Universidade de Aveiro Departamento de Engenharia Mecânica
2015

Inês Oliveira de Vasconcelos Ferreira

Análise do comportamento estrutural de painéis reforçados sujeitos a carregamentos de compressão

Analysis of the structural behaviour of stiffened panels subjected to compressive loading conditions

Universidade de Aveiro Departamento de Engenharia Mecânica
2015

Inês Oliveira de Vasconcelos Ferreira

Análise do comportamento estrutural de painéis reforçados sujeitos a carregamentos de compressão

Analysis of the structural behaviour of stiffened panels subjected to compressive loading conditions

Thesis submitted to the University of Aveiro to fulfil the necessary requirements for obtaining a Master's degree in Engenharia Mecânica, performed under the scientific guidance of Robertt Angelo Fontes Valente, Professor Auxiliar from the Departamento de Engenharia Mecânica of the University of Aveiro.

The jury

President	**Professor Doutor Ricardo José Alves de Sousa** Professor Auxiliar da Universidade de Aveiro
Committee	**Professor Doutor Robertt Angelo Fontes Valente** Professor Auxiliar da Universidade de Aveiro (orientador)
	Doutor Rui Miguel Ferreira Paulo Doutor em Engenharia Mecânica pela Universidade de Aveiro

Acknowledgements

To Professor Dr. Robertt Angelo Fontes Valente for the guidance and support.
To all my friends for the friendship.
To my family for the patience and for always being there.

Palavras-chave Painéis reforçados; Ligas de alumínio; Compósitos; Encurvadura; Pós-encurvadura; Método dos Elementos Finitos.

Resumo

Os painéis reforçados formam as estruturas básicas de construção de aviões, navios e outras estruturas que exijam uma elevada relação entre resistência e peso. Deste modo, é crucial perceber o comportamento deste tipo de painéis. Tendo em conta que a encurvadura é o modo principal de falha deste tipo de painéis, será o foco de estudo desta dissertação.

No trabalho presente, foram realizadas várias análises de forma a estudar o comportamento de encurvadura e pós-encurvadura de painéis reforçados, utilizando para isso o software de simulação Abaqus. Foram testados dois painéis diferentes, sendo que o primeiro foi um painél de alumínio, com o objectivo de perceber as metodologias envolvidas na simulação de placas reforçadas, e o segundo, um painel compósito, com o objecto de encontrar as ferramentas adequadas para simular o seu comportamento. Para isso, dois métodos distintos foram utilizados, sendo que foi utilizado o método de Riks para analisar a placa de alumínio e para analisar a placa compósita foi ultizado o método de estabilização.

O comportamento dos painéis reforçados é influênciado por vários parâmetros tais como, modelo numérico, ligação entre placa e reforço, condições de fronteira, magnitude de imperfeições, etc. Assim, todos esses parâmetros foram tidos em conta e a sua influência irá ser mostrada no trabalho presente.

Keywords Stiffened panels; Aluminium alloys; Composites; Buckling; Postbuckling; Finite Element Method.

Abstract

Stiffened panels form the basic structural building blocks of airplanes, vessels and other structures with high requirements of strength-to-weight ratio. As a consequence it is crucial to understand the behaviour of these type of panels. Since buckling is the primary mode of failure of stiffened panels, it will be the focus in the present work.

In the present work it was carried out several analysis, using the simulation software Abaqus, in order to study the buckling and postbuckling behaviour. Two different panels were tested in this thesis, the first one an aluminium stiffened panel, which its main goal was to understand the methodologies involved in the analysis of the buckling behaviour, and the second one a composite stiffened which its main goal was to find the proper tools to simulate its behaviour. Therefore, two different methods were used, the Riks method was used to analyse the aluminium panel and the Stabilize method to analyse the composite panel.

The behaviour of stiffened panels are influenced by several parameters such as, the number and type of elements, the skin-stringer connection, the boundary conditions, the magnitude of imperfections, etc. So in the present work, those parameters were taken into account and its influence will be shown.

Contents

List of Tables

List of Figures

Chapter 1

Introduction

1.1 Goals and Methodologies

The main objective of this thesis is the domain of computational tools based on the Finite Element Method (FEM) in order to analyse the behaviour of stiffened panels subjected to compressive loading conditions. Since buckling is the primary mode of failure of stiffened panels, it will be carried out several nonlinear analysis to study this problem. The simulation tool used to study buckling behaviour is Abaqus, a software created by Simulia Corp., Dassault Systmes.

Two types of panels will be analysed, the first one a flat aluminium panel and the second one a curved composite panel. The novelty in this thesis is the composite panel since the aluminium panel was already studied in detail by Paulo in [1]. The aluminium panel was tested again and included in this thesis because it was used as a starting point to learn the methods involved in the buckling and postbuckling analysis. Regarding the composite panel two models will be studied in order to check the influence of the geometry in the postbuckling area.

Both aluminium and composite panels will be analysed using similar methodologies. For both models it will be first carried out an eigenvalue analysis to extract the buckling modes in order to used them later in the nonlinear analysis as "artificial" imperfections. Also, for both models, numerous simulations will be performed in order to check the sensitivity of the results to certain parameters, such as the number and type of finite elements and the magnitude of imperfections. Regarding the analysis type, the only difference between the aluminium and composite panels is the method used to do the nonlinear analysis. While the aluminium panels are studied using the Riks Method, the composite panel is studied using the Stabilize Method. Both methods will be explained in Section 2. After being analysed all the parameters, the results will be compared with the results showed in published works in the literature being used as a guide, in order to be validated.

1.2 State of the art

1.2.1 Stiffened panel definition

Stiffened panels form the basic structural building blocks of airplanes, vessels and other structures with high requirements of strength-to-weight ratio, and they can be

produced either in a flat or curved way. These panels are used to improve the strength and also the stability of the structures [2; 3; 4; 5]. There are many different combinations of plates and stiffeners, depending on the types of structures and also the loads applied to them [6]. As a consequence, for a safe design it is crucial to understand the behaviour of the stiffened panels under distinct loading conditions and to predict their ultimate strength [7].

One example of a flat stiffened panel is illustrated in Figure 1.1 a), where it is visible that there is one plate with equally spaced longitudinal stiffeners welded on one side, and also a number of intermediate transverse stiffeners. This is a typical configuration for the deck, side or bottom of a ship hull girder [8]. In this case the longitudinal stiffener cross-section is a L-shaped with T-shaped transverse stiffeners but there are others such as bulb or flat bar which are the most common stiffener cross-sections for steel and aluminium structures [9; 10]. Also in Figure 1.1 b) it is illustrated one example of a curved stiffened panel.

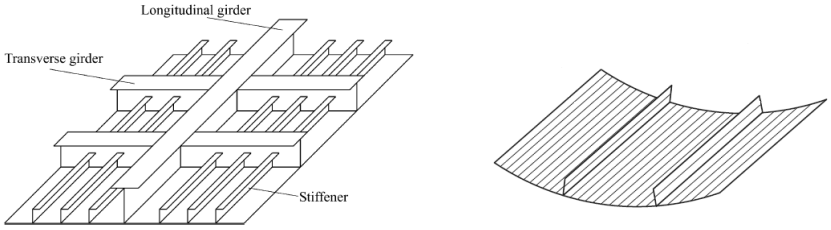

(a) Flat stiffened panel [8] (b) Curved stiffened panel [11]

Figure 1.1: Distinct configurations of reinforced panels

Curved panels are extensively used in several branches of engineering, particularly in marine and aerospace engineering, mostly working under compressive loads. Failure of these components by buckling or excessive stress is an important design consideration to be taken into account [12].

1.2.2 Aluminium applied to stiffened panels

Since there is a big concern about strength-to-weight ratio, in the marine industry developments have been made to replace steel by aluminium. However, and compared to steel there is limited accumulated experience from aluminium structures and the existing design recommendations for aluminium panels are based on experience from steel structures [4; 9; 10].

When compared to steel panels, the ultimate strength of aluminium structures is much more sensitive to residual stresses, initial deformations and deterioration of mechanical strength in heat affected zone (HAZ). However, due to new improvements in extrusion technology, and welding methods (such as friction stir welding), opportunities for new designs in aluminium appeared, which have led to improvements in geometric tolerances, increased structural efficiency and reduced costs [4; 9; 10; 13].

It is worth mentioning that the panels fabricated from the new extrusion technology, known as integrally stiffened panels (ISP), can be joined either together or to other components. With this, in the aircraft industry, it was easier to obtain complex reinforced

structures such as fuselage or cover wing walls. Other advantage was the improvement on the corrosion resistance due to the non existence of free gaps, crevices and rivet holes, since the panels can be also mainly built-up structures, where the skin and stringer are linked by riveting operations [13; 14].

In the marine industry, aluminium has been applied for the construction of high speed commercial and military vessels since 1990. In the literature it is possible to find references to a construction of an aluminium trimaran ferry over 120 m in length for service in the Canary Islands and the construction of a 140 m aluminium SES ferry as part of the Japanese Techno Super Liner project. Also the militaries use these vessels for both logistic and combat roles [15]. In Figure 1.2 it is shown one example of aluminium stiffened panels applied in the marine industry.

Figure 1.2: Aluminium stiffened panels applied in marine industry [16].

1.2.3 Composites applied to stiffened panels

Composite materials are used in a variety of activity areas which includes industries with higher requirements and technological visibility such as aeronautics, spacial and defence industries or others such as transport ones [17].

In aeronautics industry, the technological challenges are permanent and its specificity results in a production of small scale where the high manufacturing costs can be compensated by lower operating costs. Composites with high mechanical performance are used in this industry and they are fundamentally composed by carbon, aramid, hybrid carbon-aramid fibers and also boron fibers when specific applications are required. The main goal is to obtain structures with high specific strength and also a high lightness combined to a freedom of product conception [17].

Composite materials have become increasingly popular due to their considerable stiffness and strength to weight ratio, and because of this there has been a significant increase in the use of this material in stiffened panels in a wide number of aeronautical applications [18; 19; 20]. In Figure 1.3 it is shown an example of a composite stiffened panel applied in aerospace industry.

Figure 1.3: Composite stiffened panel applied in aerospace industry [21].

The structural behaviour of a composite stiffened panel is quite complex due to its complex structural form and the anisotropic material properties of the skin and stringers [22]. Despite the advantages of the anisotropy behaviour (the main characteristic of composite materials) from the perspective of structural design, it is also the main cause of complicated failure mechanisms. So a large amount of research has been dedicated to solve structural problems of composite materials. However, there has not been intensively investigated the postbuckling behaviour of composite structures compared to current metal aircraft design practise that allows the skin panels to be designed to have postbuckling strength [18; 23].

That is why the strength limits and failure characteristics must be well understood prior to designing a composite structural component with similar postbuckling response of the metallic structures [23]. Besides, the choice of a large number of design variables, such as the stacking sequences of the skin and the stiffeners as well as the geometry and the shape, are required to efficiently design the composite stiffened panels [24]. Also, the ability to tailor the stiffness and strength of a composite structure has increased, in the recent decades, in the aerospace applications. The tailorability, i.e., the ability to adapt for a particular end or purpose, consists in treating the fiber orientation of each ply as a variable and optimising the stacking sequence for laminate performance. The possibility of having variable angle tow (VAT) laminates, where the fiber orientation can change over the plane of a ply, results in laminates with varying in-plane and out-of-plane stiffness in the xy-plane, which provides designers with additional degrees of freedom and tailorability [20].

When considering design methods, it should be also taken into account the damage and failure mechanisms such as lamina bending, local fiber buckling and crack propagation [25]. Composite stiffened panels are often subjected to manufacturing defects or severe damages and adding to the lack of knowledge in predicting these damages, leads to the increase of the certification and maintenance costs. Interlaminar damages (delaminations) can be considered the most critical CFRP (carbon fiber reinforced polymers) failure mechanisms in composite stiffened panels [26]. Also other modes of failure have been studied. Adali *et al.* in [12] studied the influence of the fiber orientation on the failure load of a laminated curved panel subjected to uniaxial compression. They concluded that, for thick panels, the failure mode is mostly due to first-ply failure and, for

thin panels, buckling is the dominant failure mode. They also obtained optimal stacking sequences for selected laminations.

1.2.4 Buckling

When thin-walled structures are under compressive loads, they tend to fail by instability at stresses far bellow the material yielding compressive stress. Because of this, stiffened panels stability is a fundamental issue to structural designers [27]. Since stiffened panels may be considered as thin-walled structures, its stability is highly dependent on the buckling strength of the structure as a whole and also of each structural member. Buckling is highly influenced by how the structure is loaded as well as by the mechanical properties of the material, the geometry and the contact conditions of the structure. This type of failure can be defined as a sudden change of shape of a deformable structure, due to increasing external loads (typically compressive ones). When buckling occurs, often is catastrophic and compromises the structural functionality of the design. Even when the experiments are carefully monitored, the beginning of failure could not be predicted with precision. Also, when dealing with thin-walled shell structures, the discrepancy between the theoretical loads and the failure loads of an actual structure can be very large and so it is difficult to predict buckling initiation analytically (despite the existence of some results available in the literature) [13; 28; 29]. In Figure 1.4 it is shown an aluminium stiffened panel where it is possible to see that the panel has failed due to buckling effects. This is one example of how important is the need to find more advanced analysis tools.

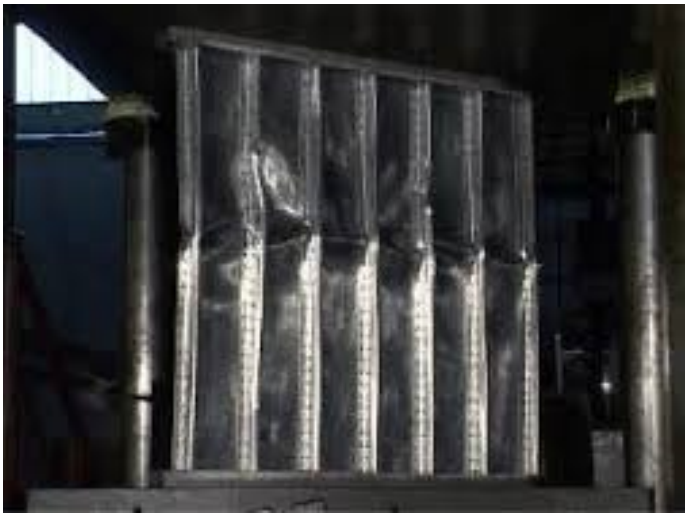

Figure 1.4: Failure of aluminium stiffened panel [7].

Buckling occurs because, in thin-walled structures, the membrane stiffness is generally several orders of magnitude greater than the bending stiffness and these structures can absorb a great amount of membrane strain energy without deforming too much. Therefore, in order to absorb an equivalent amount of bending strain, the structures must deform much more. As a consequence, if the structures are loaded in a way that most of its strain energy is in the form of membrane compression and if there is a way that this stored-up membrane energy can be converted in bending energy, the shell may

fail while the membrane energy is exchanging for bending energy [28]. When there is a reasonably large percentage of bending energy being stored in the structure throughout the loading history, the prebuckling process is often nonlinear. According to this percentage of bending energy there are two ways in which a conservative elastic system may lose its stability: nonlinear collapse (snap-through or over-the-hump) and bifurcation buckling, and these two ways of instability are shown in Figure 1.5 [28].

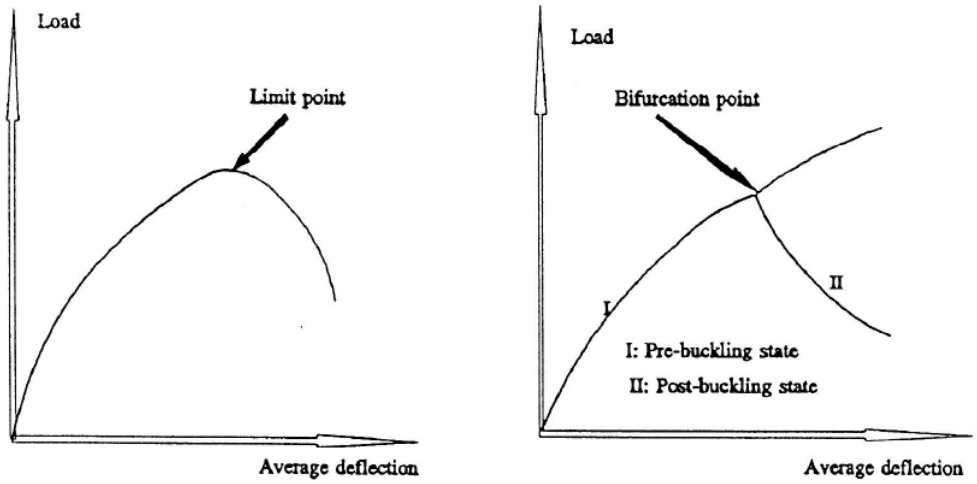

Figure 1.5: Load-deflection curves showing the two ways of instability [28].

The nonlinear collapse is predicted with a nonlinear analysis. It is possible to see in Figure 1.5 a), that the stiffness of the structure or the slope of the load-deflection curve, decreases with the increasing load and at the collapse load (limit point) the load-deflection curve has zero slope. If the load is maintained as the structure deforms, the failure of the structure will be dramatic and almost instantaneous. This type of failure is often called "snap-through" since its name derived from the many tests and theoretical models of shallow arches, caps and cones [28]. This type of failure initially deforms slowly with increasing load and when the load approaches the maximum value the rate of deformation increase until the average curvature is almost zero. Subsequently, these structures "snap-through" to a post-buckled state [28]. The other way of instability, the bifurcation buckling, can be predicted by an eigenvalue analysis. At the buckling point (see Figure 1.5 b)), the deformations begin to grow in a new pattern which is quite different from the prebuckling pattern [28].

However, an analysis of buckling initiation and growth is difficult be to performed since small variations in the parameters can result in different buckling behaviours. Therefore, the buckling analysis has been carried out case by case, by several authors, and before the use of numerical simulation, the study of the buckling behaviour was carried out through experimental and analytical studies [29]. With an analytical bifurcation analysis it is possible to estimate the elasto-plastic buckling of a simple plate however it cannot be employed in general buckling processes. Nowadays, buckling is being studied using the finite element method and assuming nonlinear geometric and material behaviours [29]. In Figure 1.6 it is shown a typical load-shortening curve for an

aluminium stiffened panel.

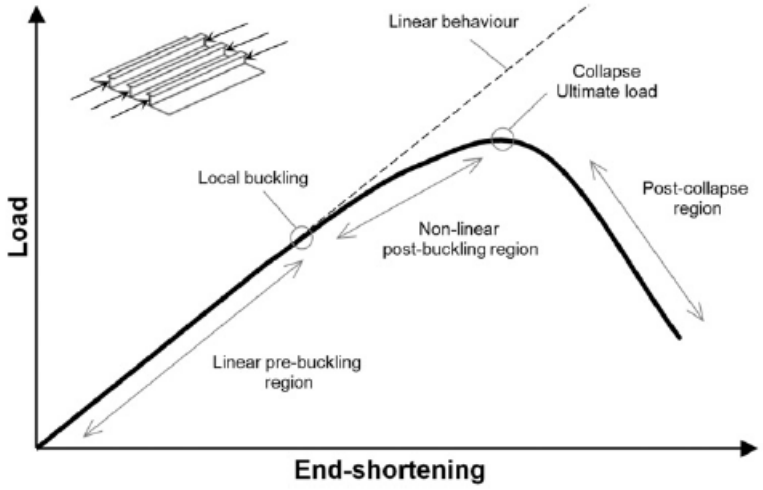

Figure 1.6: Load-shortening curve for an aluminium stiffened panel [30].

When a stiffened panel depends on its geometry and stiffness, can exhibit buckling modes which can be divided in global and local. However, the structures are usually designed such that the skin or stringers buckles prior to the global panel collapse, and so the structures enters the postbuckling regime which can still carry enough load through stress redistribution towards the unbuckled members [31].

Since stiffened panels are highly dependent on buckling behaviour, it is possible to find in literature some studies about this problem. In the field of aluminium stiffened panels, Murphy *et al.* in [32] developed a non-linear model in order to study the buckling behaviour of fuselage panels. The strategy used in this paper was based on representing a typical fuselage stiffened panel with a single non-linear element. The other results showed great potential in increasing global model accuracy. In [31], Stamatelos *et al.* studied the buckling behaviour of stiffened panels. He investigated local buckling behaviour of isotropic and laminated symmetric composite bladed stiffened plates of different aspect ratios and different number of stiffeners loaded under uniaxial compression. Khedmati *et al.* in [10] aimed to present reliable finite element models in order to study the behaviour of axially compressed stiffened aluminium plates. He considered the same model used by Rigo *et al.* in [4]. The main objectives of their work, were to compare codes and models and to perform quantitative sensitivity analysis of the ultimate strength of a welded aluminium plate. Other authors that contributed to the development of finite element methods for the accurate prediction of the post-buckling behaviour of conventional aircraft fuselage panels were Lynch *et al.* in [33]. Relatively to composite materials, Degenhardt *et al.* in [34] studied the behaviour of a compressed CFRP stiffened panel including damaged region. Vescovini *et al.* in [24] presented the buckling optimization of composite stiffened panels loaded in compression and shear. They compared analytical results with finite element analysis. Se-Hee Oh *et al.* in [18] proposed an efficient and accurate post-buckling analysis technique for a composite stiffened structure. Coburn *et al.* in [20] presented an analytical model for the pre-buckling and buckling analysis for novel blade stiffened VAT panels and then compared the model to a finite element

analysis.

1.2.5 Adhesive bonding

Structural adhesives has been adopted by the aerospace industry as a bonding technique of primary and secondary structural elements due to the increasing use of polymer composites. Structural adhesives offer much more advantages than the traditional techniques, such as mechanical fastening, and thus the engineers tend to replace mechanical fastenings with adhesive bonding also in metallic parts [35].

Although airworthiness regulations require the use of damage tolerance philosophy for the design of the structure, several interpretations of damage tolerance concept exist, mainly related to differences in structural behaviour of metallic and polymer composite structures. While in the metallic structures the tolerance concept is well established and allows damage, in the form of cracks, to exist and grow up to a critical size, in the polymer composite structures no-growth policy is adopted, although damage may exists [35]. There is a limited number of studies that investigate the effect of defects on the buckling behaviour of structures and most of them deal with defects in form of delaminations or disbonds in polymer composite plates [35]. One example is the work made by Hu *et al.* in [36] where they performed a buckling analysis of a composite panel with an embedded delamination at the mid-plane of the structure. The authors developed a method to deal with contact problems between the debonded plies of the composite panel and they investigated the influence of different size, shapes and positions of the delaminations. They concluded that the buckling load decreased as the delamination size increased and the buckling mode varied from a global mode, when the delamination was located close to the mid-plane, to a local mode, when the delamination was located close to the surface of the plane.

Arman *et al.* investigated the effect of a circular delamination around a circular hole on buckling load of a woven fabric laminate composite plate identifying a critical size of the delamination at which the stiffness of the plate and the buckling load capacity decreased significantly [37]. Regarding to stiffened panels, Zarouchas *et al.* in [35] focused on understanding the effect of disbonds on stability aspects of adhesively bonded aluminium structures. The authors presented the influence of different size and position of disbonds of a panel with four adhesively bonded aluminium stiffeners. The numerical methodology developed by the authors consisted in coupling non-linear buckling analysis and calculation of the disbond growth onset using the Virtual Crack Closure Technique (VCCT). Other study was conducted by A. Riccio *et al.* in [26] where they proposed a novel numerical methodology, alternative to the standard VCCT-based approach and able to overcome mesh and time step sensitivity problems.

There are four main methods for structural and damage analysis of adhesively bonded structures subjected to quasi-static and fatigue loadings in order to predict delamination growth [35]:

- Stress-strain based methods;
- Fracture mechanics based methods;
- Cohesive zone model (CZM);
- Extended finite element method (XFEM).

The stress-strain methods analyse the stress-strain distributions in the adhesive joint, which are sufficient for damage initiation prediction, using suitable failure criteria, and for the prediction of bond's strength. It is possible to find a summary of this method and existing models in [39].

The fracture mechanics based methods link the progression of damage, i.e. cracks in metals, delaminations in composites, adhesive and cohesive debonds in bonded joints, with the fatigue life of the structure by determining the parameters Stress Intensity Factor(SIF) and/or Strain Energy Release Rate(SERR). Although both parameters are equivalent in providing information, SERR is preferable because local stress field near the crack tip is difficult to obtain especially for anisotropic composite laminates. SERR can be either calculated analytically or numerically using Finite Element Analysis, where the most common finite element technique is the VCCT [35]. This method will be explained in Section 2.

CZM is a finite element method in which the interface between two elements is modelled using cohesive zone elements. It consists of a constitutive relation between the traction acting on the interface and the interfacial displacement. This relation depends on the type of element and material used [35]. Also this method will be explained in Section 2.

XFEM is a flexible modelling technique which allows the crack to grow arbitrarily through the element than just along a predefined crack path or crack plane. This method uses enrichment functions which are added to certain nodes of the elements, and potential lies on the fact that it can be coupled with other techniques, such as VCCT, where XFEM can be used to find the delamination growth direction and VCCT can be used to calculate the SERR values [35].

Delamination is the most common form of interlaminar damage and occurs due to high through-thickness stresses overcoming the interlaminar bond strength between two plies. The skin and stiffeners, for the composite aerospace structure, are either co-cured as a complete laminate or manufactured separately and adhesively bonded. So, for aerospace structures, the interlaminar damage is most commonly encountered as skin-stringer debonding, either as delaminations at or around the skin-stringer interface in co-cured laminates, or as adhesive failure in secondary bonded structures. Skin-stringer debonding is a common, and often explosive, form of failure, which has occurred in a large number of experimental investigations into postbuckling stiffened structures [40]. In Figure 1.7 is shown the adhesive failure of a composite stiffened panel.

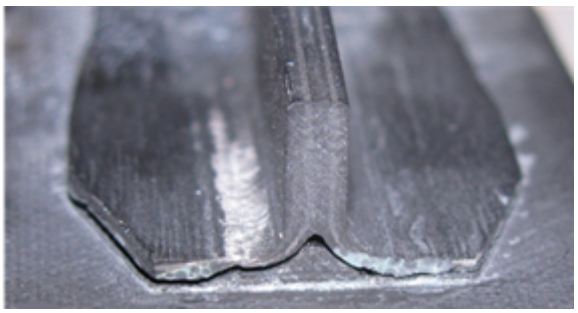

Figure 1.7: Adhesive failure of a composite stiffened panel [38].

The fracture process in high performance composite laminates is quite complex, in-

volving not only delamination, but also intralaminar damage mechanisms, such as transverse matrix cracking and fiber fracture. Usually the simulation of delaminations in composites is divided into delamination initiation and delamination propagation [41].

1.2.6 Friction Stir Welding (FSW)

Friction stir welding (FSW) is a process used to join parts without reaching their melting point. The main advantage of this process is the decreasing of the assembly time which leads to lower manufacturing costs and higher productivity. Also the structural efficiency is increased by means of the optimal placement of structural material and the elimination of fasteners [42].

FSW is a solid phase welding process in which a cylindrical shouldered tool with a profiled pin is rotated and plunged into the joint area between the two pieces of material. The two pieces of material should be forced to each other to be joined correctly. The tool is allowed to traverse along the weld line since frictional heat between the wear resistance welding tool and the material causes the latter to soften without reaching the melting point. The plasticised material is forged through intimate contact with the tool shoulder and pin profile. After this, it is created a solid bond between the materials [43]. In figure 1.8 it is illustrated the friction stir welding process.

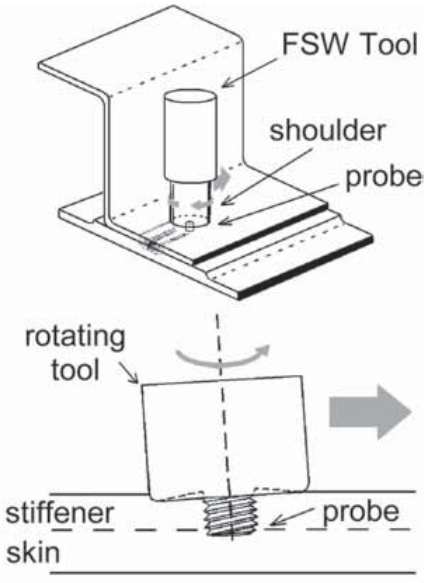

Figure 1.8: The friction stir welding process [44].

This process has being used in only a limited number of flight vehicles since there is limited experience of process industrialisation and limited knowledge on in-service performance. Some studies have been undertaken in order to understand the impact of local joint material degradation and induced residual stress on the static strength of final fabricated components. However these studies do not examine directly the impact of panel weld location, nor is there experimental analysis of representative welded wing panel structure. Thus, Murphy *et al.* in [45] presented the results of a study undertaken

to assess the impact of assembly weld joint location on the collapse behaviour of stiffened panels. A series of simulations were carried out in order to expand the knowledge on the impact of weld location and with a conducted experimental study to validate them.

With this study, Murphy and co-authors concluded that with an optimised friction stir welding, the welding induced local material degradation, residual stresses and geometric imperfections only have a modest impact on the assembled panel static strength. The geometric imperfections have the greatest impact on the panel static strength while the welding induced local material degradation only displays a modest influence on strength, which could be decreased with the size of the assembled structure. Relatively to residual stresses, these could increase with the increase of the assembled structure, although they only have also a very modest strength impact on the panel performance [45].

Friction stir welds include a thermo-mechanically affected zone and a heat-affected zone (HAZ). This is schematically shown in Figure 1.9 [44].

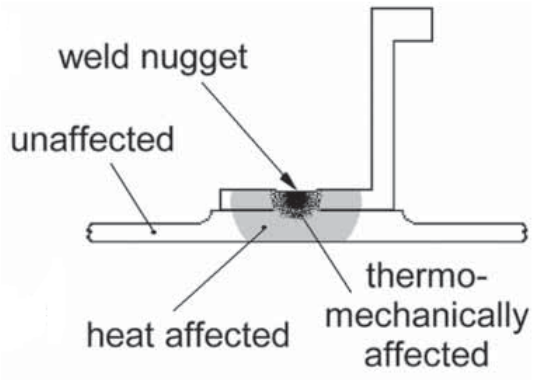

Figure 1.9: Schematic representation of weld transverse cross-section [44].

There are also two regions which have experienced high temperatures and extensive plastic deformation. These regions are a nugget region (within the thermo-mechanically affected zone) and a region at the top of the weld. Both regions contain much smaller grains than the parent (base) material [44].

The parent material grains are affected by some deformation, however recrystallization will not have taken place because of the lesser degree of freedom of deformation and lower temperatures within the remaining thermo-mechanically affected zone.

It is useful to simplify these various thermally and mechanically affected zones into one when it comes the time to analyse the static strength of welded structures. So, these affected zones are commonly termed the HAZ. The HAZ material has lower strength than the parent material for the most metals used in fabrication, with exception of steel [44].

Besides all the advantages of friction stir welding processes, there are still major issues to be addressed. The biggest problem of this process is the lack of information on the linkages between welding process parameters and the resultant induced or modified panel properties, and the consequence on strength performance of the fabricated structures [42].

1.3 Reading Guide

This dissertation report has six chapters which are presented and described hereafter.

In Chapter 1 it is presented the literature review related to the aluminium and CFRP stiffened panels and also the goal and methodologies used in this work.

In Chapter 2 it is given a brief summary about what is the Finite Element Method and how it can be applied to stiffened panels. Some studies carried out by different authors are also mentioned as examples.

In Chapter 3 it is given a brief summary about the composite materials. The fibers and matrices related to the material used in Chapter 5 will be explained as well as the constitutive laws of the layer.

In Chapter 4 it is presented the results obtained by the simulations and then compared to the results obtained in [30] in order to validate the method used in the present work.

In Chapter 5 it is presented in detail the analysis of a curved stiffened composite panel and its results.

In Chapter 6 the conclusions of this thesis are presented and some suggestions for future works are given.

Chapter 2

Finite Element Method

2.1 Introduction

The Finite Element Method, (FEM), consists in the modeling of a generic problem, which involves continuous means, in order to obtain a mathematical description of its behaviour through the analysis of its discrete parts. To each discrete element, or in other words, to each finite element, and its laws which commands its behaviour, lead to the analysis and to the knowledge of the global problem.

It should be reminded that the FEM is an approximate method and so every numerical simulation gives an approximate solution. That is why this method should only be employed when there is no other approach or an analytical solution to solve the problem.

The FEM can be applied to several problems such as, the study of vibrating systems, the analysis of material's behaviour, determination of problems related to heat transfer and fluid mechanics, sizing of large scale structures, metallic and non metallic structures, etc. [46].

Relatively to stiffened panels, the FEM has been typically applied since it is a powerfull tool which can reproduce almost all type of problems. In order to obtain accurate results, some parameters such as, the type and number of elements, geometry and magnitude of imperfections and boundary conditions, should be carefully chosen.

There are some software such as Abaqus, MSC, ANSYS and LS-DYNA which are used to simulate these problems. In the present work, the software chosen to model and simulate the panels was Abaqus [47]. This is a software marketed by Simulia, a company which belongs to the Dassault Systems SA. group.

2.2 Type of elements and mesh convergence

As it was mentioned before the type and number of elements chosen for the simulations is a determining factor in order to have an accurate result.

Abaqus has an extensive element library to provide a powerful set of tools for solving many different problems. The elements have specific names in order to identify the aspects that characterizes its behaviour. There are five aspects to be considered: family, degrees of freedom, number of nodes, formulation and integration. In Figure 2.1 it is illustrated the element families that are most commonly used [47].

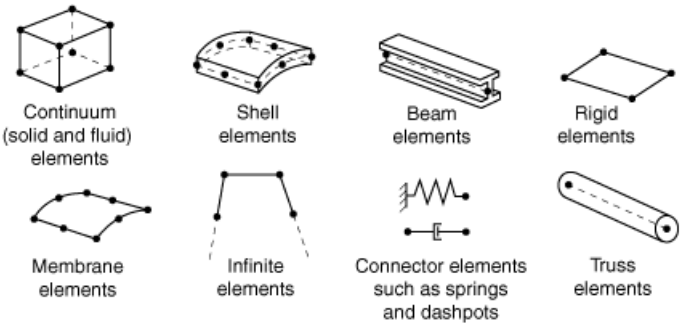

Figure 2.1: Representative element families [47].

The first letter of an element identifies to which family the element belongs. For instance, the code S8R corresponds to a shell element while C3D8I corresponds to a continuum element.

In the present work all the simulations were carried out using shell elements (in the modelling of the skin and stringers of the stiffened panels) from Abaqus library. However there are studies made by different authors that compare different type of elements and uses different softwares. For instance, Yoon *et al.* in [29] compares three different type of continuum elements from Abaqus library: C3D8 (conventional, displacement-based solid element, eight nodes, fully integrated), C3D8I (enhanced continuum-shell element, eight nodes, fully integrated, 13 internal parameters) and C3D8R (reduced integrated solid element, eight nodes, hourglass control). After an analysis of a quarter of a plate using this type of elements, Yoon concluded the best choice was C3D8I since it only has a 0.113% of desviation from the analytical solution while C3D8 has a 1665% of desviation and C3D8R has a 2364% of desviation from the analytical solution.

In Lynch and co-authors work [33], a mesh convergence study was undertaken in order to enable element selection. They considered five different shell elements which were assessed based on the convergence, with increasing mesh density, of the predicted buckling stresses and load-deflection curves to the corresponding theoretical behaviour. After the analysis, it was concluded that S8R5-type element (shell element with eight nodes and reduced numerical integration, with five degrees-of-freedom per node) provides optimum buckling and postbuckling solutions.

In other study [54] following on fracture prediction, the influence of shell elements and solid elements on fracture is carried out. It is mentioned that one problem with the finite element method is the sensitivity to mesh sizes which is apparent in zones with large strain gradients and shell elements are especially sensitive to this, due to the plane stress formulation. While the through-thickness stress stabilizes solid elements subjected to thinning, shell elements are only restrained by neighbouring elements. This means that shells elements are free to deform in the thickness direction and consequently they may strain excessively. This problem happens with small elements and once large elements are applied, the strain concentrations remain uncaptured.

The aim of Rigo and co-authors work [4] was to validate a non-linear finite element model for calculation of the ultimate compressive strength of aluminium stiffened panels. So, a calibration assessment was done comparing the results of contributors that performed an identical analysis with different codes. Hereafter, it is presented the results obtained by the contributors of the Committee III.1 "Ultimate Strength" of ISSC'2003,

in order to compare different codes and different number of elements. In Figure 2.2 is shown a table which summarizes the different codes and different meshes used by the contributors.

	FEM software	Mesh		Number of elements on a single line (or row)				
		Type of element	Total number of elements	Number of elements along X in one span of 1025 mm (or 2050 mm)	Number of elements along Y (between two stiff.)	Number of elements for the web (stiff)	Number of elements for the flange (stiff)	Number of elements on the plate HAZ's width
Lehmann–Catalin	MSC Marc	Shell	8520	40	8	3	1	2 for Weld A 2 for Weld B
Philippe–Radu—standard mesh	ANSYS	Shell43	6588	16	13	4	2	5 for Weld A 4 for Weld B
Philippe–Radu—Fine mesh	ANSYS	Shell43	13656	42	13	4	2	5 for Weld A 4 For Weld B
Pasqualino–Estefen	ANSYS	Shell43	10320	40	12	3	1	4 for Weld A
Wan (coarse mesh)	ANSYS	Shell143	1866	10	6	3	1	2 for Weld A
Wan (standard mesh)	ANSYS	Shell143	7150	36	6	5	1	2 for Weld A
Wan (fine mesh)	ANSYS	Shell143	12292	50	10	5	1	4 for Weld A
Yao—phase A (coarse mesh, M2)	ULSAS	Shell/beam	4160/480	96	20	4	Beam-column element	No
Yao—phase A (fine mesh, M4)	ULSAS	Shell/beam	14400/960	192	40	6	Beam-column element	No
Yao—phase B (final mesh)	ULSAS	Shell/beam	8880/480	96	50	6	Beam-column element	2 for Weld A 2 for Weld B
Bo–Ulrik	LS-DYNA	Shell	7850	32	13	4	2	5 for Weld A 4 for Weld B

Figure 2.2: Software and meshes used by the contributors [4].

In Figure 2.3 is shown the results obtained by the contributors and it is possible to see that there are slight differences. Although the different softwares used by the participates, it is possible to compare those who used the same software but different number of elements, for instance Philippe-Radu. With the same software and the same type of elements, Philippe-Radu obtained different results.

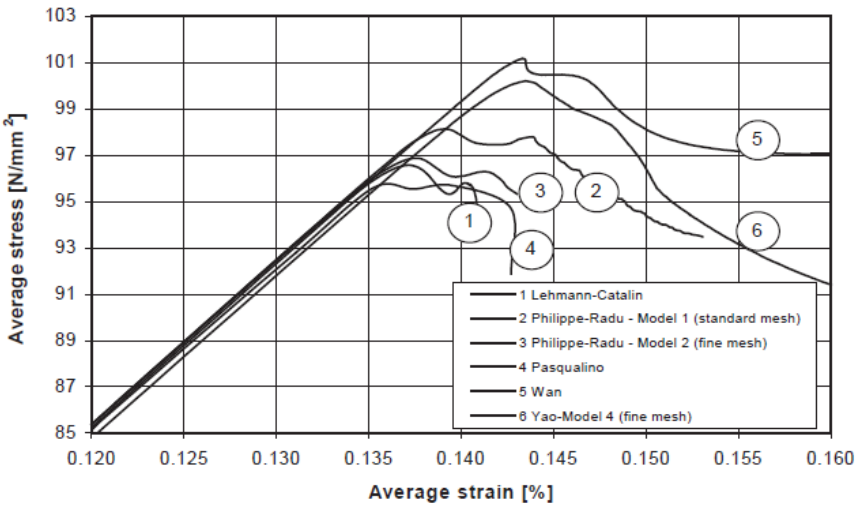

Figure 2.3: Results obtained by the contributors [4].

With this stydy, Rigo *et al.* [4] concluded that, for their model, it is necessary a minimum of 8000 elements to get the ultimate strength and about 12000 elements to

assess the post collapse behaviour.

Shell elements are used most commonly in stiffened panels since this type of elements are used to model structures in which the thickness is significantly smaller than the other dimensions which is the case of stiffened panels. Besides, shell elements are in advantage in terms of implementation and computational effort when compared to solid elements.

The shell elements available in Abaqus Standard library are:

- S3: A 3-node triangular general-purpose shell, finite membrane strains.
- STRI3: A 3-node triangular facet thin shell.
- S4: A 4-node doubly curved general-purpose shell, finite membrane strains.
- S4R: A 4-node doubly curved thin or thick shell, reduced integration, hourglass control, finite membrane strains.
- S4R5: A 4-node doubly curved thin shell, reduced integration, hourglass control, using five degrees of freedom per node.
- STRI65: A 6-node triangular thin shell, using five degrees of freedom per node.
- S8R: A 8-node doubly curved thick shell, reduced integration.
- S8R5: A 8-node doubly curved thin shell, reduced integration, using five degrees of freedom per node.

2.3 Eigenvalue analysis

An eigenvalue analysis is used to estimate the critical buckling loads of stiff structures. This type of analysis is a linear perturbation procedure and buckling loads are calculated relative to the base state of the structure. The base state is formed by the initial conditions when the eigenvalue buckling procedure is the first step in an analysis. Otherwise, it can be the current state of the model at the end of the last general analysis step. The base state can also include preloads, which are often zero in classical eigenvalue analysis [47].

What matters in an eigenvalue buckling problem is to find the loads for which the model stiffness matrix becomes singular and for that it is necessary that

$$\mathbf{K}^{MN} v^M = 0, \tag{2.1}$$

has nontrivial solutions. $\mathbf{K}^{MN}$ is the tangent stiffness matrix when the loads are applied, and the v^M are nontrivial displacement solutions.

To calculate the critical buckling loads is necessary to define an incremental loading pattern Q^N in the eigenvalue buckling prediction step. The magnitude of this load is not important because it will be scaled by the load multipliers, λ_i found in the eigenvalue problem

$$(\mathbf{K}_0^{NM} + \lambda_i \mathbf{K}_\Delta^{NM}) v_i^M = 0, \tag{2.2}$$

where:

- $\mathbf{K}_0^{NM}$ is the stiffness matrix corresponding to the base state, which includes the effect of the preloads if they exist;
- $\mathbf{K}_\Delta^{NM}$ is the differential initial stress and load stiffness matrix due to the incremental loading pattern, Q^N;
- λ_i are the eigenvalues;
- v_i^M are the buckling modes shapes;
- M and N refer to degrees of freedom of the whole model;
- i refers to the ith buckling mode.

Usually the lowest value of λ_i is the one that interests and corresponds to the lowest critical buckling load.

The buckling mode shapes, v_i^M, are normalized vectors and so the maximum displacement component is 1.0. These buckling mode shapes are often the most useful outcome of the eigenvalue analysis, since they predict the likely failure mode of the structure.

In Abaqus/Standard there are two eigenvalue extraction methods. One of them is the Lanczos method which is generaly faster when a large number of eigenmodes are required for a system with many degrees of freedom. The other one is the subspace interaction method which may be faster when only a few (less than twenty) eigenmodes are needed. The Lanczos eigensolver cannot be used for buckling analysis in which the stiffness matrix is indefinite.

After the eigenvalue analysis if there is any concern about material nonlinearity, geometric nonlinearity prior to buckling or unstable postbuckling response, a load-deflection (Riks) analysis must be performed [47].

2.4 Riks method

The Riks method is generally used to predict unstable, geometrically nonlinear collapse of a structure. It can include nonlinear materials and boundary conditions, and often follows an eigenvalue buckling analysis to provide complete information about a structure's failure. It also can be used to speed the convergence of ill-conditioned or snap-through problems that do not exhibit instability [47]. The Riks method is briefly summarized hereafter.

For a conservative system, the change of the total potential energy $\Delta\Pi$ due to an admissible variation δu of the displacement field u can be written as

$$\Delta\Pi(u, \delta u) = \frac{\partial \Pi}{\partial u_i} + \frac{1}{2}\frac{\partial^2 \Pi}{\partial u_i \partial u_j}\delta u_i \delta u_j + ... \tag{2.3}$$

To have a stable system, the second variation term must be positive definite which leads to

$$\frac{\partial^2 \Pi}{\partial u_i \partial u_j}\delta u_i \delta u_j = \mathbf{K}_{ij}\delta u_i \delta u_j > 0, \tag{2.4}$$

where $\mathbf{K}_{ij}$ represents the component of the tangent stiffness matrix $\mathbf{K}$. So, when the matrix $\mathbf{K}$ ceases to be positive definite, the stability limit is reached. This is described for

$$det[\mathbf{K}] = 0. \tag{2.5}$$

With only one incremental step in implicit analysis, the determinant in Eq. 2.5 can change abruptly. When each value of the diagonal terms of a triangular form of the stiffness matrix is checked, it is possible to find the bifurcation point [29].

The finite element solution past the bifurcation point should not be the primary path, but the secondary or bifurcated path. In most bifurcation problems, the eigenvector is orthogonal to the primary path and so the increment of the nodal displacement field along the secondary path Δu^s can be taken as

$$\Delta u^s = \chi v, \tag{2.6}$$

where χ is a positive scalar and v is an eigenvector at a singular point calculated from

$$\mathbf{K}v = 0. \tag{2.7}$$

The trial increment $\Delta u^s = v$, in Eq. 2.6, is used as an initial estimate for the Newton-type solution scheme and is updated during the iteration and therefore the magnitude of χ is eliminated [29].

Summarized, the Riks method is a searching technique of equilibrium condition at unstable states. It is a good method to be used with global buckling problems [18]. In the case of local buckling problems, the Stabilize Method should be used and it will be described in the section below.

2.5 Stabilize method

Nonlinear static problems can be unstable and such instabilities can be of a material nature or of a geometrical nature, such as buckling, which is the case of stiffened panels [47]. If these instabilities operates itself in a global load-displacement response, the problem can be treated using Riks method, described in the section above. However, if the instability is localized there will be a local transfer of strain energy from one part of the model to neighbouring parts, and Riks method may not operate normally [18; 47]. Besides, the Riks method conserves the structural strain energy during the analysis processes, but it is not conserved at the moment of buckling mode change [18]. In this case the Stabilize method should be used.

The Stabilize method finds the equilibrium condition by importing an artificial damping factor that decreases the strain energy and transfers the concentrated energy to other sections. Thus, the strain energy level of the system changes to a low and unique condition which results in an improved convergence and in the possibility of stable results [18].

Abaqus/Standard offers an automatic mechanism for stabilizing unstable quasi-static problems through the automatic addiction of volume proportional damping to the model. The applied damping factors can be constant over the duration of a step, or they can

vary with time to account for changes over the course of a step. The latter, adaptive approach is typically preferred [47].

When it is used the automatic stabilization with a constant damping factor, the stabilization is triggered by including automatic stabilization in any nonlinear quasi-static procedure. This means that viscous forces of the form,

$$F_v = c\mathbf{M}^* v, \tag{2.8}$$

are added to the equilibrium equations,

$$P - I - F_v = 0, \tag{2.9}$$

where $\mathbf{M}^*$ is an artificial mass matrix calculated with unity density, c is a damping factor, $v = \Delta u/\Delta t$ is the vector of nodal velocities, and Δt is the increment of time (which may or may not have a physical meaning in the context of the problem being solved). The damping factor can be specified directly but generally it is quite difficult to make a reasonable estimate for the damping factor, unless a value is known from the output of previous runs. The damping factor depends not only on the amount of damping but also on mesh size and material behaviour [47].

The approach mentioned above, typically works well to subside instabilities and to eliminate rigid body modes without having a major effect on the solution. However there is no guarantee that the value of the damping factor is optimal or even suitable in some cases. This is particularly true for thin shell models, in which the damping factor may be too high when a poor estimation of the extrapolated strain energy is made during the first increment. For such models it is necessary to increase the damping factor if the convergence behaviour is problematic or to decrease the damping factor if it distorts the solutions. Therefore, obtaining an optimal value for the damping factor is a manual process requiring trial and error until a converged solution is obtained and the dissipated stabilization energy is sufficiently small.

An effective alternative approach is provided by the automatic stabilization scheme, in which the damping factor can vary spatially and with time. In this case the damping factor is controlled by the convergence history and the ratio of the energy dissipated by viscous damping to the total strain energy. If the convergence behaviour is problematic because of instabilities or rigid body modes, Abaqus/Standard automatically increases the damping factor. The ratio of the energy dissipated by viscous damping to the total strain energy is limited by an accuracy tolerance specified in Abaqus. Such an accuracy tolerance is imposed on the global level for the whole model. If the ratio of the energy dissipated by viscous damping to the total strain energy for the whole model exceeds the accuracy tolerance, the damping factor at each individual element is adjusted to ensure that the ratio of the stabilization energy to the strain energy is less than the accuracy tolerance on both the global and local element level. The stabilization energy always increases, while the strain energy may decrease. Therefore, Abaqus/Standard restricts the ratio of the incremental value of the stabilization energy to the incremental value of the strain energy for each increment to ensure that this value has not exceeded the accuracy tolerance if the ratio of the total stabilization energy to the total strain energy exceeds the accuracy tolerance. The accuracy tolerance is a targeted value and can be exceeded in some situations, such as when there is rigid body motion or when significant non-local instability occurs.

Some authors such as A. Blzquez *et al.* in [19], R. Degenhardt *et al.* in [48] and A.C. Orifici *et al.* in [49] are some examples of authors who used the Stabilize method to study the buckling and postbuckling behaviour of stiffened panels.

2.6 Imperfections

The geometric imperfections are generally introduced in a model for a postbuckling load-displacement analysis. As it was mentioned before, the Riks method is used to solve postbuckling problems but sometimes the exact problem cannot be analysed directly due to the discontinuous response at the point of buckling. Therefore, it is necessary to introduce a geometric imperfection in order to get some response in the buckling mode before the critical load is reached.

Imperfections are usually introduced by perturbations in the geometry. In Abaqus there are three ways to introduce an imperfection. They can be [47]:

- defined as a linear superposition of buckling eigenmodes obtained from a previous eigenvalue buckling prediction;
- defined from the displacements of a static analysis;
- defined by specifying the node number and displacement values directly.

Unless the precise shape of an imperfection is known, an imperfection consisting of multiple superimposed buckling modes can be introduced. Usually, the approach involves two analysis runs with the same model definition, the first one using Abaqus/Standard to establish the probable collapse modes and the second one using either Abaqus/Standard or Abaqus/Explicit to perform the postbuckling analysis. The lowest buckling modes are frequently assumed to provide the most critical imperfections, and so usually these are scaled and added to the perfect geometry to create the perturbed mesh [47]. The imperfection has the form,

$$\Delta x_i = \sum_{i=1}^{M} w_i \phi_i, \tag{2.10}$$

where ϕ_i is the i^{th} mode shape and w_i is the associated scale factor.

In the literature it is possible to find some examples about how to introduce the imperfections. For example, Caseiro *et al.* in [13] introduced the imperfections directly into the model. The imperfections were applied to the nodes in the middle of the panel with a magnitude of l/1000, where l is the length of the panel. Thus, the imperfections have an effect on the coordinates of the nodes with an offset along the normal direction to the skin plate. It is shown in Figure 2.4 the details of the imperfection.

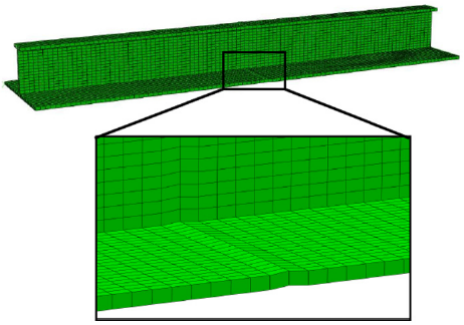

Figure 2.4: Details of the imperfection [13].

Other way to introduce the imperfections was presented by Rigo *et al.* in [4], and it consists in applying a uniform lateral pressure on the overall structure. It is shown in Figure 2.5 the procedure to define the initial imperfections.

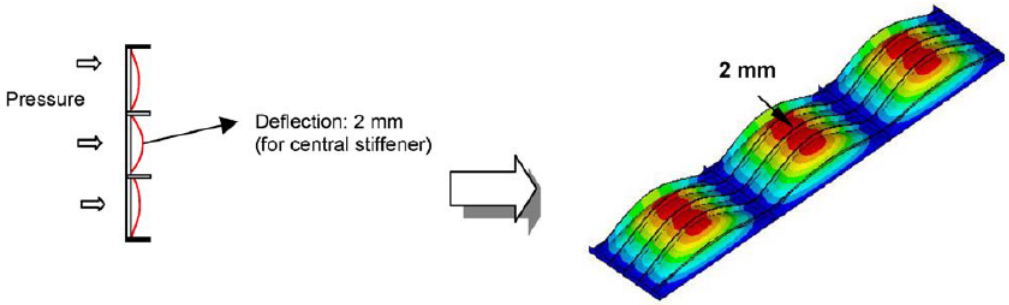

Figure 2.5: Procedure to define the imperfections [4].

Rigo *et al.* [4] calibrated the pressure in order to obtain a linear elastic deflection of 2 mm at the central point of the central panel. It is assumed that the shape and amplitude of the initial imperfections are identical to the deflections induced by the uniform lateral pressure and therefore they were captured and used to define the geometry of the FEM model. These imperfections do not induce stresses.

In [33], Lynch *et al.* used the eigenvalue analysis to determine the first buckling mode and use it as an initial imperfection in the postbuckling analysis. In the present work the imperfections were defined as a linear superposition of buckling eigenmodes obtained from a previous eigenvalue buckling prediction.

2.7 Cohesive Zone Method (CZM) and Virtual Crack Closure Technique (VCCT)

As it was mentioned before, in the aerospace industry, the skin and stringer can be manufactured separately and adhesively bonded. As a result, interlaminar damage is most commonly encountered as skin-stringer debonding as delaminations. Two different ways of modelling the behaviour of interlaminar damage in Abaqus is using CZM and VCCT models.

The cohesive zone method implements interfacial constitutive laws defined in terms of damage variables and a damage evolution law. Cohesive elements are usually inserted between solid elements or beam/shell elements. The virtual crack closure technique uses a fracture mechanics approach, where the propagation of an existing delamination is analysed by comparing the amount of energy release rate with the fracture toughness of the interface. When mixed modes conditions are involved, the decomposition of the total energy release rate into mode I, mode II, and mode III components becomes necessary due to the mixed-mode dependency of interface toughness [51]. Since a delamination crack propagates with its advancing tip in mixed mode condition, the analyses requires a fracture criterion including all three mode components.

The elastic strain energy per unit volume (in $(\frac{J}{m^3})$) is defined as

$$U_0 = \frac{1}{2\sigma_{ij}\epsilon_{ij}}. \tag{2.11}$$

The strain energy (in Joules) is defined as the volume integral

$$U = \int_V U_0 dV. \tag{2.12}$$

The energy required to form, or propagate, a crack is equal to the elastic energy released by the solid during the crack formation. The energy released is the difference between the elastic strain available before and after the crack is formed, i.e.,

$$-\Delta U = U_{after} - U_{before}. \tag{2.13}$$

The rate of energy released per unit of crack area A (in $(\frac{J}{m^2})$) is given by

$$G = -\frac{\Delta U}{\Delta A}, \tag{2.14}$$

where A is one half the surface area created. The theory of crack growth may be developed by using Griffith or Irwin approach. The Griffith approach uses, in one hand, the concept of energy release rate, G, as the energy available for fracture and in the other hand, the material property, G_c as the energy necessary for fracture. A crack grows when

$$G > G_c, \tag{2.15}$$

where $G_c = 2\gamma_c$, with γ_c being the critical fracture energy per unit surface of crack area. The Irwin approach is based on the concept of stress intensity factor, which represents the energy stress field in the neighbourhood of the crack tip. Both approaches are equivalent and, therefore, the energy criterion may be rewritten in terms of stress intensity factors [51].

The elastic strain energy released ΔU during crack propagation, and therefore used to create the new surface area, can be calculated as the work required to close the crack, this means,

$$\Delta U = W_{closure}. \tag{2.16}$$

The crack closure method provides the base for the virtual crack closure technique which it is described hereafter.

As it was mentioned before, the VCCT can be used to analyse delaminations in laminated materials using a fracture mechanics approach, where the linear elastic fracture mechanics (LEFM) is implemented and only brittle crack propagation is modeled. The condition for crack propagation is based on Griffith's principle (2.15). For the case of single mode deformation under mode I conditions, the crack grows when

$$\frac{G_I}{G_{Ic}} \geq 1, \tag{2.17}$$

where G_I is the energy release rate for mode I crack formation and G_{Ic} is a material property representing the critical energy release rate for mode I crack formation.

With the VCCT model, the Irwin approach is used to calculate the change in strain energy ΔU, which is considered to be equal to the work required for crack closure, $W_{closure}$, as it was seen in 2.16. By substituting 2.14 and 2.16 into 2.17, the condition of crack propagation becomes,

$$\frac{W_{closure}/\Delta A}{G_{Ic}} \geq 1. \tag{2.18}$$

Abaqus calculates $W_{closure}$ from the FE nodal displacements and forces as illustrated in Figure 2.6.

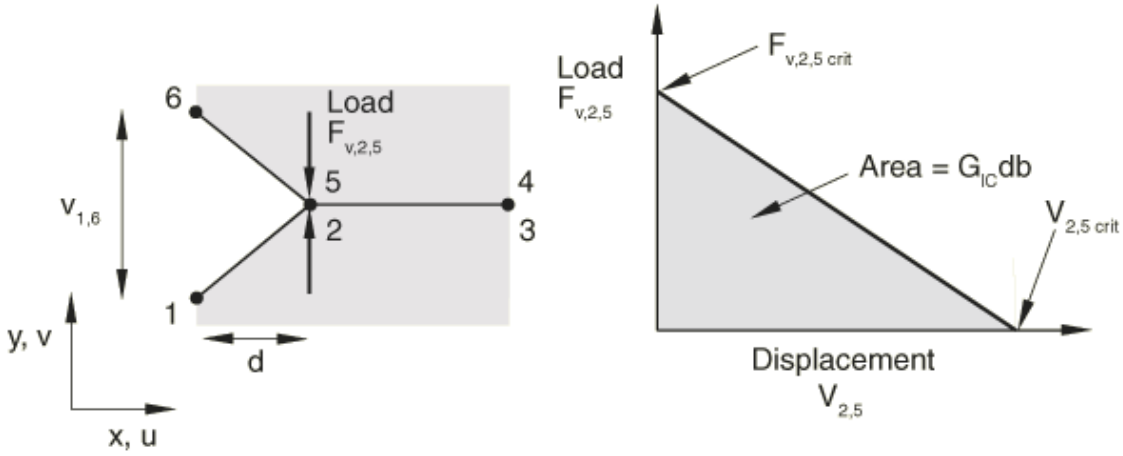

Figure 2.6: VCCT model [47].

where nodes 2 and 5 will start to release when [47],

$$\frac{1}{2}\left(\frac{v_{1,6}F_{v,2,5}}{bd}\right)\frac{1}{G_{Ic}} \geq 1. \tag{2.19}$$

VCCT has been used for many authors in research and industry to predict interlaminar crack growth in composite structures. For instance, in [50], Lauterbach *et al.* used this method to simulate the progress of delamination of initial debonded areas. Their study consisted in using a FE model generated with nominally coincident shell layers of skin and stringers which were connected by MPC's (multi-point constraints). The VCCT was used to determine the strain energy release rate of all MPC's at the crack

front. Also, Riccio in [26] used the VCCT to study the skin-stringer debonding growth in composite stiffened panels. They proposed a novel numerical methodology, alternative to the standard VCCT-based approach and able to overcome mesh and time step sensitivity problems, in order to investigate the evolution of interface defects between the skin and the stringer.

Regarding the cohesive zone model, this one is based on the assumption that the stress transfer capacity between the two separating faces of a delamination is not lost completely at damage initiation, but rather is a progressive event governed by progressive stiffness reduction of the interface between the two separating faces [51].

In Abaqus, the interface between the two possible separating faces of the laminated material is modeled with cohesive elements and there are two types:

- Elements with finite thickness, which are based on a regular, continuum ($\sigma - \epsilon$) constitutive behaviour. This type of elements is used to model delamination behaviour of adhesive bonds where the thickness of the interface is considerable;

- Elements with zero thickness, which are based on a traction-separation ($\sigma - \delta$) constitutive behaviour. This type of elements is used to model delamination behaviour of adhesive bonds where the thickness of the interface is negligible, as it is in the case of laminated composites. One example of application of these elements is in the debonding along skin-stringer interface [47].

In the case of a continuum constitutive behaviour, the cohesive elements model the initial loading, the initiation of damage, and the propagation of damage leading to eventual failure in the material. In three-dimensional problems, it assumes one direct (through-thickness) strain, two transverse shear strains, and all (six) stress components to be active at a material point. In two-dimensional problems it assumes one direct (through-thickness) strain, one transverse shear strain, and all (four) stress components to be active at a material point [47].

In the case of a traction-separation constitutive behaviour, the macroscopic material properties are not relevant directly, and the analyst must resort to concepts derived from fracture mechanics, such as the amount of energy required to create new surfaces. The cohesive elements model the initial loading, the initiation of damage, and the propagation of damage leading to eventual failure at the bonded interface. The behaviour of the interface prior to initiation of damage is often described as linear elastic in terms of a penalty stiffness that degrades under tensile and/or shear loading but is unaffected by pure compression. The cohesive elements should be used in areas of the model where cracks are expected to develop. However, the model need not have any crack to begin with. In fact, the precise locations (among all areas modeled with cohesive elements) where cracks initiate, as well as the evolution characteristics of such cracks, are determined as part of the solution. The cracks are restricted to propagate along the layer of cohesive elements and will not deflect into the surrounding material. In three-dimensional problems, this type of constitutive behaviour assumes three components of separation: one normal to the interface and two parallel to it; and the corresponding stress components are assumed to be active at a material point. In two-dimensional problems the traction-separation-based model assumes two components of separation: one normal to the interface and the other parallel to it; and the corresponding stress components are assumed to be active at a

material point [47]. In Figure 2.7 is shown a summary comparing the two methods used to model delaminations.

VCCT	Cohesive Elements
Simulation (mechanics)-driven crack propagation along a known crack surface.	Simulation (mechanics)-driven crack propagation along a known crack surface. However, cohesive elements can also be placed between element faces as a mechanism for allowing individual elements to separate.
Models brittle fracture using LEFM only.	Model brittle or ductile fracture for LEFM or EPFM. Very general interaction modeling capability is possible.
Uses a surface-based framework. Does not require additional elements.	Require definition of the connectivity and interconnectivity of cohesive elements with the rest of the structure. For accuracy, the mesh of cohesive elements may need to be smaller than the surrounding structural mesh and the associated "cohesive zone." As a result, cohesive elements may be more expensive.
Requires a pre-existing flaw at the beginning of the crack surface. Cannot model crack initiation from a surface that is not already cracked.	Can model crack initiation from initially uncracked surfaces. The crack initiates when the cohesive traction stress exceeds a critical value.
Crack propagates when strain energy release rate exceeds fracture toughness.	Crack propagates according to cohesive damage model, usually calibrated so that the energy released when the crack is fully open equals the critical strain energy release rate.
Multiple crack fronts/surfaces can be included.	Multiple crack fronts/surfaces can be included.
In Abaqus/Standard crack surfaces are rigidly bonded when uncracked.	Crack surfaces are joined elastically when uncracked in Abaqus/Standard.
Requires user-specified fracture toughness of the bond.	Require user-specified critical traction value and fracture toughness of the bond, as well as elasticity of the bonded surface.

Figure 2.7: Comparison between VCCT and cohesive elements [47].

Chapter 3

Composites

3.1 Introduction

A composite material is a material which combines two or more different materials. The most common composites are composed by fibers and matrices [17].

One of the main reasons for the excellent properties of composites is because, generally, the fibers have superior mechanical properties than other identical compact materials. However the fibers cannot be directly used in structural engineering applications. In fact, the matrix is the main reason of the stable shape of the composites and ensures the efficient load distribution by the fibers. It also protects their surfaces from damage and corrosion and gives specific properties such as tenaciousness, chemical resistance, etc. In table 3.1 it is shown the difference between some fibers properties and some compact material properties [17].

Table 3.1: Difference between fibers properties and compact material properties [17].

Material	Young's Modulus E(GPa)	Tensile Strength σ_u (GPa)	Density ρ (kg/dm^3)	Specific Modulus E/ρ	Specific Strength σ_u/ρ
Fibres:					
Glass E	72	3.5	2.54	28.5	1.38
Glass S	87	4.3	2.49	35.0	1.70
Carbon (Pitch CP)	690	2.2	2.15	321	1.00
Carbon (PAN C)	345	2.3	1.85	186	1.24
Boron	393	3.1	2.70	146	1.15
Silica	72.4	5.8	2.19	33	2.65
Tungsten	414	4.2	19.3	21	0.22
Beryllium	240	1.3	1.83	131	0.71
Kevlar 49	131	3.6	1.45	90	2.48
Conventional materials:					
Steel	210	0.34-2.1	7.8	26.9	0.043-0.27
Aluminium alloys	70	0.14-0.62	2.7	25.9	0.052-0.23
Glass	70	0.7-2.1	2.5	28	0.28-0.84
Tungsten	350	1.1-4.1	19.3	18.1	0.057-0.21
Beryllium	300	0.7	1.83	164	0.38

Composite materials can be classified by several criteria wherein the matrix type is one of the most relevant criterion. There are polymeric, metallic, ceramic and cementitious matrices. Nowadays, the polymeric matrix is one of the most important matrices in terms of performance and application field due to its low density and processability [17].

The fibers which are more used in composites of polymeric matrices are carbon, glass and aramid fibers. On the other hand, the polymeric matrices can be thermoplastics such as polypropylene, polyamide and polyether ether ketone (PEEK) or thermosetting resins of polyester or epoxide.

Since the second part of this thesis uses CFRP (carbon fiber reinforced plastics) as a material, it will only be described in detail the carbon fibers and the thermosetting matrices. It will also be described some processes used in the manufacturing of CFRP.

CFRP is a material which is distinguished by its extremely high strength and rigidity. To complement its complex characteristics profile, the CFRP material has also low density, excellent damping properties and a high resistance to impacting combined with exactly modifiable thermal expansion. This material consists of a polymer employed as a matrix material in which carbon fibers with a diameter of a few micrometers are embedded. Different processes are utilised for the manufacturing of semi-finished products and final products, depending on the geometry and requirement profile involved. These include fiber winding, autoclave pressing, board pressing, resin transfer moulding (RTM, the resin injection method) or manual laminating for individual and small series production.

3.2 Carbon fibers

There are two types of carbon fibers: the carbon fibers with percentages between 80 and 95% and the graphite fibers with percentages up to 99 %. The last ones are applied in high performance composites in areas such as aeronautics and spacial industry [17].

The most recent technology used in the production of carbon fibers focuses on the thermal decomposition of several organic precursors, which are essentially three:

1. the cellulose, which origins the "rayon fibers";
2. the polyacrylonitrile (PAN);
3. the tar ("pitch").

This precursors should have some specific characteristics such as:

- proper strength and handling characteristics in order to maintain the fibers together during all the steps of the conversion process into carbon;
- no melting during any step of the process;
- no volatilize during the pyrolysis process.

Different precursors leads to different carbon fibers with different mechanical characteristics. Nowadays, the polyacrylonitrile is the most commonly used precursor. In Figure 3.1 it is illustrated the process for the manufacture of a PAN based carbon fiber.

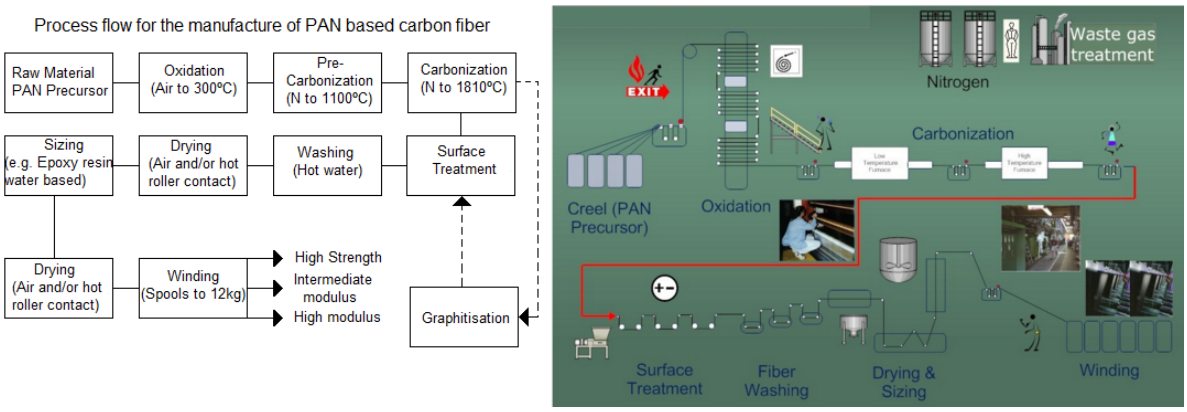

Figure 3.1: Process for the manufacture of PAN based carbon fiber (adapted from [52]).

The carbon fibers are classified based on its mechanical strength and they are marketed according to the following designations:

- UHM (ultra high modulus)for fibers with modulus above 500 GPa;
- HM (high modulus)for fibers with modulus above 300 GPa and mechanical strength-tensile modulus ratio lower than 1 %;
- IM (intermediate modulus) for fibers with modulus up to 300 GPa and mechanical strength-tensile modulus ratio around 1 %;
- for fibers with low modulus, with values lower than 100 GPa.
- HS (high strength) for fibers with tensile strength above 3 GPa and strength-rigidity ratio between 0.015 and 0.02.

There is one important particularity relatively to carbon fibers: in the longitudinal direction the dilatation coefficient is almost negative or null. So when the carbon fibers are associated to materials with positive dilatation coefficient, some damaging stresses at the surface could appear. However some insightful conjugations between the fiber and the matrix, could lead to the production of composite materials with null dilatation coefficient which is useful for applications in the domain of optical metrology and aerospace [17].

3.3 Thermosetting matrices

Unsaturated polyesters, vinylester and phenolic resins are the most common thermosetting resins applied to the manufacturing of non-structural and semi-structural composites. As regards to high resistance composites, epoxides, polyimides and bismaleimides are the most common references. For CFRP IM7/8552 it is used epoxy resin [17].

Epoxy resins have a big chemical formulation variety which most of them are based on the bisphenol A diglycidyl ether (BADGE). The cure scheme of these resins involves the addiction of an appropriate hardening agent such as aromatic and aliphatic amines and some polyamides.

The advantages of this resin are high mechanical strength, abrasion resistance, chemical resistance (specially in alkaline means), good fiber adhesion properties, cure process without release of volatiles, great sizing stability due to its low concentration (2 % up to 3%), low water absorption and operating temperatures between 100 and 200 °C [17].

3.4 Constitutive laws of the layer

The composites of continuum fibers have structural applications of large requirements due to its high strength and rigidity. These materials have a laminated structure which means they are made up of several layers all aligned in the same direction. So the layer is a elementary block whose mechanical behaviour is essential to characterize. Usually the laminates have several layers with different orientations [17].

It is important to mention that the mechanical properties of the fiber and the matrix determine the internal stress distributions and the effective mechanical properties of the layer. It is also important to have models which could predict the properties of the layer according to the content and to the properties of the constituents. So, to study the mechanical behaviour of the layers, which have an huge amount of fibers, they should be considerer as an homogeneous solid. Consequently the strains and stresses considered are medium quantities of a representative volume element whose dimensions are necessarily in the order of magnitude greater than the diameter of the fiber [17].

The behaviour of an homogenized layer model still is more complex than structural materials such as steel and aluminium alloys. In the elastic regime these materials are isotropic which means the constitutive laws are independent of the local orientation while the layer is strongly anisotropic due to the big difference between the properties of the fiber and the matrix. For example the rigidity in the fibers direction is one or two orders of magnitude greater than the rigidity in the perpendicular direction.

3.4.1 General analysis of anisotropic solids

A material point could be subject to a state of three-dimensional stress, characterized by the stress tensor σ_{ij}, i,j=1,2,3. The equilibrium equations dictate the symmetry of the stress tensor [3.1,3.2], this means,

$$\sigma_{ij} = \sigma_{ji}. \tag{3.1}$$

The stresses naturally originates a state of strain, described by the strain tensor, ε_{kl}, which is also symmetric, in other words,

$$\varepsilon_{kl} = \varepsilon_{lk}, \tag{3.2}$$

where, k,l=1,2,3. In most of situations, solids have a linear elastic behaviour and so the relation between strain and stress could be described by

$$\sigma_{ij} = C_{ijkl}\varepsilon_{kl}, \tag{3.3}$$

in which $C_{ijkl}\varepsilon_{kl}$ is the stiffness tensor. Its terms are also called by elastic constants. So, from the symmetry of the stress 3.1 and strain 3.2 tensors,

$$C_{ijkl} = C_{jikl}, C_{ijkl} = C_{ijlk}. \tag{3.4}$$

So, in the matrix form,

$$\sigma = \mathbf{C}\varepsilon, \tag{3.5}$$

or alternatively,

$$\begin{Bmatrix} \sigma_{11} \\ \sigma_{22} \\ \sigma_{33} \\ \sigma_{23} \\ \sigma_{13} \\ \sigma_{12} \end{Bmatrix} = \begin{bmatrix} C_{1111} & C_{1122} & C_{1133} & C_{1123} & C_{1113} & C_{1112} \\ C_{2211} & C_{2222} & C_{2233} & C_{2223} & C_{2213} & C_{2212} \\ C_{3311} & C_{3322} & C_{3333} & C_{3323} & C_{3313} & C_{3312} \\ C_{2311} & C_{2322} & C_{2333} & C_{2323} & C_{2313} & C_{2312} \\ C_{1311} & C_{1322} & C_{1333} & C_{1323} & C_{1313} & C_{1312} \\ C_{1211} & C_{1222} & C_{1233} & C_{1223} & C_{1213} & C_{1212} \end{bmatrix} \begin{Bmatrix} \varepsilon_{11} \\ \varepsilon_{22} \\ \varepsilon_{33} \\ \varepsilon_{23} \\ \varepsilon_{13} \\ \varepsilon_{12} \end{Bmatrix}, \tag{3.6}$$

and contracting the indices,

$$\begin{Bmatrix} \sigma_{1} \\ \sigma_{2} \\ \sigma_{3} \\ \sigma_{4} \\ \sigma_{5} \\ \sigma_{6} \end{Bmatrix} = \begin{bmatrix} C_{11} & C_{12} & C_{13} & C_{14} & C_{15} & C_{16} \\ C_{21} & C_{22} & C_{23} & C_{24} & C_{25} & C_{26} \\ C_{31} & C_{32} & C_{33} & C_{34} & C_{35} & C_{36} \\ C_{41} & C_{42} & C_{43} & C_{44} & C_{45} & C_{46} \\ C_{51} & C_{52} & C_{53} & C_{54} & C_{55} & C_{56} \\ C_{61} & C_{62} & C_{63} & C_{64} & C_{65} & C_{66} \end{bmatrix} \begin{Bmatrix} \varepsilon_{1} \\ \varepsilon_{2} \\ \varepsilon_{3} \\ \varepsilon_{4} \\ \varepsilon_{5} \\ \varepsilon_{6} \end{Bmatrix}. \tag{3.7}$$

Similarly, it is possible to describe the relation between stress and strain by

$$\varepsilon_{ij} = S_{ijkl}\sigma_{kl}, \tag{3.8}$$

where,

$$S_{ijkl} = C^{-1}_{ijkl}, \tag{3.9}$$

is the flexibility tensor. In the matrix form,

$$\varepsilon = \mathbf{S}\sigma, \tag{3.10}$$

or alternatively,

$$\begin{Bmatrix} \varepsilon_{11} \\ \varepsilon_{22} \\ \varepsilon_{33} \\ \varepsilon_{23} \\ \varepsilon_{13} \\ \varepsilon_{12} \end{Bmatrix} = \begin{bmatrix} S_{1111} & S_{1122} & S_{1133} & S_{1123} & S_{1113} & S_{1112} \\ S_{2211} & S_{2222} & S_{2233} & S_{2223} & S_{2213} & S_{2212} \\ S_{3311} & S_{3322} & S_{3333} & S_{3323} & S_{3313} & S_{3312} \\ S_{2311} & S_{2322} & S_{2333} & S_{2323} & S_{2313} & S_{2312} \\ S_{1311} & S_{1322} & S_{1333} & S_{1323} & S_{1313} & S_{1312} \\ S_{1211} & S_{1222} & S_{1233} & S_{1223} & S_{1213} & S_{1212} \end{bmatrix} \begin{Bmatrix} \sigma_{11} \\ \sigma_{22} \\ \sigma_{33} \\ \sigma_{23} \\ \sigma_{13} \\ \sigma_{12} \end{Bmatrix}. \tag{3.11}$$

Apparently, equations 3.6 and 3.11 suggests that is necessary 36 elastic constants to characterize an anisotropic elastic solid. However, this is not the case, and it could be demonstrated using the concept of strain energy density, in other words, strain energy per unit volume,

$$U = \frac{1}{2}\sigma_{ij}\varepsilon_{ij}, \tag{3.12}$$

and from equation 3.3, it can be written,

$$U = \frac{1}{2} C_{ijkl} \varepsilon_{kl} \varepsilon_{ij}. \tag{3.13}$$

When an elastic solid is subjected to several solicitations, U only depends from the final state of deformation, and not from the order in which the several partial deformations are applied. This is described by,

$$\frac{\partial^2 U}{\partial \varepsilon_{ij} \partial \varepsilon_{kl}} = \frac{\partial^2 U}{\partial \varepsilon_{kl} \partial \varepsilon_{ij}} \Leftrightarrow C_{ijkl} = C_{klij}. \tag{3.14}$$

However, taking into account equations 3.4 and 3.9, it also can be written,

$$C_{ijkl} = C_{lkji}, \tag{3.15}$$

and,

$$S_{ijkl} = S_{lkji}. \tag{3.16}$$

So, the flexibility and stiffness matrices are symmetric and the number of independent elastic constants decreases to 21.

3.4.2 Orthotropy and transversal isotropy

The layer of the laminates are orthotropic, which means it has 3 symmetry plans all perpendicular between each others. The lines of intersection of these plans are associated with the main axes of orthotropia 1, 2 and 3. In Figure 3.2 are represented the three axes where axis 1 is in the direction of the fibers and axis 3 is in the perpendicular direction of the layer plane.

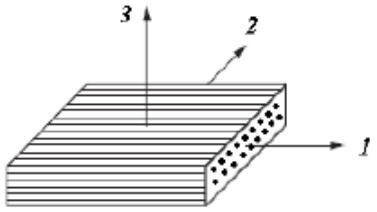

Figure 3.2: Main axes of a given layer [53]

Matrix **S** has several null elements when is expressed in 123 reference, and its nonzero terms are related to the engineering constants, in other words, they are related to the elastic modulus and poisson's ratio. To demonstrate these particularities, it is necessary to use the law of the tensor transformations, using the referential rotation. Thus, it is possible to obtain the {xyz} stress tensor, σ'_{pq} from the {123} stress tensor, σ_{kl}, where

$$\sigma'_{pq} = a_{pk} a_{ql} \sigma_{kl}, \tag{3.17}$$

and,

$$a_{pk} = \cos(e_k, e_p), \tag{3.18}$$

is the cosine of the formed angle between the axes which corresponds to p and k indices. For example, if {xyz} is obtained from {123} by rotation of an angle θ around 3, in the matrix form this could be described as

$$\begin{Bmatrix} \sigma_{xx} \\ \sigma_{yy} \\ \sigma_{zz} \\ \sigma_{yz} \\ \sigma_{xz} \\ \sigma_{xy} \end{Bmatrix} = \begin{bmatrix} c^2 & s^2 & 0 & 0 & 0 & 2cs \\ s^2 & c^2 & 0 & 0 & 0 & -2cs \\ 0 & 0 & 1 & 0 & 0 & 0 \\ 0 & 0 & 0 & c & -s & 0 \\ 0 & 0 & 0 & s & c & 0 \\ -cs & cs & 0 & 0 & 0 & c^2 - s^2 \end{bmatrix} \begin{Bmatrix} \sigma_{11} \\ \sigma_{22} \\ \sigma_{33} \\ \sigma_{23} \\ \sigma_{13} \\ \sigma_{12} \end{Bmatrix}, \tag{3.19}$$

where,

$$c = \cos\theta \quad and \quad s = \sin\theta. \tag{3.20}$$

The strain tensor components could be written as,

$$\varepsilon'_{mn} = a_{mi} a_{nj} \varepsilon_{ij}. \tag{3.21}$$

So, in order to obtain S'_{mnpq} from S_{ijkl}, in a way that

$$\varepsilon'_{mn} = S'_{mnpq} \sigma'_{pq}, \tag{3.22}$$

it is possible to obtain

$$\varepsilon_{ij} = [(a_{mi} a_{nj})^{-1} (a_{pk} a_{ql})^{-1} S'_{mnpq}] \sigma_{kl}, \tag{3.23}$$

and therefore,

$$S'_{mnpq} = a_{mi} a_{nj} a_{pk} a_{ql} S'_{\mathrm{ijkl}}. \tag{3.24}$$

In the case that $\{1'2'3'\}$ is obtained from {123} and through a rotation of $\theta = 180°$ around 3, it is clear that elastic constants must be equal in both references.

Analysing all the terms and considering also the axis 1 and 2, it would be concluded the existence of only 9 elastic constants (equation 3.25).

$$S = \begin{bmatrix} S_{1111} & S_{1122} & S_{1133} & 0 & 0 & 0 \\ & S_{2222} & S_{2233} & 0 & 0 & 0 \\ & & S_{3333} & 0 & 0 & 0 \\ & & & S_{2323} & 0 & 0 \\ & Symmetric & & & S_{1313} & 0 \\ & & & & & S_{1212} \end{bmatrix} \tag{3.25}$$

Indeed, the fibers are randomly distributed in the transverse plane <23> and that is way the layer presents transverse isotropy which means the elastic constants are independent from the axis orientation in the plane <23>. Therefore, the layer has only 5 elastic constants [17].

3.4.3 Engineering constants of the layer

Considering a rectangular element layer subjected to a tractive stress σ_{11}, and knowing that the element undergoes a deformation, it is possible to obtain,

$$\varepsilon_{11} = S_{1111}\sigma_{11}. \tag{3.26}$$

Knowing that elastic modulus is the ratio between a stress and a deformation, the longitudinal elastic modulus is defined as

$$E_1 = \frac{\sigma_{11}}{\varepsilon_{11}} = \frac{1}{S_{1111}}. \tag{3.27}$$

Considering that the rectangular element has also transverse deformations ε_{22} and ε_{33}, it is possible to define the Poisson's ratio as:

$$\nu_{12} = -\frac{\varepsilon_{22}}{\varepsilon_{11}}, \quad \nu_{13} = -\frac{\varepsilon_{33}}{\varepsilon_{11}}. \tag{3.28}$$

It is possible to obtain equation 3.29 from equations 3.11 , 3.25 and 3.27.

$$S_{2211} = -\frac{\nu_{12}}{E_1}, \quad S_{3311} = -\frac{\nu_{13}}{E_1}. \tag{3.29}$$

Similarly, it is possible to define the transverse elastic modulus E_2 and E_3 and poisson's ratio ν_{21}, ν_{23}, ν_{31} and ν_{32}.

Considering now a rectangular element layer subjected to a shear stress τ_{12}, and knowing that the shear modulus is the ratio between a shear stress and a shear strain, it is possible to obtain the longitudinal shear modulus

$$G_{12} = \frac{\tau_{12}}{\gamma_{12}}. \tag{3.30}$$

So, from equations 3.11 and 3.25,

$$S_{1212} = \frac{1}{2G_{12}}. \tag{3.31}$$

Equation 3.32 is easily obtained by the analysis of other cases.

$$S = \begin{bmatrix} \frac{1}{E_1} & -\frac{\nu_{21}}{E_2} & -\frac{\nu_{31}}{E_3} & 0 & 0 & 0 \\ S_{2211} & S_{2222} & S_{2233} & 0 & 0 & 0 \\ S_{3311} & S_{3322} & S_{3333} & 0 & 0 & 0 \\ 0 & 0 & 0 & S_{2323} & 0 & 0 \\ 0 & 0 & 0 & 0 & S_{1313} & 0 \\ 0 & 0 & 0 & 0 & 0 & S_{1212} \end{bmatrix}. \tag{3.32}$$

From the symmetry character of $\mathbf{S}$,

$$\frac{\nu_{ij}}{E_i} = \frac{\nu_{ji}}{E_j}, \tag{3.33}$$

while in transverse isotropy:

$$E_3 = E_2; \quad \nu_{13} = \nu_{12}; \quad G_{13} = G_{12}; \quad G_{23} = \frac{E_2}{2(1+\nu_{23})}. \tag{3.34}$$

Therefore, E_1, E_2, ν_{12}, G_{12} and ν_{23} or G_{23} are all the elastic constants needed to characterized the stress-strain behaviour of the layer [17].

3.5 Glued connections

3.5.1 Introduction

Glued connections consist in joining two elements, usually known by adherends, through an adhesive. This type of connection have several advantages when compared to other joining techniques with holes [17]. This advantages are:

- Load distribution over a larger surface, which decreases the stress concentration and, consequently, it provides a better performance under fatigue requests;
- The viscoelastic nature of the adhesive promotes the vibration damping;
- Economy in the number of parts and weight;
- Ability to seal and for thermal insulation;
- Prevents galvanic corrosion that occurs in the connection of different materials (metallic adherends);
- It is more readily adaptable to the junction of irregular surfaces;
- It allows obtaining smooth contours, which is very important regarding aerodynamic and aesthetic aspects;
- Usually, it is a more economic and fast process.

However, there are some disadvantages too. They are:

- The surfaces need pretreatment and cleaning;
- The curing cycles of some adhesives take too much time and/or require the application of pressure and temperature;
- Sensitivity to environmental factors, such as, temperature, humidity and ultraviolet radiation;
- Difficult inspection for joint quality check;
- Creation of permanent connections which means there is no way to dismantle the components without damaging or destroying them;
- Bad performance under pull out request;
- Manufacturing process that needs more rigid control and well trained manpower;
- Health problems due to toxicity and security problems inherent to the flammability of most adhesives.

The most common types of joints are illustrated in Figure 3.3. The most frequent joint used, for its simplicity of execution, is the simple lap, where the loads are transmitted between adherends by means of shear stresses in the adhesives [17].

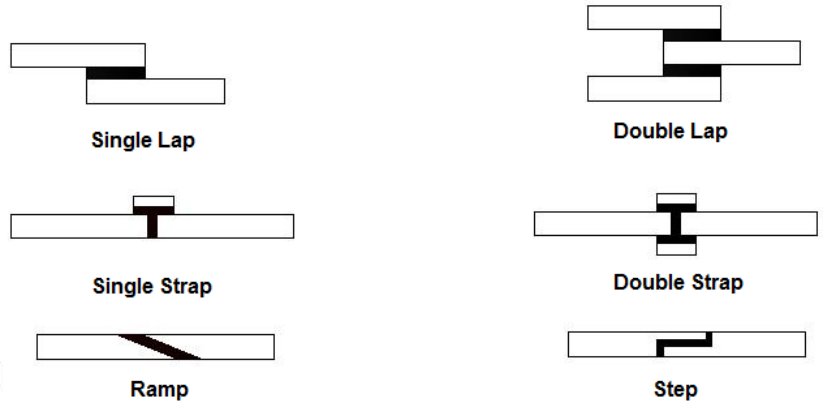

Figure 3.3: Most common types of joints (adapted from [17]).

However, the off-center load application causes bending effects, which lead to the appearance of normal stresses in the thickness direction of the adhesive, decreasing the joint strength [17]. In Figure 3.4 is illustrated this effect.

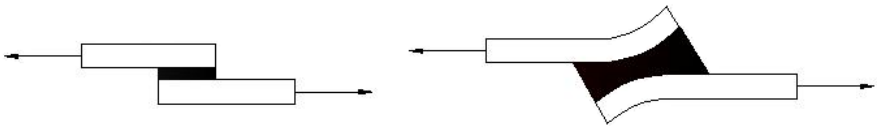

Figure 3.4: Schematic representation of the single lap deformed shape (adapted from [17]).

3.5.2 Failure modes

In general, there are three different failure modes regarding glued connections in composite materials: cohesive failure within the adhesive, adhesive failure at the interface between the adherend and the adhesive and failure in one of the adherends. The cohesive failure occurs when the bond between the adhesive and the adherend is stronger than the internal strength of the adhesive itself. Some authors defend that the adhesive failure would only occur if there was a bad pre-treatment of the surfaces. However, recent studies have shown that, in glued connections of single lap, there is a variation of stresses along the thickness of the adhesive, and the maximum values of stresses occur at the surface. This can explain the frequent appearance of adhesive failure. The failure in one of the adherends is demonstrative of a joint well designed, particularly if the ultimate load correspond to the nominal strength of the adherend. In Figure 3.5 it is illustrated the failure modes of the glued connections.

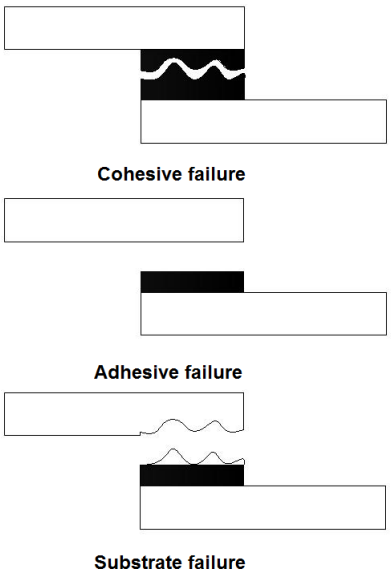

Figure 3.5: Schematic representation of the failure modes in glued connections (adapted from [17]).

Regarding to glued connection of simple lap, there are points of stress concentration at the end of the lap region, particularly in the three normal components and in the shear component τ_{xy}. These stress peaks also affect the adhesive neighbouring layers and can cause interlaminar failure [17].

Chapter 4

Case studies of aluminium stiffened panels

4.1 Introduction

As it was mentioned before, the panels studied in this section were already studied in detail by Paulo in [1] and so there was not a detailed study in this thesis. As in reference [1], two different types of panels were considered for the simulations but only the ones with supported edges.

The methodology to study this type of panels starts with an eigenvalue analysis in order to extract the buckling modes to used them as imperfections for later introduce them in the nonlinear analysis. In the case of these panels the nonlinear analysis will be made using Riks methods while in the next section the method that will be used is the stabilize method.

After the analysis, all the simulations will be compared with the results obtained by Paulo and also with the experimental results [1]. It will be compared the final deformed shapes of the panels and the ultimate load.

The study will be focus on the results shown in [30], i.e., it will only be carried out simulations for the first mode of the eigenvalue analysis in the case of model L and for the nineteenth mode in the case of model TR. Also, as it was recommended in [1], it will be carried out simulations for S8R element type for both models. Regarding the number of elements, TR model has 4950 elements and L model has 4320 elements.

Regarding to the imperfections, it will be carried out simulations for the imperfections with magnitude of 0.25, 0.50, 1, 2 and 4 mm in case of model L and in case of model TR it will be carried out simulations for the imperfections with magnitude of 0.25, 0.50, 1 and 2 mm. They will be tested only for the positive direction of the Oz axis.

4.2 Numerical Simulation

4.2.1 Geometry

As it was mentioned before, two different types of panels were studied. One of them is a model with trapezoidal stiffeners (model TR) and the other with L-shaped stiffeners (model L).

Following this, it was created a 3D, deformable shell part, where in Figures 4.1 and 4.2 are illustrated the cross sections of the stiffeners profile. Since the models of the panels were created using shell elements, they are represented by their mid-section profile [30].

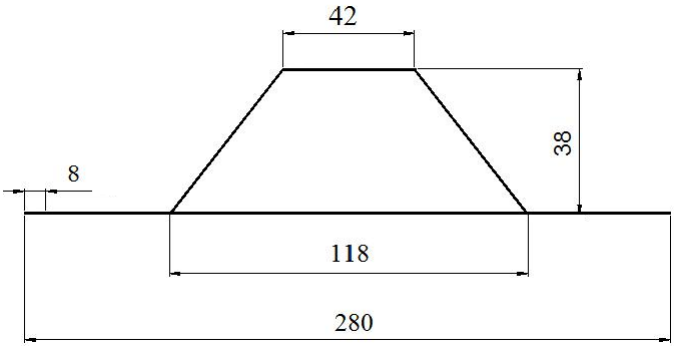

Figure 4.1: Cross section of the model TR (dimensions in mm).

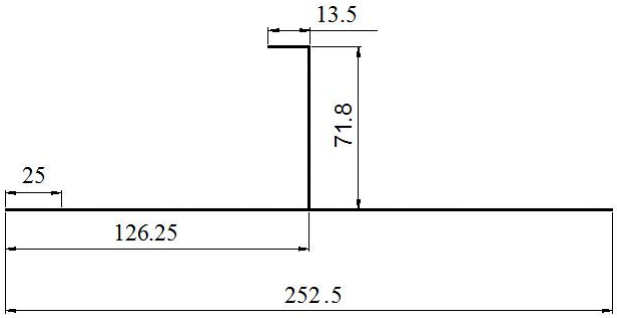

Figure 4.2: Cross section of the L-shaped stiffener (dimensions in mm).

Five stiffeners for L-shaped panel was taken into account while only half of the model TR was considered, and they were joined by welding. The length of the panels is 957 mm for model L and 995 mm for model TR.

One specification of these models was the creation of a rigid wall for the loaded and opposite edges. To define these rigid walls it was used the constraint rigid body present in Abaqus. It was necessary to create a reference point with a position approximately corresponding to the bearing axis of the supported beams of the panels. In the case of L-shaped stiffener, the reference point was moved up 2.2 mm (along the positive Oz direction), in order to force the plates to globally buckle in the negative direction for all the initial imperfections tested. The reference point was also used to measure the displacement of the rigid wall along the Ox axis.

In Figure 4.3 are illustrated both TR and L models, with the representation of the reference point, and also the thicknesses of the different parts of the panels. For TR model only half of the panel was considered because of its symmetry and to be able to compare the results with Paulo's results.

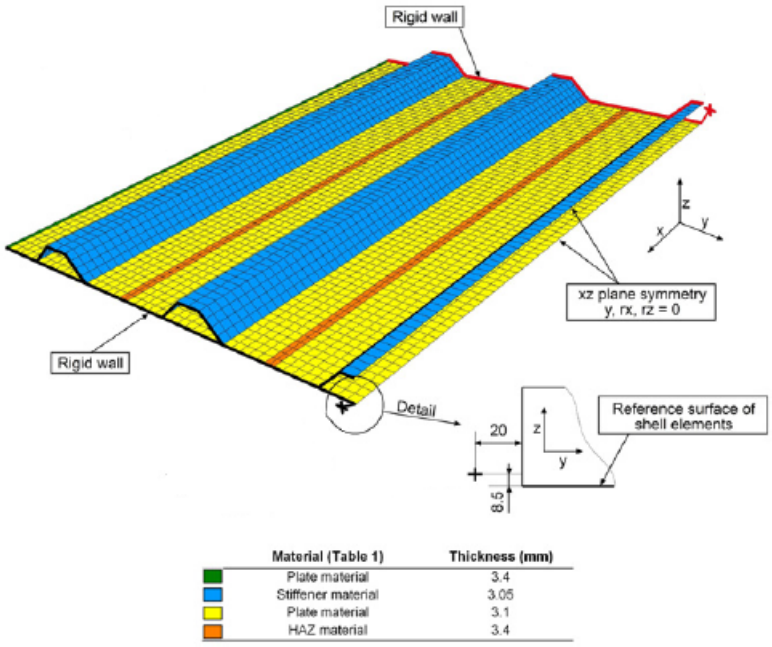

(a)

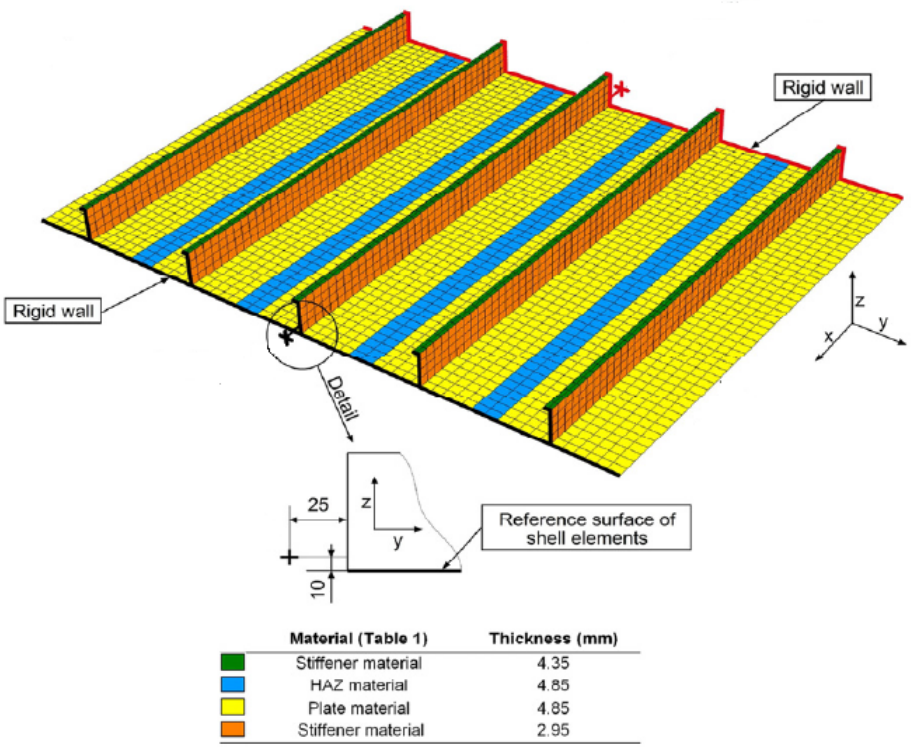

(b)

Figure 4.3: Detailed description for models: a) TR and b) L [30].

4.2.2 Material properties

The panels were built with extruded aluminium profiles in alloy AA6082 temper T6 and joined together by welding. The model with L-shaped stiffeners was welded by MIG welding while the model with trapezoidal stiffeners was welded by friction stir welding (FSW).

The plastic properties of the material for L and TR models are listed in table 4.1. The elastic properties for both TR and L models are the same and are listed in tables 4.2 [30].

Table 4.1: Plastic properties of L and TR models [30].

	Eq. plastic strain	Effective stress (MPa)
Model L plate	0	265
	0.06	298
Model L stiffener	0	284
	0.06	317
Model TR plate	0	261
	0.06	294
Model TR stiffener	0	275
	0.06	308
HAZ	0	135
	0.007	160
	0.027	200
	0.047	220
	0.067	200

Table 4.2: Elastic properties [30].

E (GPa)	ν
64.5	0.3

As it was shown by Paulo in [1], at least 4950 elements were needed for the model TR, while 4320 elements were needed for the model L. These choices assumed that S8R element formulation were chosen (shell element with 8 nodes and reduced numerical integration), in order to have a good accuracy in the ultimate load prediction and also in the post-collapse behaviour. So, in the present work, the simulations were carried out using the same meshes and the same formulations used by Rui Paulo in order to be able to compare results. It was also taken into consideration, for both cases, 5 integration points along the thickness direction of the structure in order to correctly predict the through-thickness stress and strain fields.

4.2.3 Load and boundary conditions

The boundary conditions that were considered in the numerical simulation models are illustrated in figures 4.4 and 4.5 and they were based on [30]. In tables 4.3 and 4.4 can be seen the boundary conditions applied in Abaqus, of models TR and L, respectively.

Those boundary conditions took into account the coordinate system of the simulations of this thesis that could be seen in Figure 4.5. Since two rigid walls were created, one in the edge where the load is applied and another one opposite to that edge, the loads and boundary conditions were applied to the reference points of the rigid walls. As it was mentioned before it was only tested the models with supported edges.

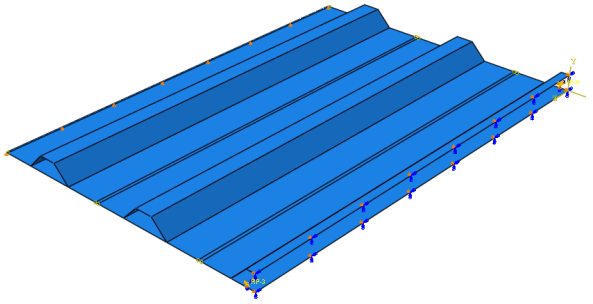

Figure 4.4: Load and boundary conditions applied in model TR.

Table 4.3: Boundary Conditions for model TR with supported edges [30].

RP-1	u1=u2=ur2=ur3=0
RP-2	u1=u2=u3=ur2=ur3=0
Supported edge	u2=0
Symmetric edge	u1=ur2=ur3=0

The reference point RP-1 of model TR is allowed to only move in direction of *Oz* axis and to rotate around *Ox* axis. RP-1 represents the reference point where the load is applied. In the reference point RP-2 all the degrees of freedom are restrained with exception of the rotation around Ox axis. RP-2 represents the reference point opposite to the edge where the load is applied.

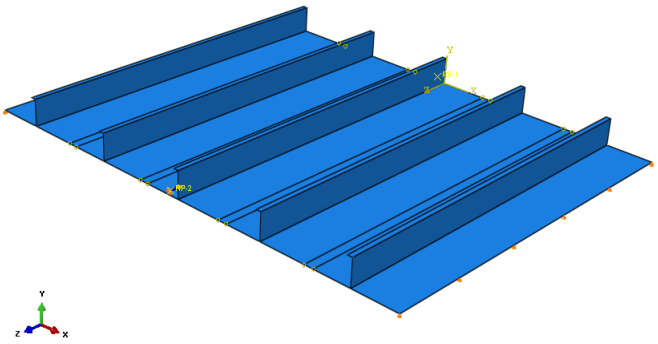

Figure 4.5: Load and boundary conditions applied in L-shaped stiffener.

Table 4.4: Boundary Conditions for model L with supported edges [30].

RP-1	u1=u2=u3=ur2=ur3=0
RP-2	u1=u2=ur3=0
Both lateral edges	u2=0

In the reference point RP-1 of model L all the degrees of freedom are restrained with exception of the rotation around Ox axis. RP-1 represents the reference point opposite to the edge where the load is applied. In the reference point RP-2 only is permitted to move in direction to the Oz axis and to rotate around Ox and Oz axis. RP-2 represents the edge where the load is applied.

The loads applied to the models were extracted from previous eigenvalue analysis.

4.3 Results

The results from the simulations and its comparison with the results obtained by Paulo in [30] are presented in this section. As it was mentioned before, only the results for the imperfections with magnitude 0.25, 0.50, 1, 2 and 4 for model L and with magnitude 0.25, 0.50, 1 and 2 for model TR are compared. Also the results from the eigenvalue analysis will be compared for the models with supported edges.

In Figure 4.6 is illustrated the comparison between the eigenvalue analysis obtained by Paulo in [1] and the eigenvalue analysis obtained from this study, for model L with supported edges. The results are pretty similar and the values of the critical loads for both eigenvalues are 692 kN and 691.819 kN for the first and second pictures, respectively. It is possible to see that both deformed shapes are very similar as also the values of the critical loads.

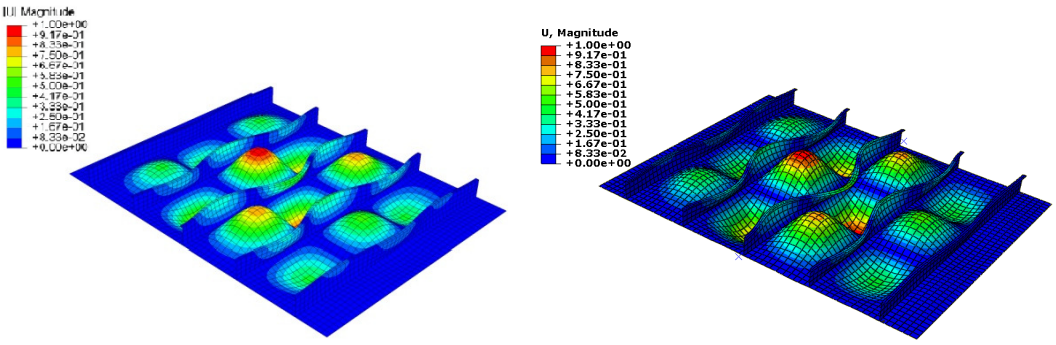

(a) First eigenvalue obtained by Paulo [1]. (b) First eigenvalue obtained in this study.

Figure 4.6: Comparison between the deformed shapes of the eigenvalues for model L.

In Figure 4.7 is illustrated the comparison between the deformed shapes obtained by Paulo and the deformed shaped obtained in this study for all the magnitudes of imperfections for model L. Once again the deformed shapes are very similar as it was expected. It is possible to see that all the stringers collapsed as happened in Paulo simulations.

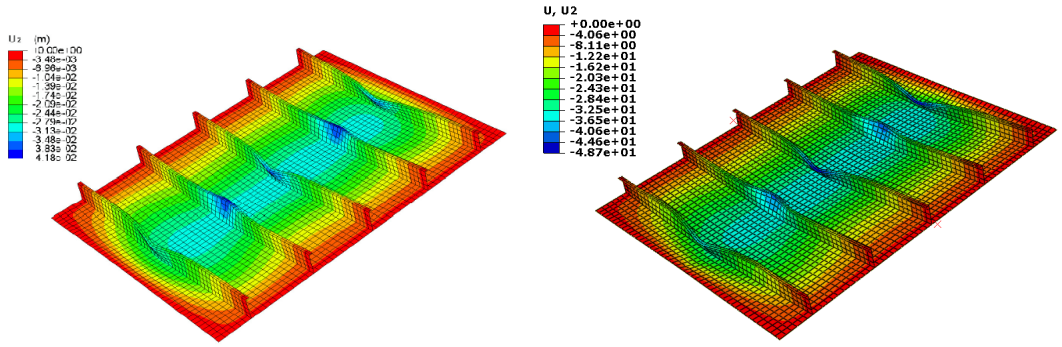

(a) Result obtained by Paulo for all magnitudes of imperfections [1].

(b) Result obtained from this study for all magnitudes of imperfections.

Figure 4.7: Comparison between the deformed shapes for all the magnitude of imperfections of model L.

The load vs displacement curves are compared for all the imperfections in Figure 4.8 for model L. For clear interpretation of the curves, the legend regarding EV1 model refers to the results obtained by Paulo. As it was expected, the ultimate load decreases with the increasing of the magnitude of imperfections. However there are slight differences between the results obtained by Paulo and the results obtained in this thesis. The ultimate load is slightly smaller and the curve tends slightly for the right side.

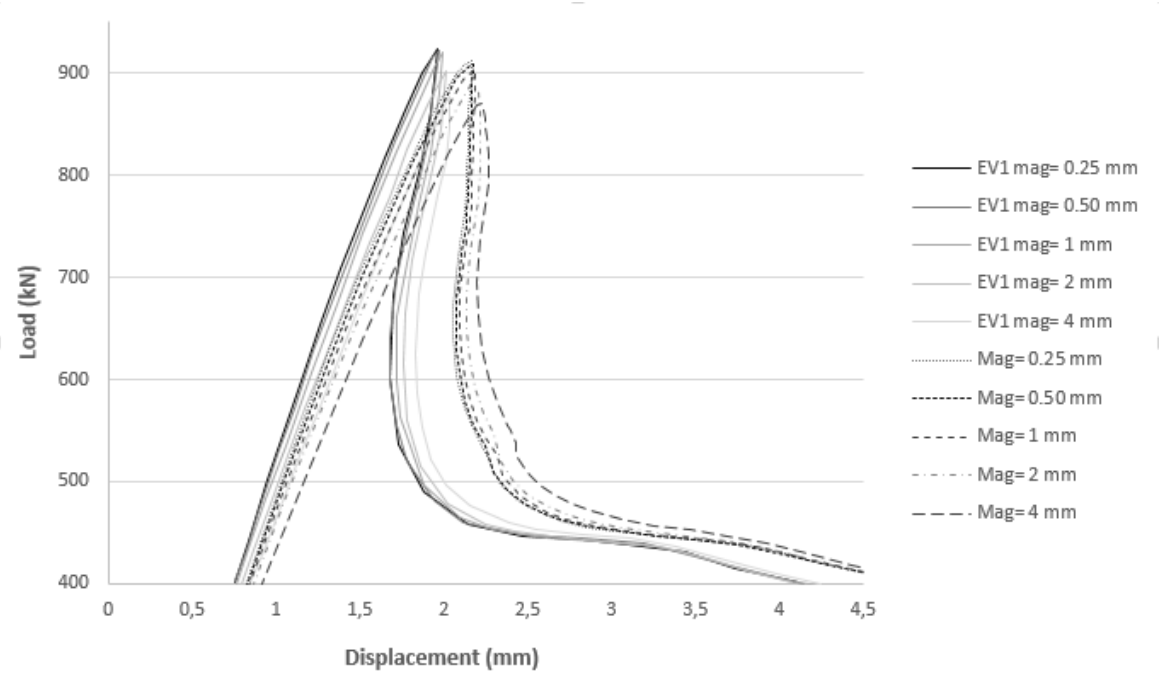

Figure 4.8: Load vs displacement curves for model L with supported edges. Comparison with results obtained by Paulo [1].

In Figure 4.9 is shown the comparison between the load vs displacement curves for

the experimental results and the results obtained in this study. Once again, for clear interpretation of the curves, the legend regarding K, L and M models refers to the experimental results. As happened with Paulo, it is possible to see in the load vs displacement curve that after the post-collapse phase, there is a slight decreased in the displacement with the decreasing of the load. This does not happen in the load vs displacement curve of the experimental results, where it is possible to see that after the post-collapse phase the progress is unidirectional and constant. This can be explained by the calculation method of Abaqus since other authors achieved similar results for the same type of panels and with the same software. It is also possible to see that the K curve match with the beginning of the curve of magnitude equal to 2 mm and the same happened to the L curve which matches with the beginning of the curve of magnitude equal to 4 mm.

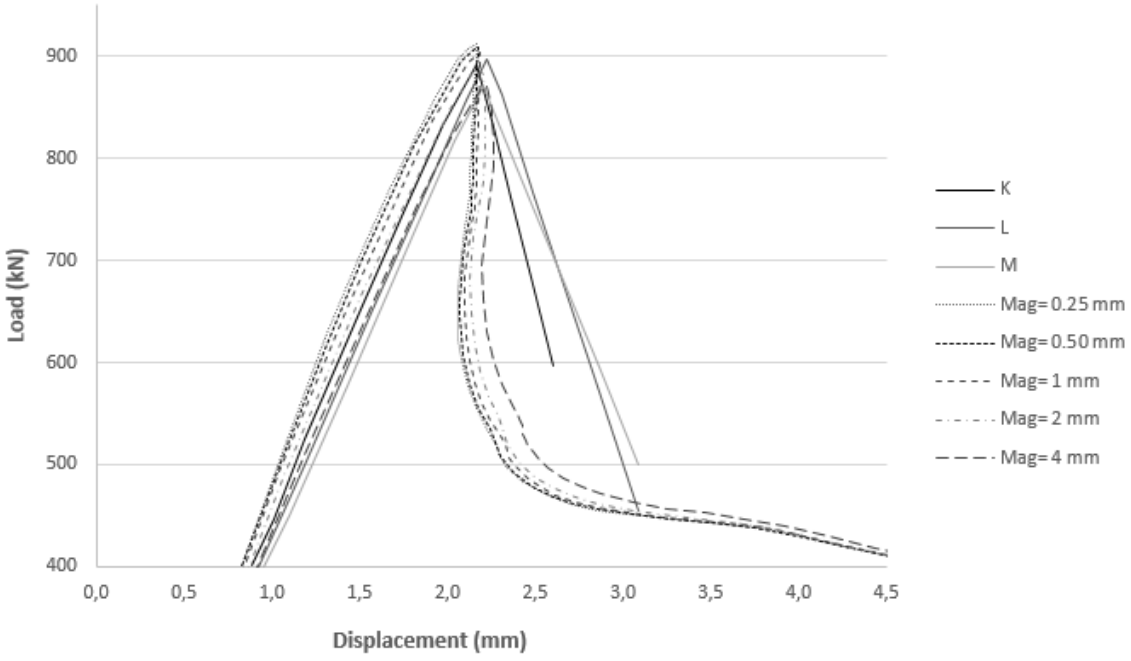

Figure 4.9: Longitudinal displacement vs load curves for model L with supported edges. Comparison with experiment results.

Regarding to the eigenvalue analysis of the model TR with supported edges, in Figure 4.10 is illustrated the results obtained by Paulo and the results obtained in this study. The results in this case are very similar regarding the deformed shape however the values of the critical loads for both eigenvalues are not so approximated and they are 1099 kN and 1085 kN for the first and second pictures, respectively.

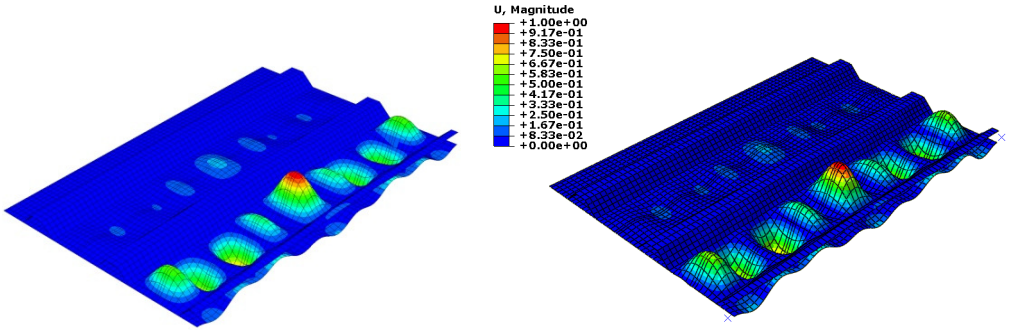

(a) Nineteenth eigenvalue obtained by Paulo [1].

(b) Nineteenth eigenvalue obtained in this study.

Figure 4.10: Comparison between the deformed shapes of the eigenvalues for model TR.

While the deformed shapes for model L were equal for all the imperfections, in the case of model TR that does not happen. For the imperfections with magnitudes of 0.25 and 0.50 the deformed shape is equal but for the imperfections with magnitudes of 1 and 2 the deformed shaped is different. In Figure 4.11 it is shown the comparison between the deformed shapes obtained by Paulo and the deformed shapes obtained in this study, for the magnitudes of imperfections equal to 0.25 and 0.50. It is possible to see that the deformed shapes are very similar.

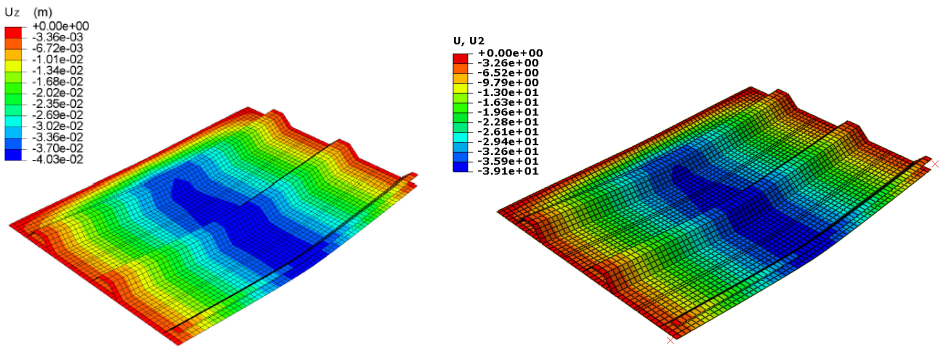

(a) Result obtained by Paulo [1].

(b) Result obtained from this study.

Figure 4.11: Comparison between the deformed shapes for model TR for the magnitude of imperfections equal to 0.25 and 0.50.

In Figure 4.12 it is shown the comparison between the deformed shapes obtained by Paulo and obtained in this study for the magnitude of imperfections equal to 1 and 2. Once again the deformed shapes are very similar.

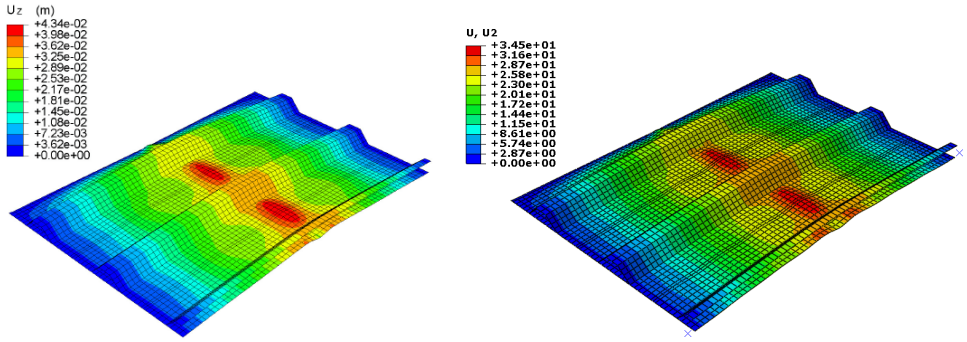

(a) Result obtained by Paulo [1]. (b) Result obtained from this study.

Figure 4.12: Comparison between the deformed shapes for model TR for the magnitude of imperfections equal to 1 and 2.

In Figure 4.13 is illustrated the comparison between the load vs displacement curves obtained by Paulo and the load vd displacement curves obtained in this study for all magnitude of imperfection. The legend regarding EV19 curves refers to the results obtained by Paulo. It is possible to see that the curves almost match with slight differences in the ultimate load. In Table 4.5 is possible to have a better perception of the differences between the ultimate loads.

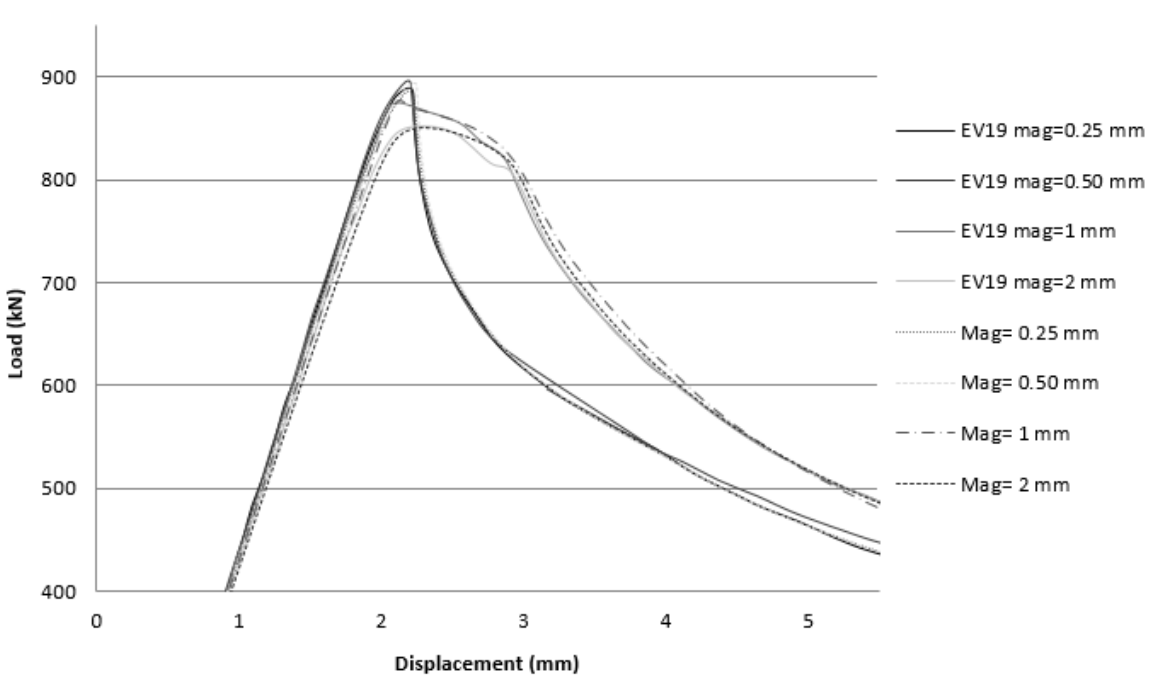

Figure 4.13: Load vs displacement curves for model TR with supported edges. Comparison with results obtained by Paulo.

In Figure 4.14 is illustrated the comparison between the experimental load vs displacement curves and the load vs displacement curves obtained in this study for all

magnitude of imperfection. The legend regarding E,F and G models refers to the experimental results. It is possible to see that the experimental curves tends a little bit to the right side. Also the curves for magnitude of imperfection equal to 1 and 2 shows a significantly horizontal area closer to the ultimate load as it happen with the experimental curve G.

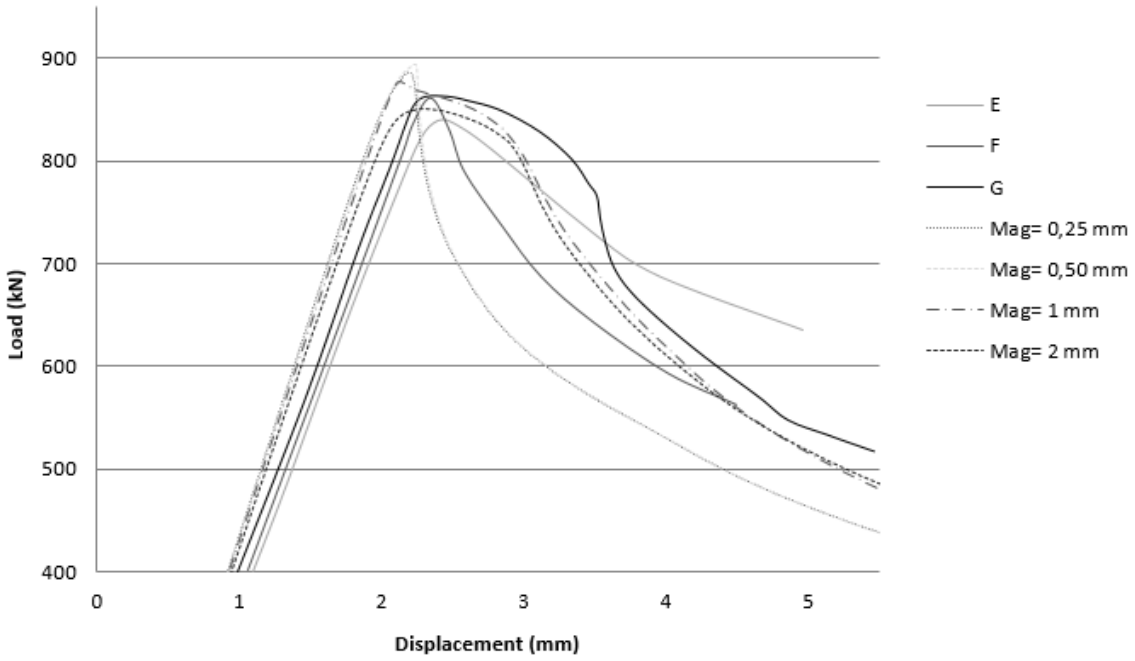

Figure 4.14: Load vs displacement curves for model TR with supported edges. Comparison with experimental results.

In Table 4.5 is shown a summary of the ultimate loads obtained in this thesis for all the magnitude of imperfections and its comparison with the ultimate loads obtained by Paulo in his study.

Table 4.5: Comparison between the ultimate loads for all the magnitude of imperfections.

Model	Magnitude of imperfections (mm)	Ultimate load (kN)	
		Ref.	
L	0.25	926.4	911.3
	0.50	924.0	908.9
	1	921.6	902.9
	2	904.8	889.5
	4	878.4	869.7.9
TR	0.25	883.2	887.7
	0.50	895.2	894.3
	1	871.2	877.9
	2	849.2	850.5

4.4 Summary of results

The main objective of this section was to achieve the necessary skills to study stiffened panels and so there is no big differences between the methodologies used by Paulo in [1] and the methodologies used in this thesis. The geometry of the models, the material, the boundary conditions and the number and type of elements are the same. It is possible to say that the goal was achieved since the results are pretty similar.

Comparing the results obtained by Paulo [1] and the results obtained in this thesis, they are pretty similar. The deformed shapes of both TR and L models are similar however there are slight differences in the load vs displacement curves and in the ultimate load. Regarding to model L, the load vs displacement curve obtained in this study, presents a similar behaviour although it begins slightly to the right side and the ultimate load is slightly smaller. As it was shown by Paulo [1], almost all the load vs displacement curves tends to the right side of the graphic and the ultimate load tend to decrease with the increase of the magnitudes of imperfections. The same tendency was shown in this thesis in Figure 4.9. Regarding to model TR, the load vs displacement curves almost match with the exception of the ultimate load which is a little bit higher in some cases. Beside that the curves have exactly the same behaviour.

It is possible to conclude that the magnitude of imperfections can considerably affect the performance of the stiffened panels. In general, the ultimate load tend to decrease with the increase of the magnitude of imperfections.

Chapter 5

Stiffened CFRP curved panel

5.1 Introduction

In this section it will presented a model of a stiffened carbon fiber reinforced plastic (CFRP) curved panel and it will be explained all the methodologies involved to analyse it. The model is based on the POSICOSS project (FP5) which means "Improved POst-buckling SImulation for Design of Fibre COmposite Stiffened Fuselage Structures" [55]. This is a project under the co-ordination of DLR, Institute of Composite Structures and Adaptive Systems, and their main goal is the exploitation of considerable reserves in primary fiber composite fuselage structures through an accurate and reliable simulation of postbuckling up to collapse. In order to validate the results, they created new experimental data, designing and testing the panels under their own project objectives.

In the present work the main goal is to achieve a good agreement with the experimental results and to show the influence of all the parameters involved to simulate this type of panels. To study these type of panels, the non-linear analysis the build-in Newton-Raphson technique with adaptive/artificial damping factor was used. To employ this method in Abaqus, the STABILIZE command was used. Four damping factor values using the constant damping factor approach were tested. It was also compared the influence of the buckling modes, the number and type of elements and the magnitude of imperfections. Regarding the number of elements, three and five different meshes were tested for panels P10 and P12 respectively. S4R and S4 element formulations were tested for both models. The magnitude of imperfections varied from 10 % up to 95 % of the thickness of the skin. Afterwards, in order to validate the results, they will be compared to the experimental results showed in the literature [55].

5.2 Experimental tests

The experimental tests were performed in the buckling test facility of the Institute of Composite Structures and Adaptive Systems of DLR. The test device used to perform the tests is extremely stiff. In order to perform the tests, a test specimen is located between an axially supporting top plate and a lower drive plate, in which the top plate can be moved in the vertical direction, on three spindle columns in order to adapt the test device to several lengths of test specimens. It is fixed during the tests and reacts the axial force that is applied to the movable lower drive plate by a servo-controlled

hydraulic cylinder. The drive plate acts against the specimen, which itself acts against a stout load distributor that is meant to distribute three concentrated forces. Torsion to cylindrical structures is applied at the load distributor by an electrical drive, and a torsion support at the lower edge of the test specimen reacts against it. In Figure 5.1 it is shown a picture of the buckling test facility [55].

Figure 5.1: Buckling test facility [55].

Despite the test device and test specimens were manufactured with particular care, it cannot be expected that all loaded elements are absolutely plane and parallel. Therefore, to make sure the test specimens are uniformly loaded, thin layers of a kind of epoxy concrete are applied between the clamping boxes of the test specimen and the adjacent parts of the test device. This has the effect of securing the test specimen against lateral displacement [55].

Two displacements transducers are used to measure axial shortenings of the specimen during the tests, and their signals are recorded and moreover used for control purposes. The nominal data of the facility is given in Table 5.1 [55].

Table 5.1: Nominal data of the buckling test facility [55].

Maximum axial compression	1000 kN
Maximum torsion moment	50 kN m
Maximum specimen length	1600 mm
Maximum specimen width (diameter)	1200 mm

The preparation of the structures for the buckling tests started by casting the panel into preliminary end boxes, hardening the end blocks and detaching from the boxes, as it can be seen in Figure 5.2 a). After, the end block edges were milled in order to obtain plane surfaces perpendicular to the panel axis. The imperfections of the panel shape

and the realised radius were then measured, as the radial deviations from the perfect cylindrical shape. The next step was the application of strain gauges and the changing of stress-free casting into final end boxes (Figure 5.2 b)). After, it were applied supports to the longitudinal edges as it can be seen in Figures 5.2 c) and d), and the strain gauges were connected to cables. The final steps were the assembling to the buckling test facility and the application of position encoders.

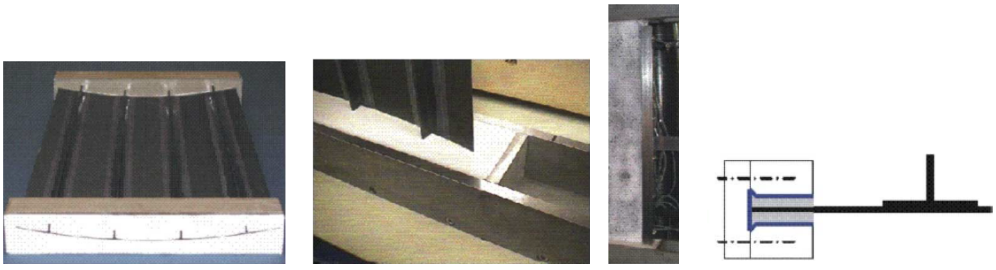

(a) (b) (c) (d)

Figure 5.2: Preparation of the test structures [55].

5.3 Numerical Simulation

5.3.1 Geometry

The main design objective within this model is to obtain a significant postbuckling area before collapse [56]. In reference [55] there is detailed information about the different designs and their influence on the postbuckling behaviour. In the present work, two different models will be analysed to compare the influence of the design in the postbuckling area before collapse. In table 5.2 it is shown the geometrical data for the two chosen designs.

Table 5.2: Nominal geometrical data and lay-up for the panel designs [55].

Nominal geometry/lay-up	Models	
	$PanelP10$	$PanelP12$
Panel length (mm)	l=780	l=780
Free length (buckling length) (mm)	$l_f = 660$	$l_f = 660$
Radius (mm)	r= 1687.5	r= 1069
Arc length (mm)	a=419	a=419
Number of stringers	n=3	n=4
Distance stringer to stringer	$d = a/3$	$d = a/4$
Distance stringer to longitudinal edge	$e = a/6$	$e = a/8$
Laminate set-up of skin	$[+45, -45, 0]_s$	$[90, +45, -45, 0]_s$
Laminate set-up of stringers (cf. Fig. 5.3)		
Blade	$[(+45, -45)_3, 0_6]_s$	$[(+45, -45)_3, 0_6]_s$
Flange	cf. Fig. 5.3	cf. Fig. 5.3
Ply thickness (mm)	t=0.125	t=0.125
Stringer height (mm)	h=14	h=14
Stringer width (mm)	f=34	f=34

The big difference between both models are the radius which is bigger for panel P10, the number of stringers where panel P12 has one more stringer and the laminate set-up of skin where panel P12 has one more layup. The stringers are equal for both models. In Figure 5.3 a) it is illustrated the stringer type and in Figure 5.3 b) it is illustrated the skin-stringer connection.

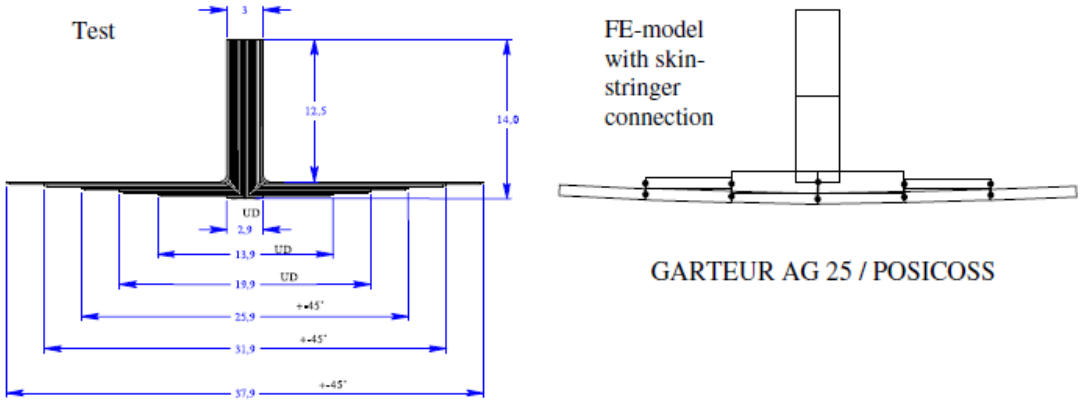

(a) Stringer type (b) Skin-stringer connection

Figure 5.3: Stringer modelling [56].

It was created a 3D deformable shell part to model the skin and stringers. To model the stringer type, partitions were made to create the six sections in the stringer. In Figure 5.4 is illustrated those six sections. The skin-stringer connection was made using TIE constraints, connecting the nodes shown in Figure 5.3 b).

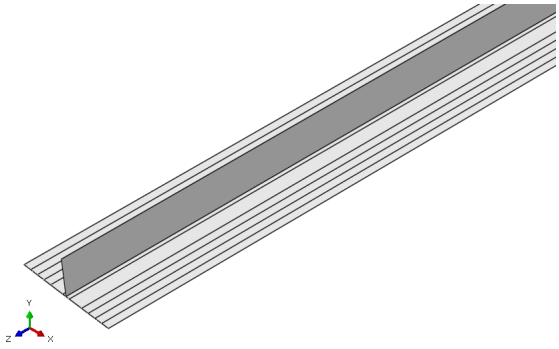

Figure 5.4: Stringer type.

A rigid wall was also created on the edge where the displacement is applied in order to force the nodes having the same offset. The rigid wall was created for both models and its reference points were created in the middle of the edge where the displacement is applied. In Figure 5.5 a) and b) it is shown the assembly of both models used for the simulations. It is possible to see where the reference points were created.

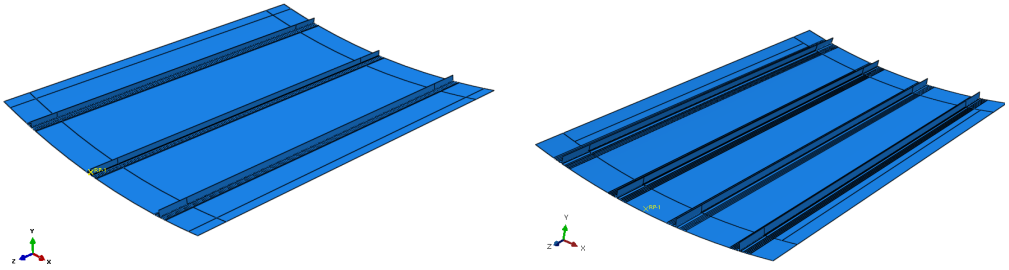

(a) Panel P10 (b) Panel P12

Figure 5.5: Assembly of the models.

5.3.2 Material Properties

Both models were built using composite materials, more specifically CFRP (carbon fiber reinforced plastics). They were made of the prepreg material IM7/8552 which is a epoxy resin. In detail, the skin of the panels was manufactured by manual tape laying in a mould and curing in an autoclave, the stringers were formed of prepreg tapes and cured, and then the stringers were bonded to the skin by application of s special adhesive film and curing. Then, each panel was inspected by ultrasonic, having not been found any substantial defect [55]. In this section the adhesive was not modeled since skin-stringer degradation was not taken into account. The material properties were measured with small specimens according to German standard and they are listed in table 5.3 [55].

Table 5.3: Material properties for CFRP prepreg $IM7/8552$ UD [55].

Longitudinal modulus of elasticity, E_{11}	146.535 GPa
Transverse modulus of elasticity, E_{22}	9.720 GPa
In-plane shear modulus, G_{12}	6.054 GPa
Poisson's ration, ν_{12}	0.34

The material was considered transverse isotropic which means its elastic constants are independent from the orientation of the axis in plane <23>. This means:

$$E_2 = E_3; \;\; \nu_{12} = \nu_{13}; \;\; G_{12} = G_{13}; \;\; G_{23} = \frac{E_2}{2(1+\nu_{23})}, \tag{5.1}$$

It is possible to introduce this type of material in Abaqus choosing the options *Mechanical -> Elastic* and then choosing *Lamina*. To define this type of material it is necessary to know the six constants, with four of them being listed in table 5.3. It is also known the value of G_{13} from the transverse isotropic definition and thus G_{23} is the only constant missing. It is possible to calculate this constant using equation 5.4 but firstly it is necessary to calculate ν_{23} using equation 5.3 [57]. This leads to

$$\nu_{21} = \frac{E_2}{E_1}\nu_{12} = 0.0226, \tag{5.2}$$

$$\nu_{23} = \nu_{12}\frac{(1-\nu_{21})}{(1-\nu_{12})} = 0.5035, \tag{5.3}$$

$$G_{23} = \frac{E_2}{2(1+\nu_{23})} = 3.232GPa. \tag{5.4}$$

5.3.3 Load and boundary conditions

The boundary conditions applied to both models can be seen in Figures 5.6 and 5.7. In Figure 5.6 it is shown the boundary condition applied to the whole panel while in Figure 5.7 it is shown in detail the boundary condition applied to the lateral edges.

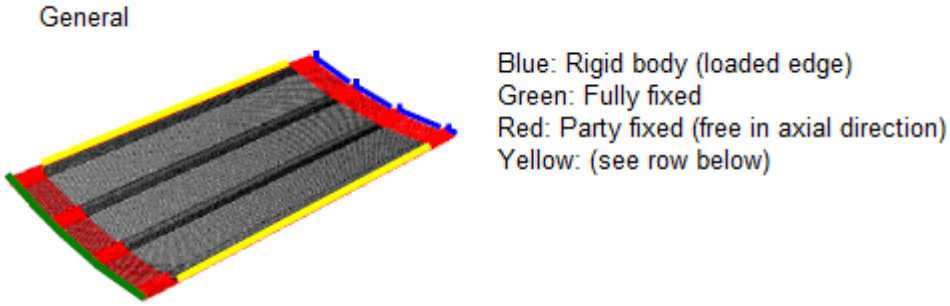

Figure 5.6: General boundary conditions [56].

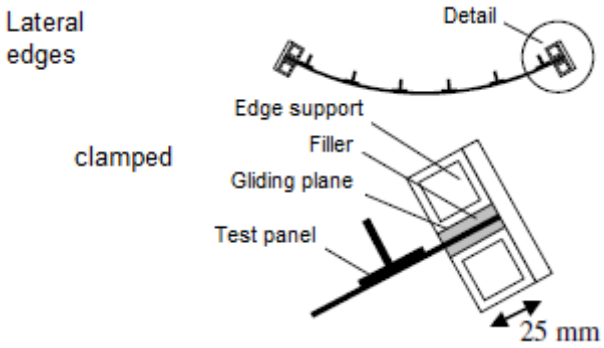

Figure 5.7: Boundary conditions of the lateral edges [56].

It should be mentioned that in the numerical model the lateral edges were not clamped. Instead, they were restrained only in the Ox displacement and in the Ox and Oz rotations. This boundary condition was based on article [55]. Later, it was changed for panel P12. The load was applied in the reference points of the rigid walls for both models, as a prescribed axial displacement with a value of 3 mm for panel P10 and with a value of 3.5 mm for panel P12.

5.4 Results

As it was mentioned before several parameters were tested in order to achieve a good agreement with the experimental results. Therefore, in this section it will be presented the results of the models P10 and P12, which includes the deformed shapes as also the load vs displacement curves. The results will be compared with the results shown in the article [55].

For panel P10 three different meshes were tested, in which the first one has 35862 elements, the second one has 20640 elements and the third one has 15072 elements, while for panel P12 five meshes were tested, in which the first one has 5076 elements, the second one has 9840 elements, the third one has 15939 elements, the fourth one has 28080 elements and the last one has 40448 elements. For both panels the S4R and S4 element formulations were tested, and for both panels four damping factors, using the constant damping factor approach, were used. The first thirty buckling modes were tested for both models as also 5 magnitude of imperfections.

5.4.1 Results of the panel P10

The results of the simulations of the panel P10 are presented hereafter. The next results were obtained from a model without imperfections and using S4R and S4 element formulations. The reason to not include the initial imperfections is because it was first made an analysis to discover which buckling mode each panel followed. Then, and being considered the deformed shapes of the models without imperfections, the buckling modes extracted from a previous eigenvalue analysis were tested and used as initial imperfections. In Figure 5.8 it is shown the deformed shapes of the three different meshes for a model with a constant damping factor of 2e-5 and S4R element formulation. In Figure 5.9 it is shown the load vs displacement curves of the respective three meshes. It can be seen that there is no big difference between the behaviour of the model with 35862 elements and the model with 20640 elements. The load vs displacement curves of these two models almost match with exception of the first global buckling area, which is slight smaller for the model with 20640 elements. Regarding the load vs displacement curve of the model with 15072 elements, it shows a similar behaviour comparatively to the other two models, however the first global buckling load is smaller and the postbuckling behaviour after the first global buckling area is below the load vs displacement curve of the experimental results. It is also shown that the prebuckling area of the three load vs displacement curves obtained in the present work do not match with the prebuckling area of the experimental result, although they are very close. Regarding the postbuckling area and specially the first global buckling load, it is possible to see that this choice of damping factor value is not the best option to represent the behaviour of the panel.

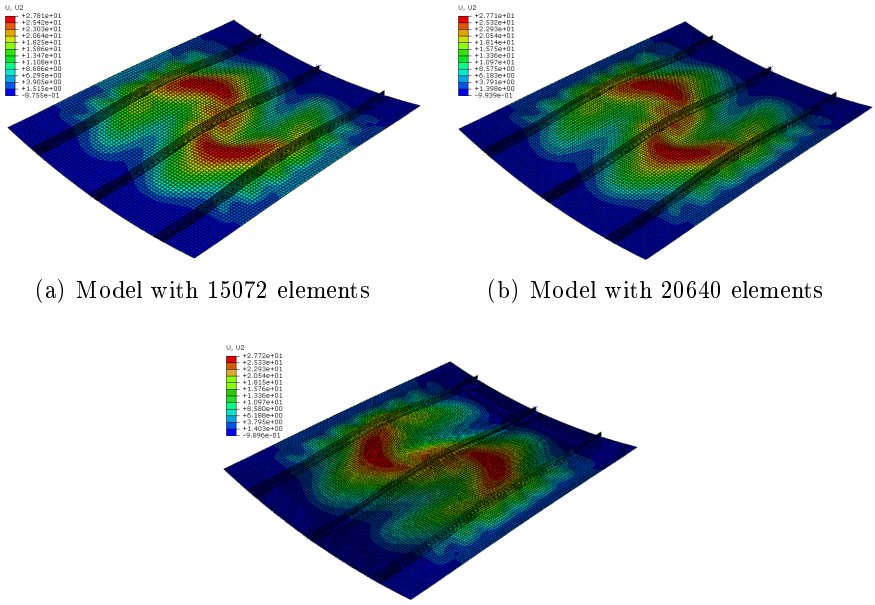

(a) Model with 15072 elements

(b) Model with 20640 elements

(c) Model with 35862 elements

Figure 5.8: Deformed shapes of the model with a damping factor of 2e-5 and S4R element type.

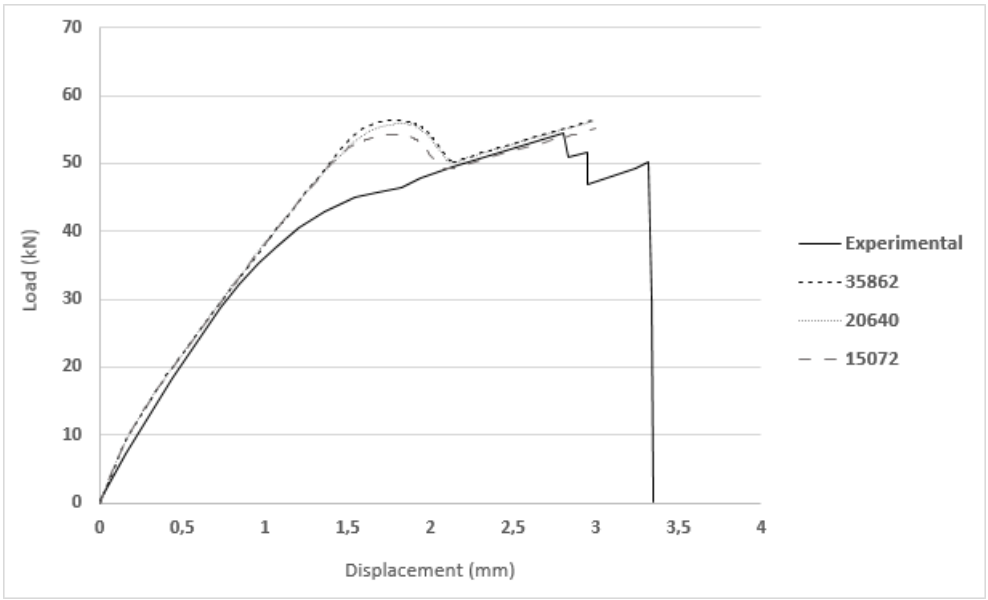

Figure 5.9: Load vs displacement curves of three different meshes, for damping factor equal to 2e-5, for a model without imperfections and with S4R element type.

The S4 element formulation it was also tested, as it was mentioned before, and in Figure 5.10 it is shown the deformed shapes obtained for that type of element. Comparing with the results obtained for the model using the S4R element formulation, it can be seen that the buckling shapes are very similar.

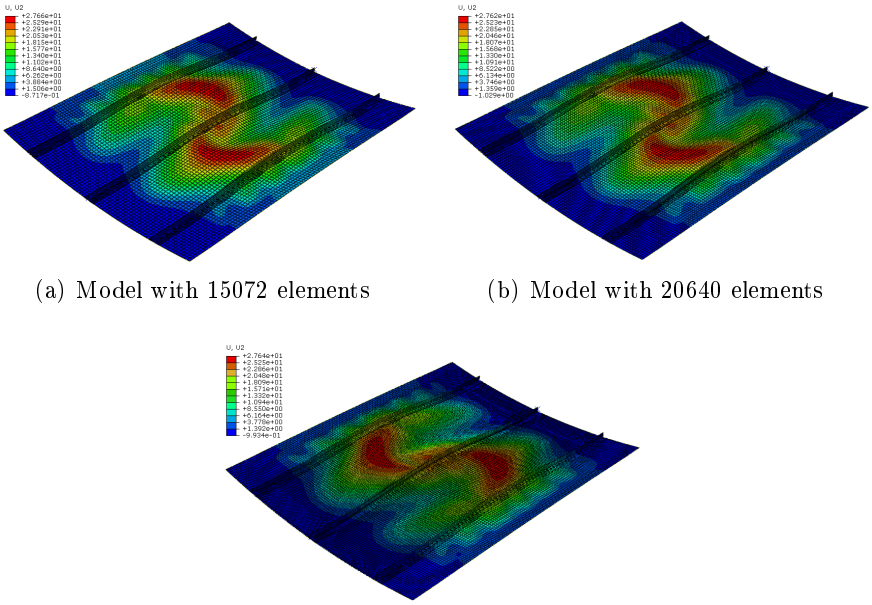

(a) Model with 15072 elements

(b) Model with 20640 elements

(c) Model with 35862 elements

Figure 5.10: Deformed shapes of the model with a damping factor of 2e-5 and S4 element type.

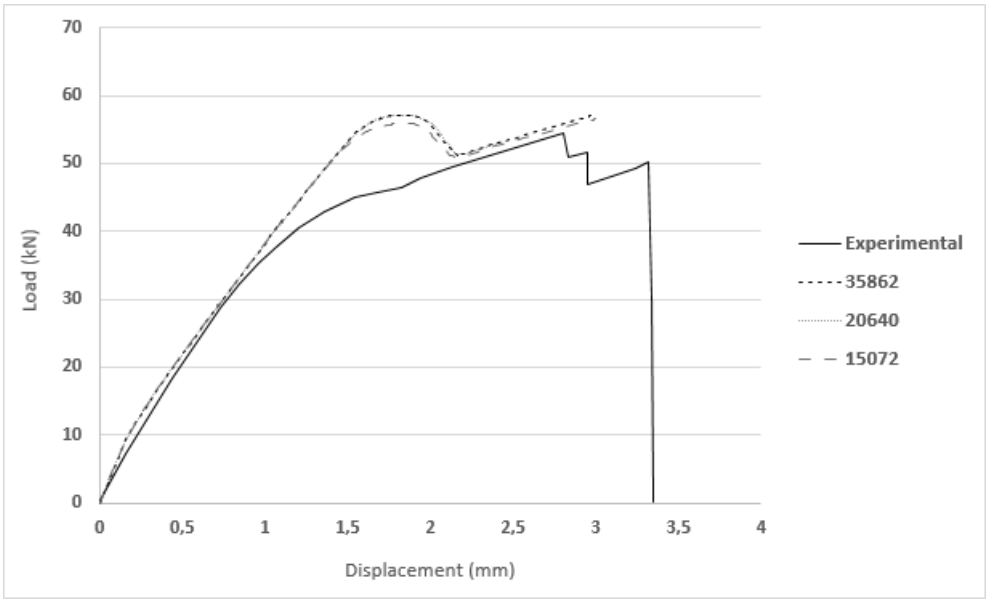

Figure 5.11: Load vs displacement curves of three different meshes, for damping factor equal to 2e-5, for a model without imperfections and with S4 element type.

Regarding the load vs displacement curves of the model with S4 element formulation, when comparing with the load vs displacement curves of the model with S4R element formulation, the behaviour is very similar however the first global buckling load is slight higher for the model with S4 element formulation. This can be seen in Figure 5.11.

The deformed shapes of the model with a damping factor of 2e-6 and S4R element formulation are shown in Figure 5.12. The deformed shapes of the first two meshes are very similar, while in the case of the model with 35862 elements it shows a different behaviour. The two first deformed shapes have a similar behaviour to the deformed shapes of the model with 35862 elements and damping factor of 2e-5, where it is visible the same buckling shape between the stringers. In the case of the model with 35862 elements, it is visible a global buckling between the left and middle stringers.

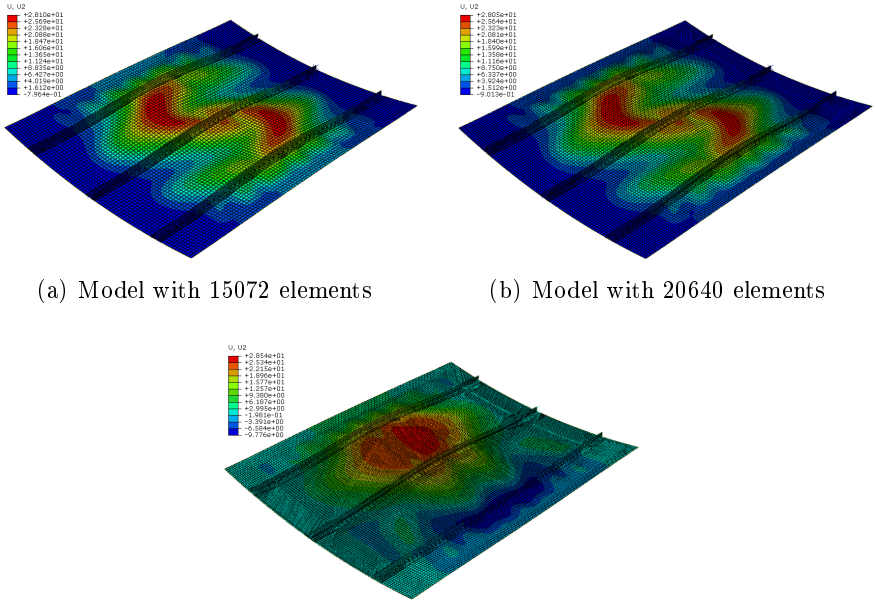

(a) Model with 15072 elements

(b) Model with 20640 elements

(c) Model with 35862 elements

Figure 5.12: Deformed shapes of the model with a damping factor of 2e-6 and S4R element type.

In Figure 5.13 it is shown the load vs displacement curves of the simulations with damping factor equal to 2e-6 and S4R element formulation. Comparing with the results shown for the model with damping factor of 2e-5, this model presents a different behaviour in the postbuckling area. The changing of the damping factor value from 2e-5 to 2e-6, is represented by a change in the first global buckling area, where it starts to form a peak. This effect is more visible for the model with 35862 elements and with the decreased of the damping factor this effect starts to appear in the other models with less elements.

The deformed shapes of the model with damping factor of 2e-6 and S4 element formulation is shown in Figure 5.14. This is an exceptional case where the model with 15072 and 35862 element have a similar behaviour, however it can be seen that the global buckling appear in opposite sides of the panel. For the model with 15072 elements the global buckling appears between the middle and right stringer, while in the case of the model with 35862 elements the global buckling appears between the left and middle stringer.

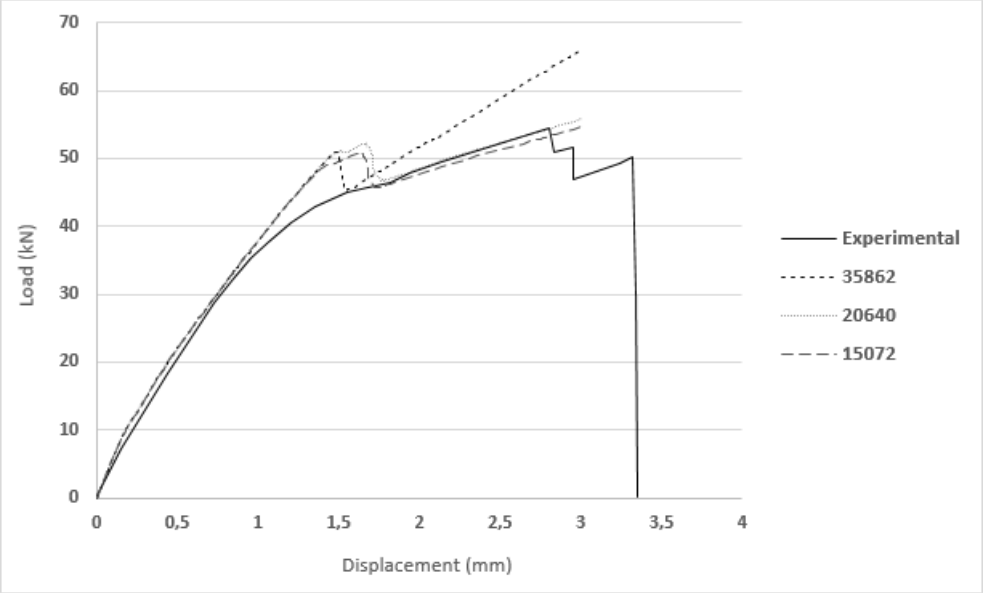

Figure 5.13: Load vs displacement curves of three different meshes, for damping factor equal to 2e-6, for a model without imperfections and with S4R element type.

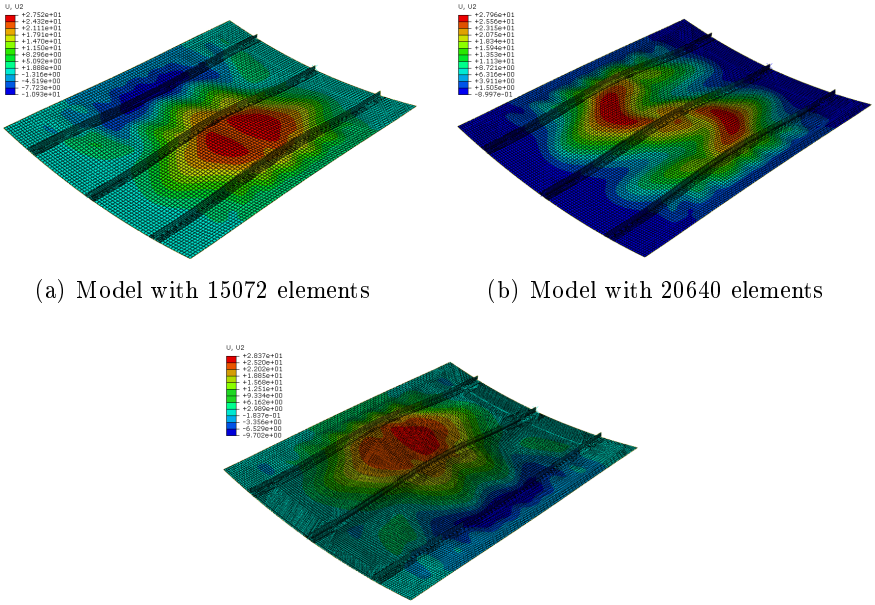

(a) Model with 15072 elements

(b) Model with 20640 elements

(c) Model with 35862 elements

Figure 5.14: Deformed shapes of the model with a damping factor of 2e-6 and S4 element type.

In Figure 5.15 it is shown the load vs displacement curves of the respective models. In this case it can be seen that the first global buckling load is smaller than the first global buckling load of the model with S4R element formulation (for the models with 35862 and 15072 elements).

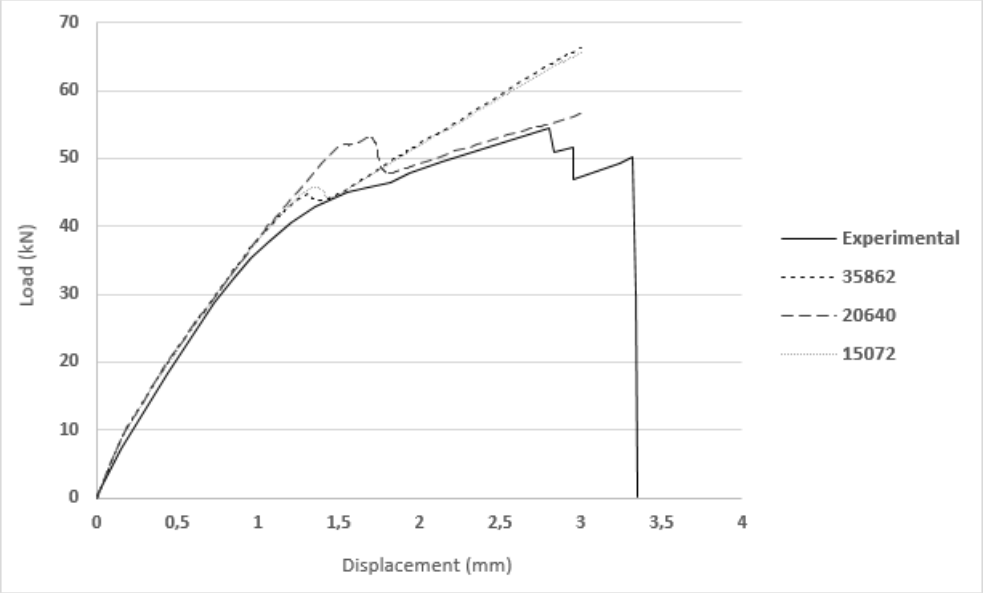

Figure 5.15: Load vs displacement curves of three different meshes, for damping factor equal to 2e-6, for a model without imperfections and with S4 element type.

The deformed shapes of the model with a damping factor of 2e-7 and S4R element formulation is shown in Figure 5.16.

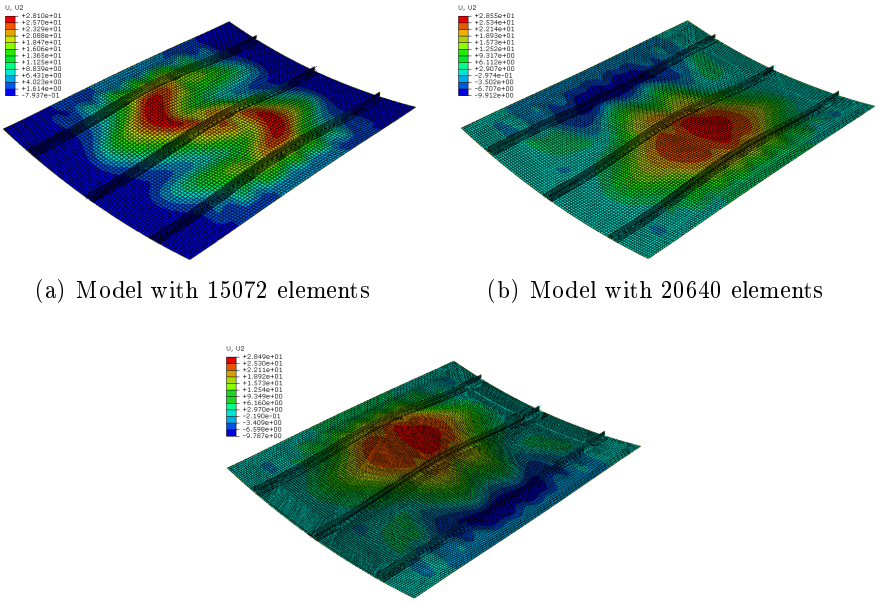

(a) Model with 15072 elements

(b) Model with 20640 elements

(c) Model with 35862 elements

Figure 5.16: Deformed shapes of the model with a damping factor of 2e-7 and S4R element type.

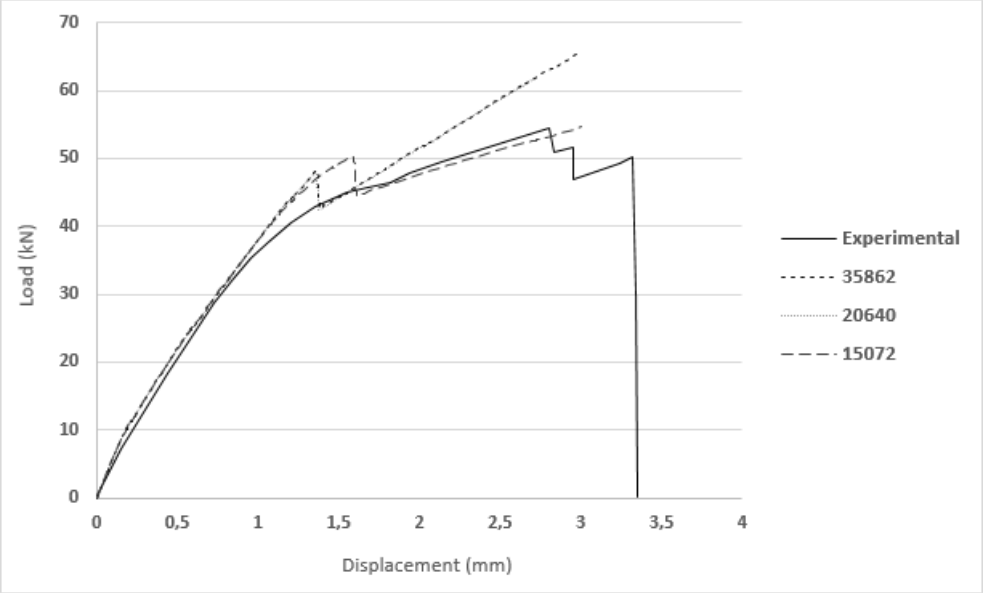

Figure 5.17: Load vs displacement curves of three different meshes, for damping factor equal to 2e-7, for a model without imperfections and with S4R element type.

It can be seen (Figure 5.16) that the deformed shapes of the model with 20640 elements becomes similar to the deformed shape of the model with 35862 elements, despite the buckling shapes being in opposite sides. The load vs displacement curves of the model with a damping factor of 2e-7 and S4R element formulation is shown in Figure 5.17. It can be seen that the curves of the models with 20640 and 35862 elements match while the curve of the model with 15072 elements have an higher first global buckling load and a different behaviour after that point. Regarding the model with S4 element formulation and comparing to the model with S4R element formulation, they have similar behaviours and the first global buckling load is higher for the model with S4 element formulation. This is shown in Figures 5.18 and 5.19.

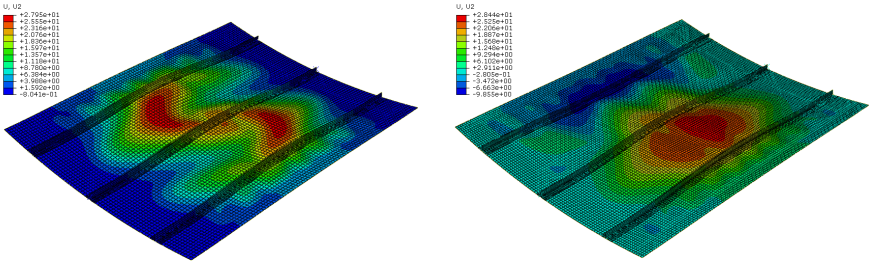

(a) Result of the model with 15072 elements

(b) Results of the models with 20640 and 35862 elements

Figure 5.18: Deformed shapes of the model with a damping factor of 2e-7 and S4 element type.

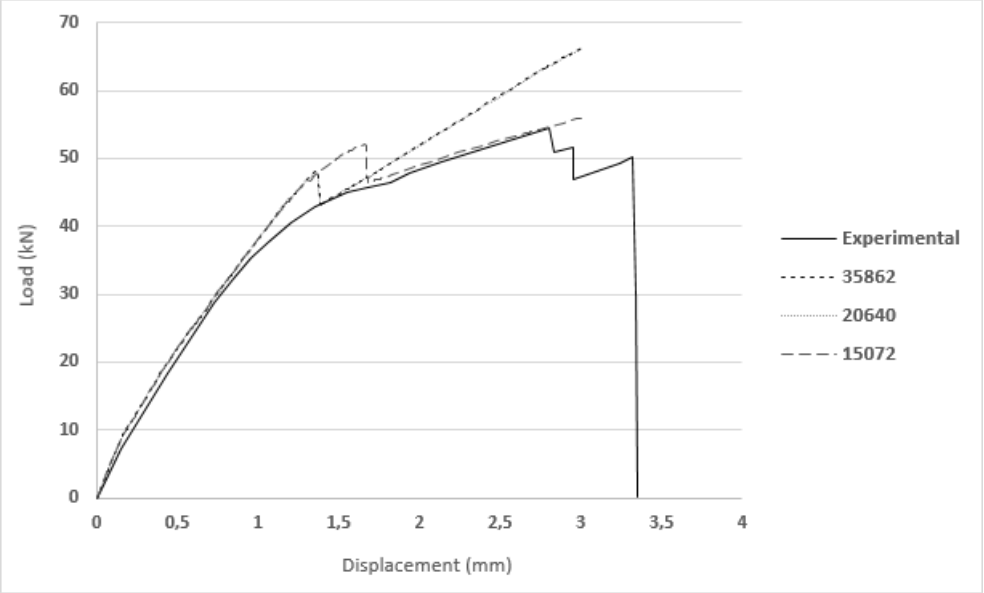

Figure 5.19: Load vs displacement curves of three different meshes, for damping factor equal to 2e-7, for a model without imperfections and with S4 element type.

The results of the model with a damping factor of 2e-8 and S4R and S4 element formulation are shown in Figures 5.20, 5.21, 5.22 and 5.23. It can be seen that there is no big difference between the models with a damping factor of 2e-7 and 2e-8.

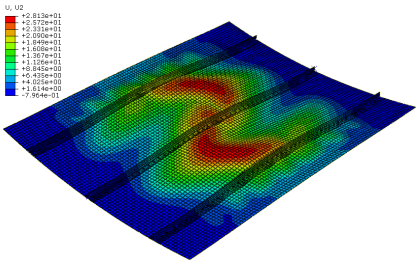

(a) Model with 15072 elements

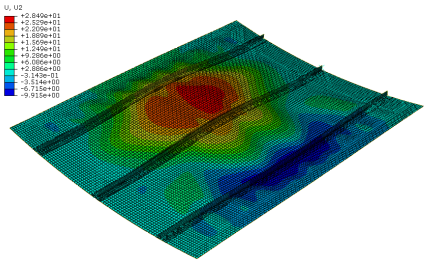

(b) Model with 20640 elements

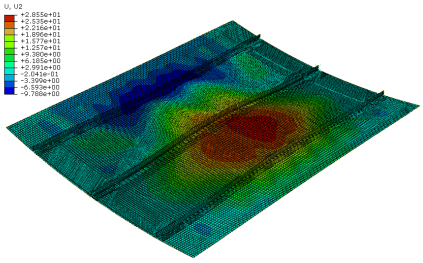

(c) Model with 35862 elements

Figure 5.20: Deformed shapes of the model with a damping factor of 2e-8 and S4R element type.

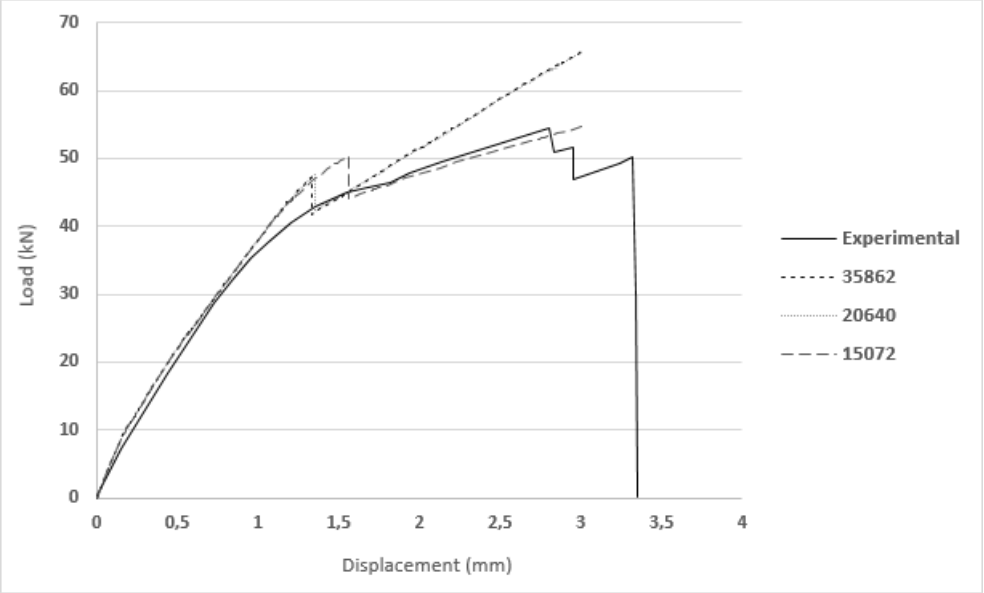

Figure 5.21: Load vs displacement curves of three different meshes, for damping factor equal to 2e-8, for a model without imperfections and with S4R element type.

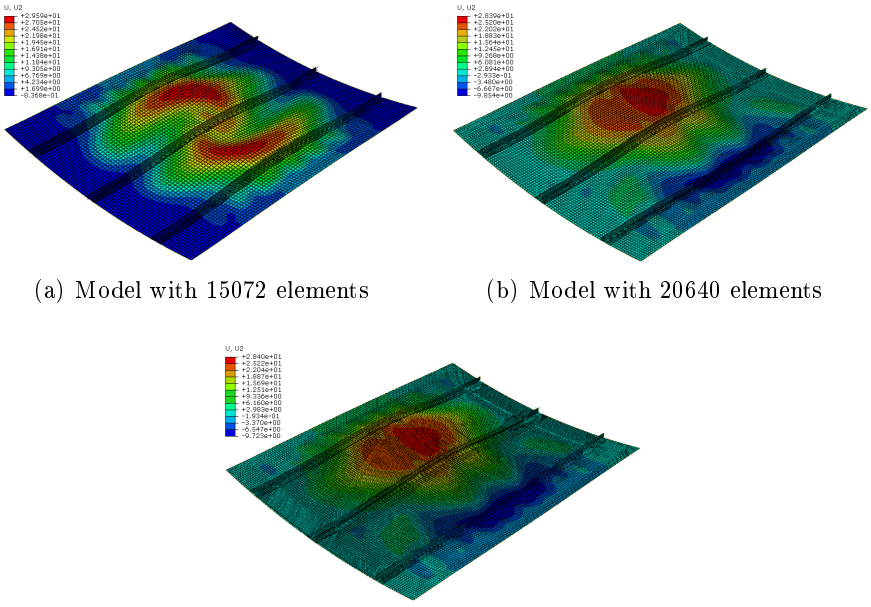

(a) Model with 15072 elements

(b) Model with 20640 elements

(c) Model with 35862 elements

Figure 5.22: Deformed shapes of the model with a damping factor of 2e-8 and S4 element type.

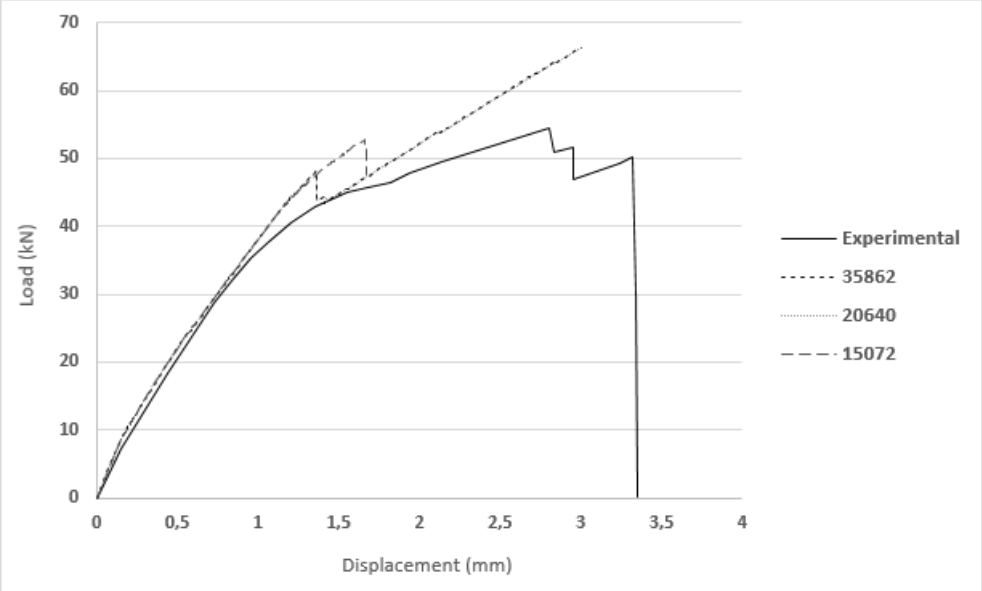

Figure 5.23: Load vs displacement curves of three different meshes, for damping factor equal to 2e-8, for a model without imperfections and with S4 element type.

After being analysed all the models without imperfections, the buckling modes were tested for the model with 35862 elements, S4R element formulation and a damping factor of 2e-6. This model was chosen because the load vs displacement curves of the other models with a damping factor of 2e-7 and 2e-8 showed a postbuckling behaviour, after the first global buckling area, below the load vs displacement curve of the experimental result. Other factors were taken into account. For instance the first global buckling load, which is higher comparatively with the models with a damping factor of 2e-7 and 2e-8, however these two last models take too much computational time and especially the models with S4 element formulation. In Figure 5.24 it is shown the mode shape used as imperfection. This mode corresponds to the twenty-fifth eigenvalue and it has a critical load of 13.6 kN.

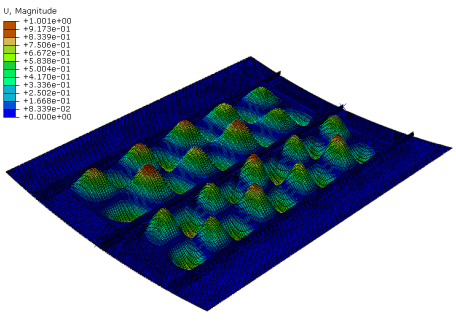

Figure 5.24: Mode shape used as imperfection.

In Figure 5.25 it is shown the deformed shapes of a model with positive imperfections. It was tested five different magnitudes of imperfections and it can be seen that the panel presents a global buckling which appears in the left side of the panel for the lowest and

the two higher magnitude of imperfection. For a magnitude of imperfection of 25 and 50 % the global buckling appears in the right side of the panel.

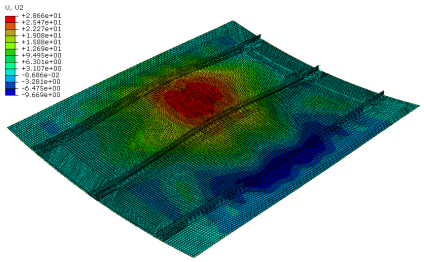

(a) Result of the model with an imperfection of 10%

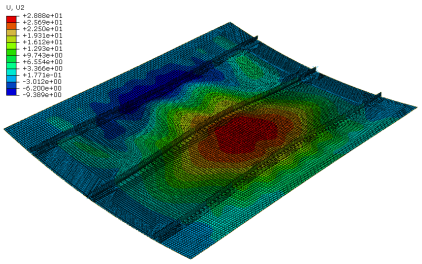

(b) Result of the model with an imperfection of 25%

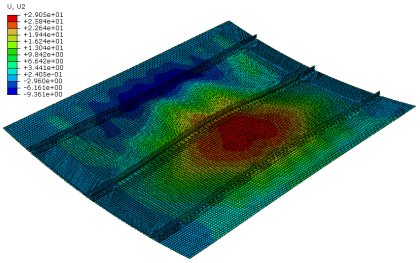

(c) Result of the model with an imperfection of 50%

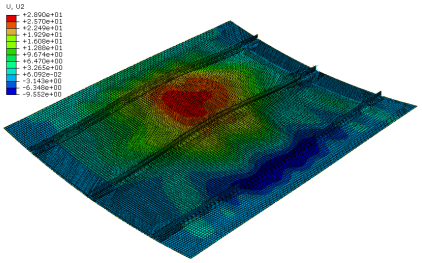

(d) Result of the model with an imperfection of 75%

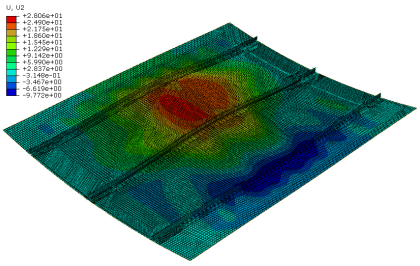

(e) Result of the model with an imperfection of 95%

Figure 5.25: Deformed shapes of the model with positive imperfections.

The deformed shapes of a model with negative magnitude of imperfections can be seen in Figure 5.26. In this case the panel presents a global buckling shape in the left side of the panel for the two lowest magnitude of imperfections and from the magnitude of imperfection of 50% the buckling shape shifted to the right side of the panel until the magnitude of imperfection of 95 %.

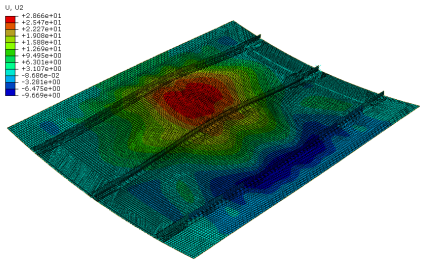

(a) Result of the model with an imperfection of 10%

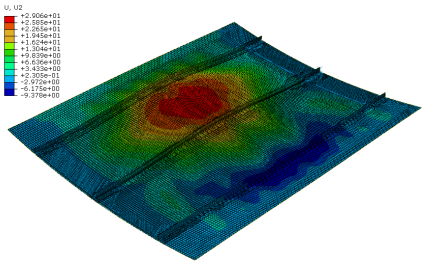

(b) Result of the model with an imperfection of 25%

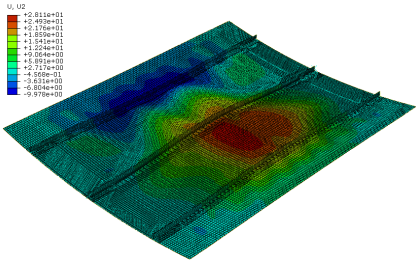

(c) Result of the model with an imperfection of 50%

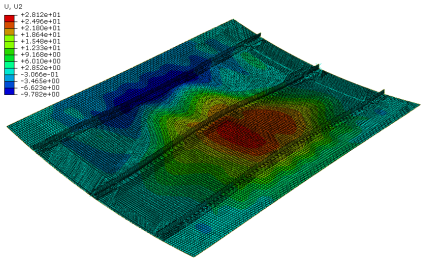

(d) Result of the model with an imperfection of 75%

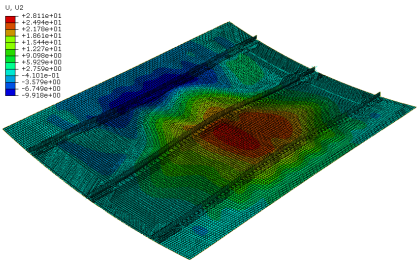

(e) Result of the model with an imperfection of 95%

Figure 5.26: Deformed shapes of the model with negative imperfection.

The load vs displacement curves of the model with positive imperfections are shown in Figure 5.27. It can be seen that with the increase of the magnitude of imperfections, the curves shifted to the right being more close to the experimental curve. It also can be seen that the first global buckling load decreases and increases with the increase of the magnitude of imperfections. In other words, when it changes from a magnitude of imperfection of 10 % to 25 %, the buckling load decreases but when it changes from a magnitude of 25 to 50 % the buckling load increases again, and so on ultil a magnitude of imperfection of 96 %. In Figure 5.28 it is shown the load vs displacement curve of the model with negative magnitude of imperfections. In this case the buckling load increases with the increase of the magnitude of imperfections and as it happened with the models with positive magnitude of imperfections, the curves shifted to the right side of the graph being more close to the experimental curve. Comparatively to the models with positive imperfections, the models with negative imperfections present lower buckling loads.

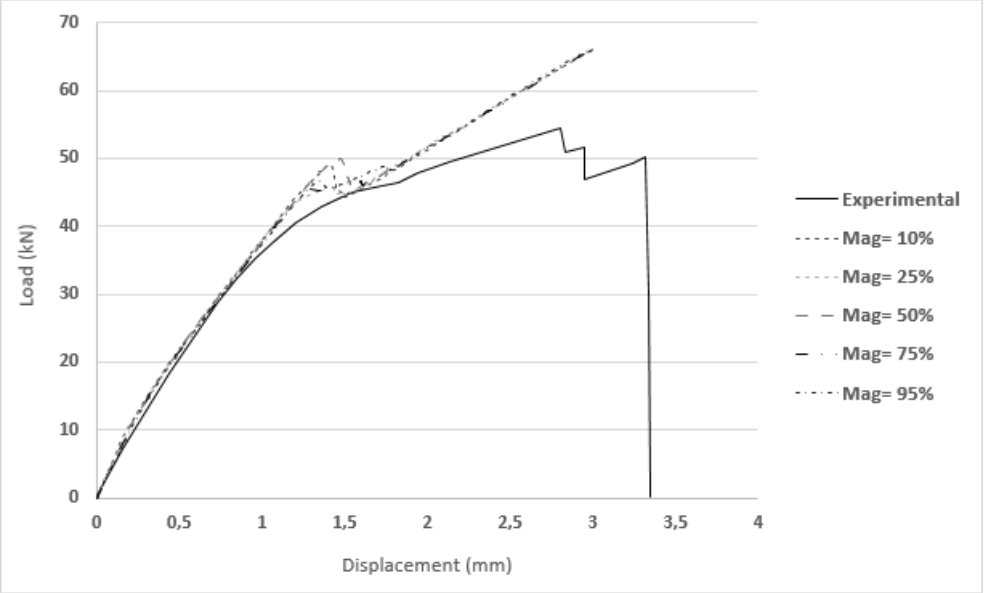

Figure 5.27: Results of the positive magnitude of imperfections.

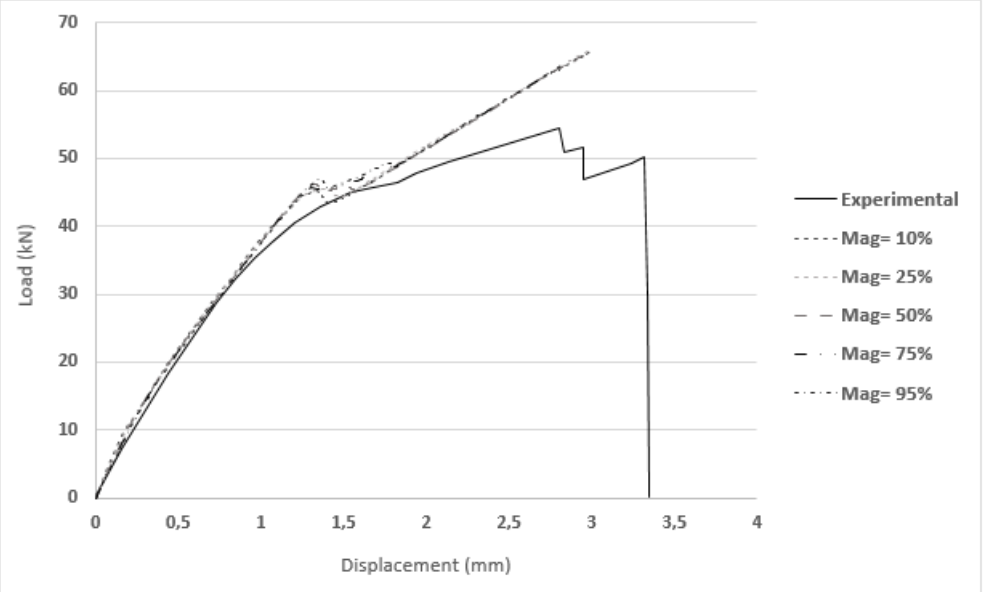

Figure 5.28: Result of the negative magnitude of imperfection.

5.4.2 Results of the panel P12

The results of the panel P12 will be shown hereafter. Firstly it will be shown the results of the five different meshes and four damping factors (constant damping factor approach). This first simulations were based on a model without initial imperfections for the same reason mentioned for the panel P10 . For each damping factor value it will also be presented the results for two different type of elements (S4R and S4 element formulations). In Figure 5.29 it is shown the deformed shapes for five different meshes

and damping factor equal to 2e-5. It is visible that the models with 28080 and 15939 present a similar behaviour as well as the models with 9840 and 5076 elements. They are all characterized by a global buckling in the center of the panel, but having different shapes.

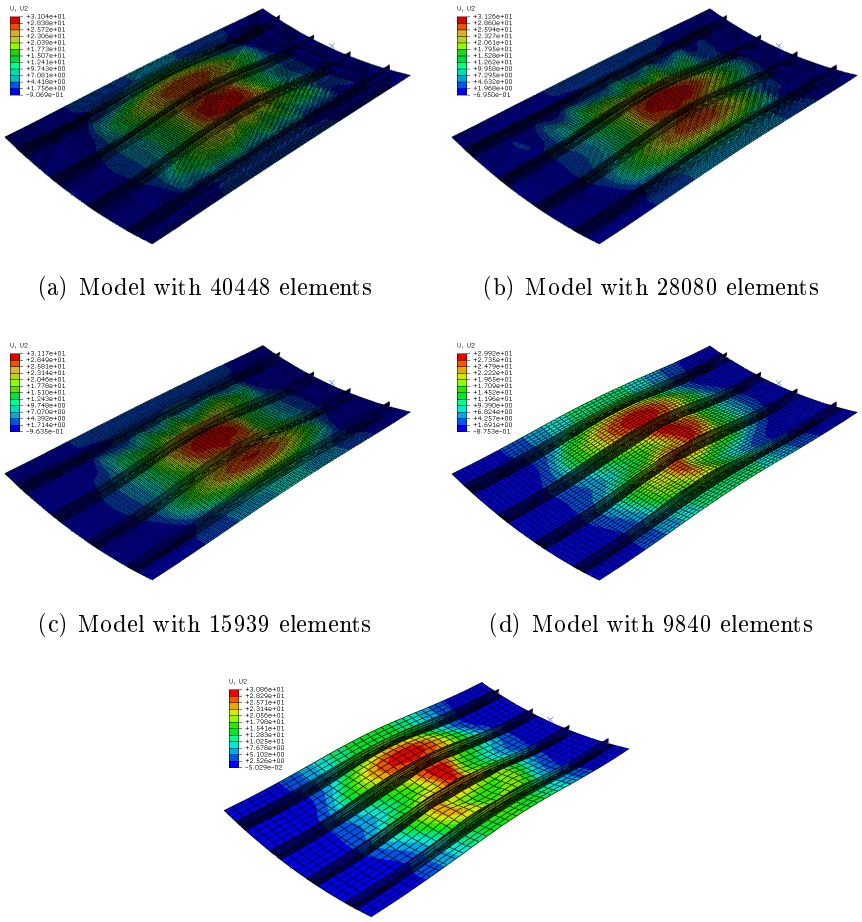

(a) Model with 40448 elements

(b) Model with 28080 elements

(c) Model with 15939 elements

(d) Model with 9840 elements

(e) Model with 5076 elements

Figure 5.29: Deformed shapes of the model with a damping factor of 2e-5.

In Figure 5.30 it is shown the load vs displacement curves for five meshes of a model with S4R element formulation and damping factor equal to 2e-5. It can be seen that there is a good agreement between the experimental and computational results for the prebuckling area. However, it is visible that the postbuckling area does not even partly match. Comparing the models with 15939 and 28080 elements, the behaviour is very similar however the first global buckling load is higher for the model with 28080 elements . The model with 40448 elements, exhibits a different behaviour comparatively with the other four models and in general, it is possible to see that the first global buckling load increases with the increasing number of elements. Resuming, for this damping factor value, there is not a good agreement between the computational and experimental results for the postbuckling area, for any of the five meshes, as in terms of behaviour as in terms of critical load.

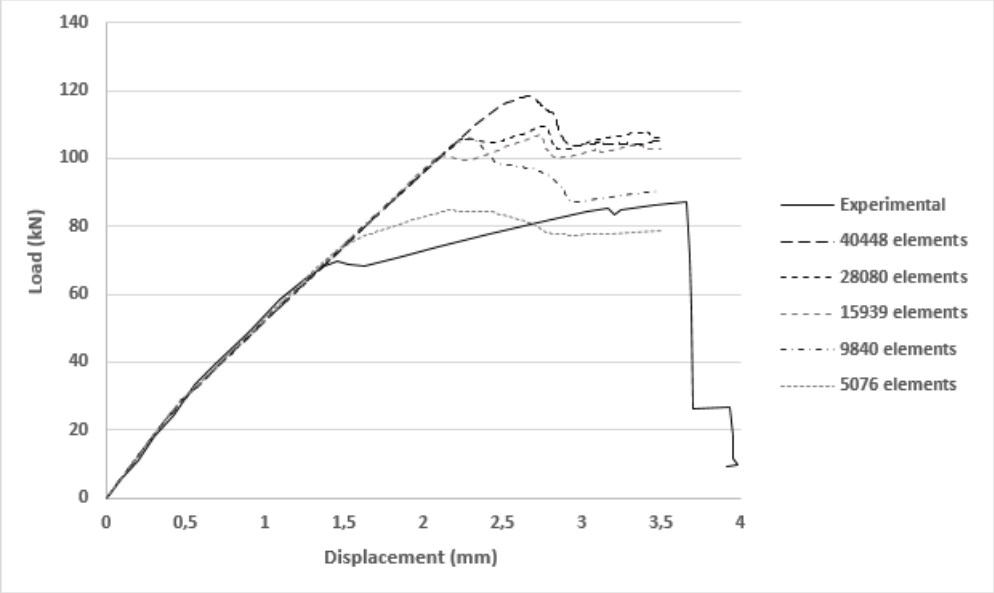

Figure 5.30: Load vs displacement curves of five different meshes, for damping factor equal to 2e-5, for a model without imperfections and with S4R element type.

In Figure 5.31 it is shown the load vs displacement curves for the same model but for the S4 element formulation. Comparing with the load vs displacement curves of the model with S4R element formulation, in general, the behaviour is similar. The difference between the two type of elements resides in the first global buckling load which is higher for the S4 element formulation (with exception of the model with 9840 elements).

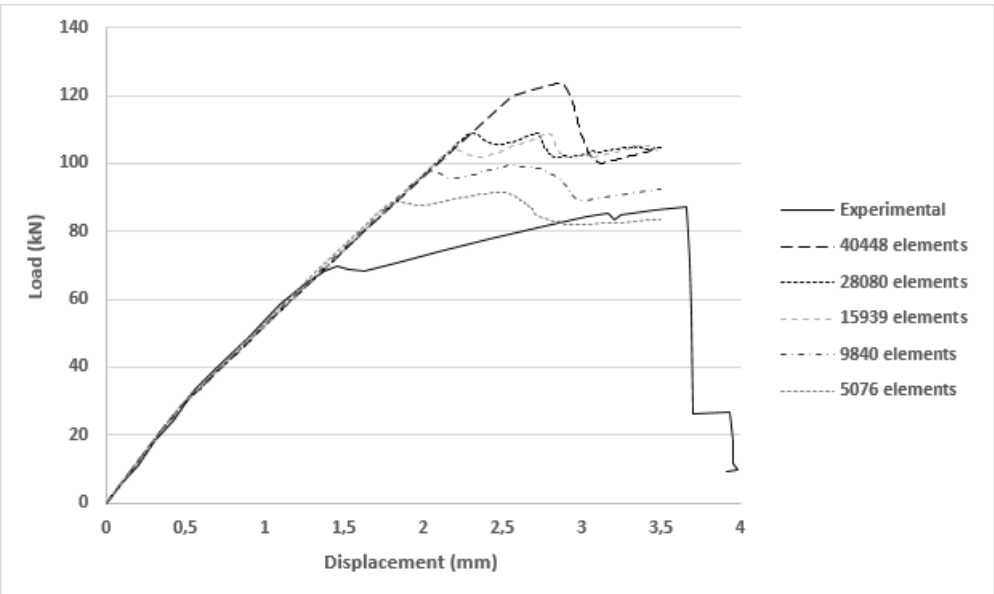

Figure 5.31: Comparison between five different meshes for damping factor equal to 2e-5, for a model without imperfections and with S4 element type.

The deformed shapes for the five different meshes, using the S4R element formulation and with a damping factor equal to 2e-6 can be seen in Figure 5.32. It can be seen that there are some changes in the buckling shapes when it changes the damping factor value from 2e-5 to 2e-6.

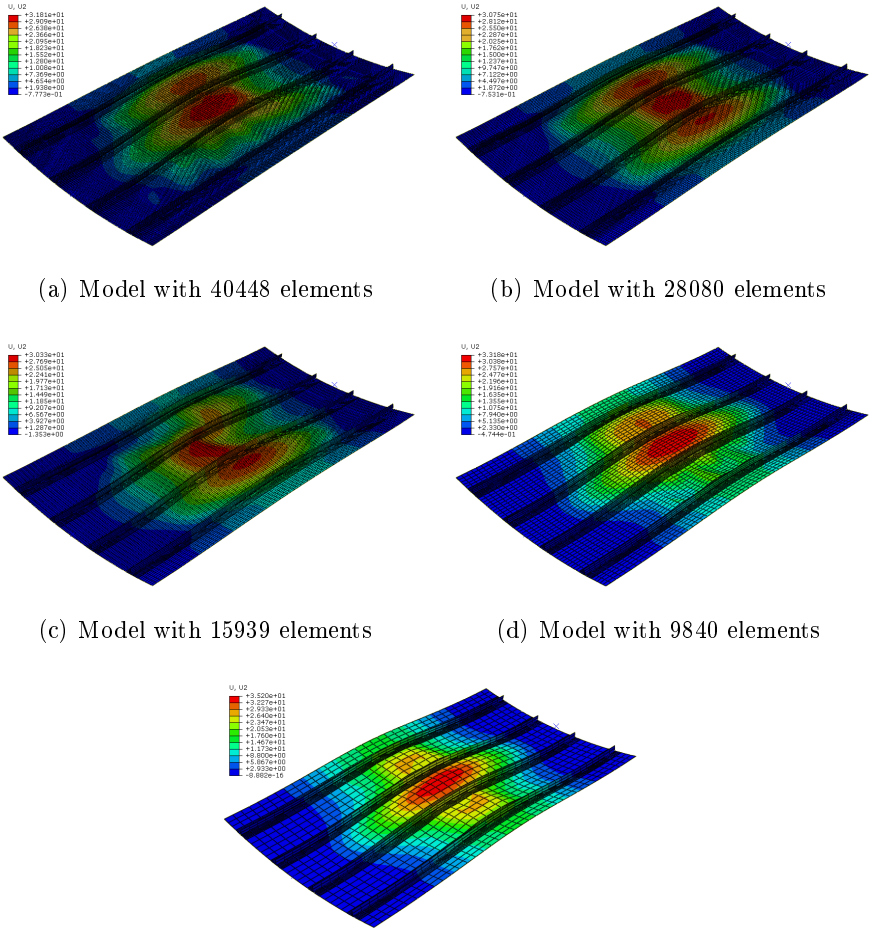

(a) Model with 40448 elements

(b) Model with 28080 elements

(c) Model with 15939 elements

(d) Model with 9840 elements

(e) Model with 5076 elements

Figure 5.32: Deformed shapes of the model with a damping factor of 2e-6.

Comparing with the model with a damping factor of 2e-5, the model with a damping factor of 2e-6 exhibits a different behaviour which is possible to see in Figure 5.33. The curves of this model start to present a peak in the first global buckling load area while in the case of the model with a damping factor of 2e-5 shows a horizontal behaviour, as it happened with panel P10. Once again the prebuckling area shows a good agreement with the experimental model, however the first global buckling load continues too high.

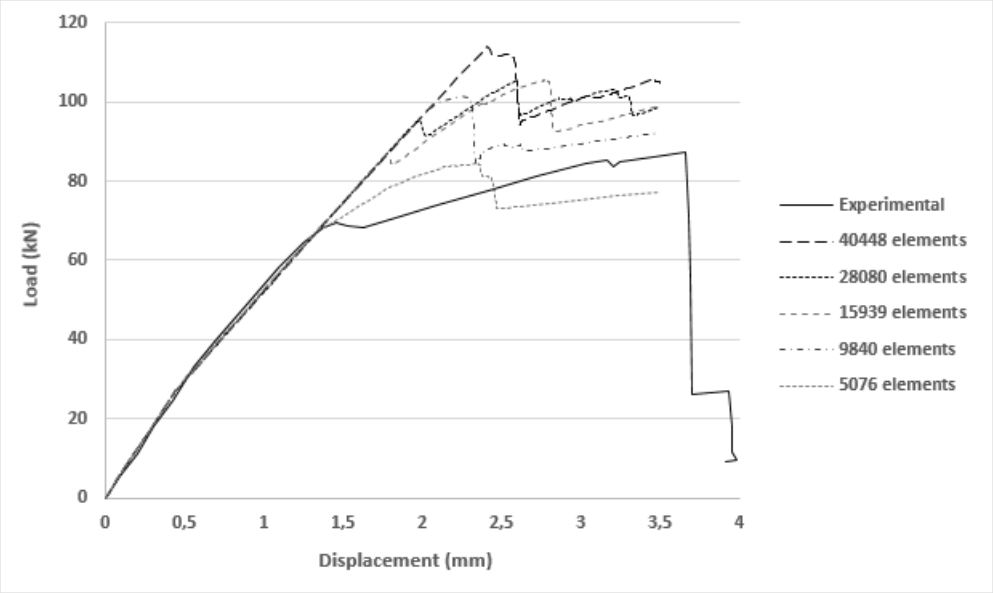

Figure 5.33: Comparison between five different meshes for damping factor equal to 2e-6, for a model without imperfections and with S4R element type.

In Figure 5.34 it is shown the results for the same models but with S4 element formulation. The biggest difference between the two element formulations resides in the model with 40448 which has a completely different postbuckling behaviour, besides the first global buckling load which is much higher for the model with S4 element formulation.

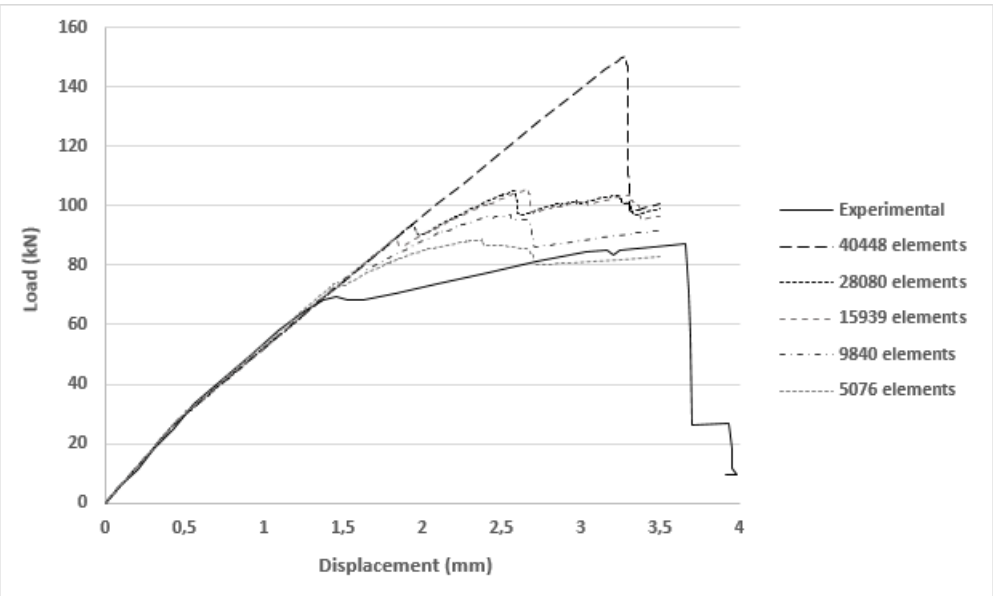

Figure 5.34: Comparison between five different meshes for damping factor equal to 2e-6, for a model without imperfections and with S4 element type.

In Figure 5.35 it is shown the deformed shapes of the models with a damping factor of 2e-7. For this value of damping factor it can be seen that the model with 40448 elements

presents a different behaviour from all the others. While the other models present a global buckling in the center of the panel, the model with 40448 elements presents local buckles between the stringers.

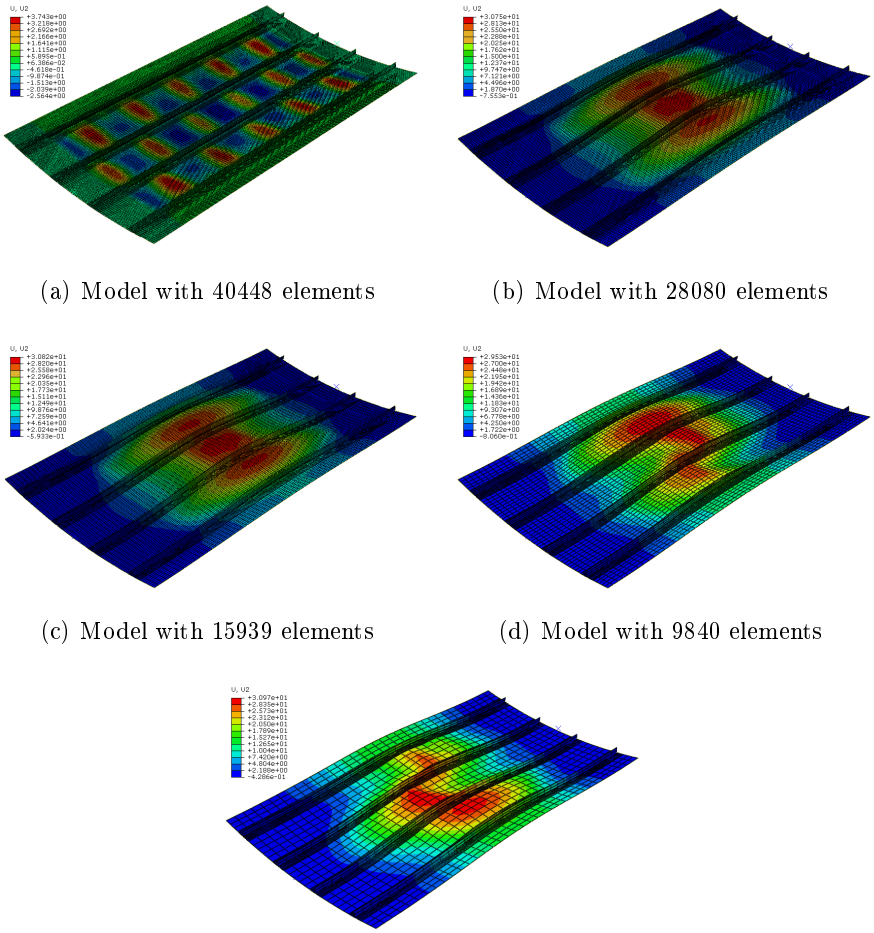

(a) Model with 40448 elements

(b) Model with 28080 elements

(c) Model with 15939 elements

(d) Model with 9840 elements

(e) Model with 5076 elements

Figure 5.35: Deformed shapes of the model with a damping factor of 2e-7.

In Figure 5.36 it is shown the load vs displacement curves for the five different meshes and a damping factor of 2e-7. The particularity of this damping factor value is the model with 40448 elements which presents a completely different behaviour from the other models. This was expected since the deformed shaped of this model presented local buckles between the stringers instead of a global buckle in the center of the panel.

The load vs displacement curves of the same model but with the S4 element formulation can be seen in Figure 5.37. In this case the load vs displacement curve of the model with 40448 elements presents a similar behaviour to the load vs displacement curve of the model with a damping factor of 2e-6 and S4 element formulation.

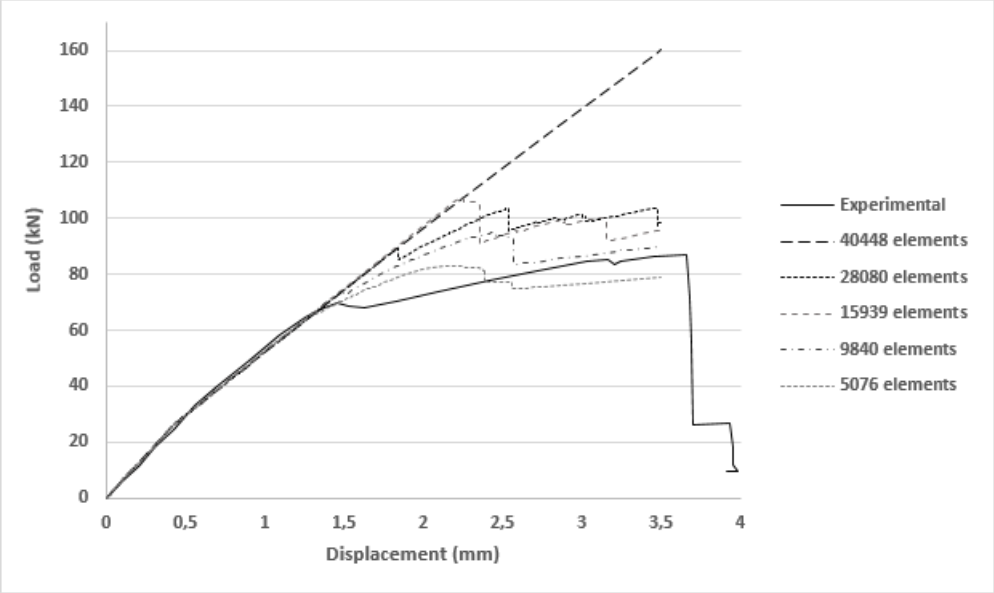

Figure 5.36: Comparison between five different meshes for damping factor equal to 2e-7, for a model without imperfections and with S4R element type.

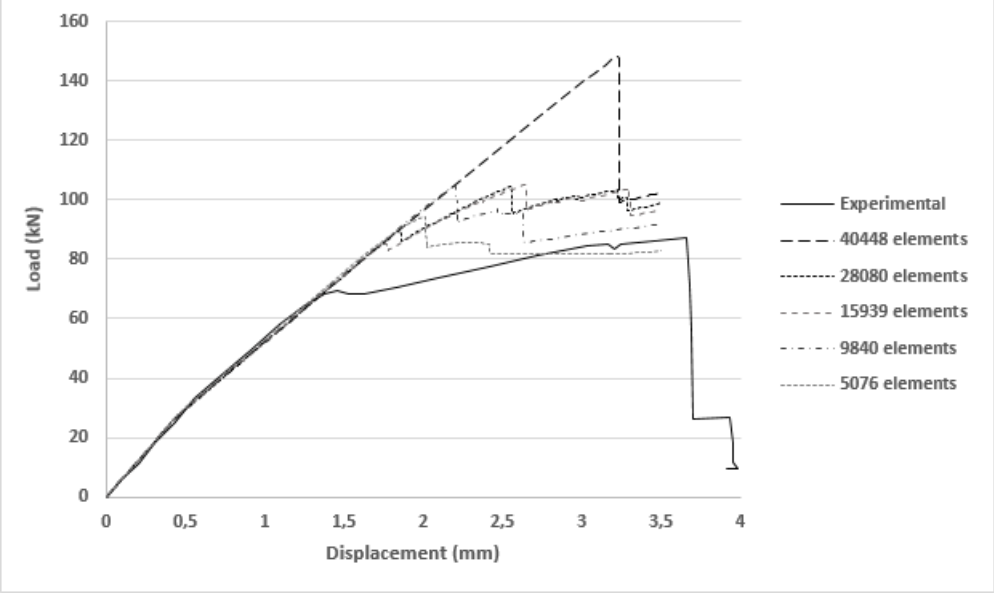

Figure 5.37: Comparison between five different meshes for damping factor equal to 2e-7, for a model without imperfections and with S4 element type.

The deformed shapes of the model with a damping factor of 2e-8 and S4R element formulation is shown in Figure 5.38. The load vs displacement curves of this model is shown in Figure 5.39.

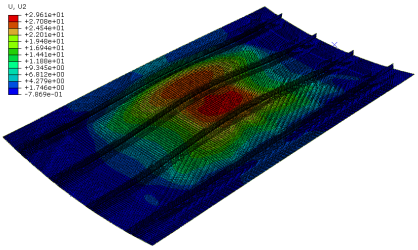

(a) Model with 40448 elements

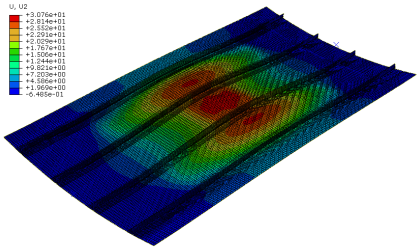

(b) Model with 28080 elements

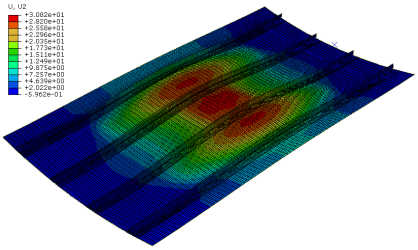

(c) Model with 15939 elements

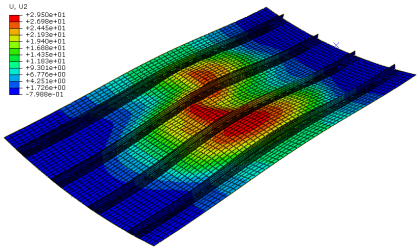

(d) Model with 9840 elements

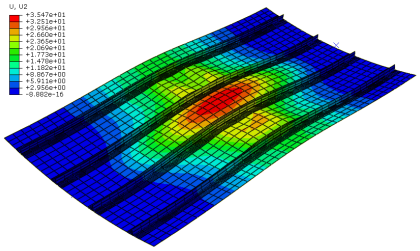

(e) Model with 5076 elements

Figure 5.38: Deformed shapes of the model with a damping factor of 2e-8.

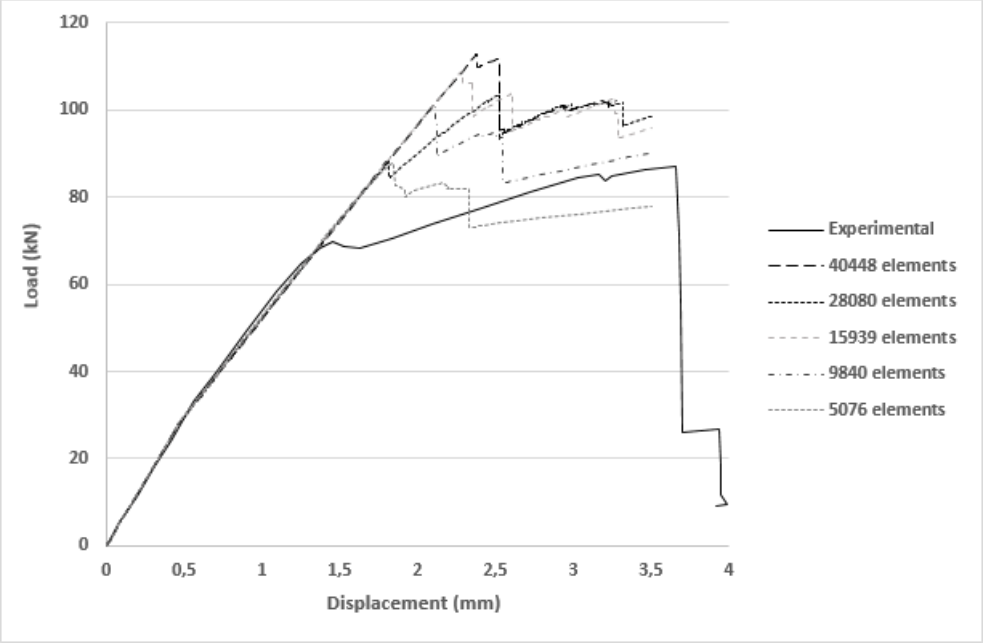

Figure 5.39: Comparison between five different meshes for damping factor equal to 2e-8, for a model without imperfections and with S4R element type.

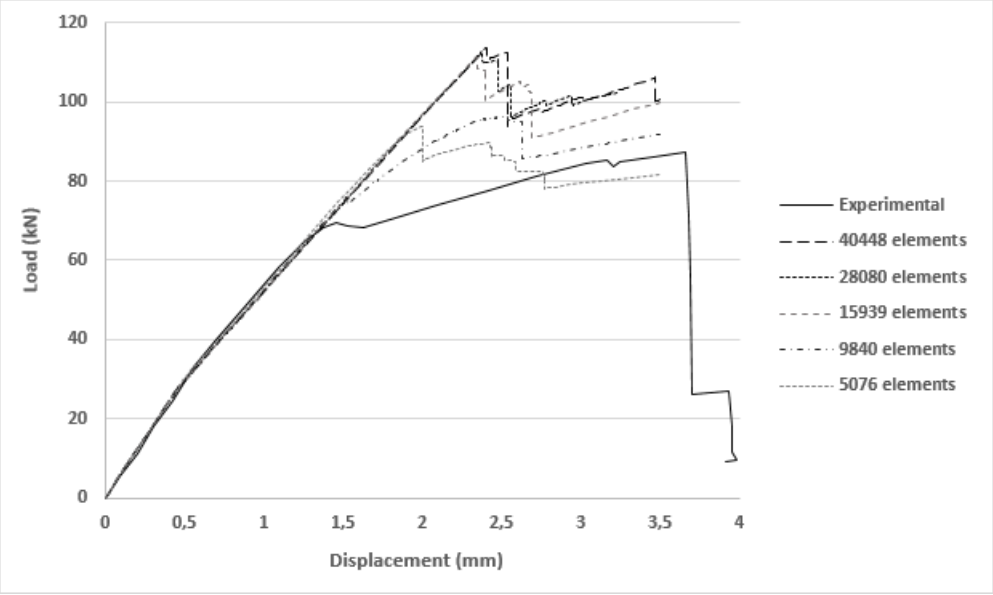

Figure 5.40: Comparison between five different meshes for damping factor equal to 2e-8, for a model without imperfections and with S4 element type.

A summary of the first global buckling loads of all models is given in Table 5.4. It can be seen that the first global buckling loads of all models are too high when compared with the reference value. One cause to this problem could be the boundary conditions applied to the longitudinal edges. This will be shown later.

Table 5.4: Comparison between the first global buckling loads of the five meshes and four damping factors.

Meshes	First global buckling load (kN)							
	2e-5		2e-6		2e-7		2e-8	
	S4R	S4	S4R	S4	S4R	S4	S4R	S4
40448	118.2	123.7	112.1	150.1	-	148.3	112.6	113.7
28080	105.9	108.9	95.4	93.5	89.2	89.9	88.4	112.6
15939	100.7	104.2	86.5	88.9	107.8	86.1	108.8	111.3
9840	105.7	97.6	101.4	79.3	74.3	104.7	101	76
5076	84.8	88.8	84.5	74.1	83	94	87.7	93.9
Ref.	69.6							

After being analysed all the models without imperfections, the buckling modes were tested for the model with 15939 elements, S4R element formulation and a damping factor of 2e-6. This model was chosen because it is the model that has the lowest first global buckling load and the behaviour more proximate to the experimental curve. The computational time was also other factor being considered in the choice of the model.

In Figure 5.41 it is shown the mode shape used as imperfection. This mode shape corresponds to the twenty-second eigenvalue and has a critical load of 29.6 kN. The deformed shapes for the models with positive imperfections are shown in Figure 5.42. With exception of the model with the lowest magnitude of imperfection, the other four models present the same buckling shape, which some of the buckles are deeper than others. In Figure 5.43 it is shown the deformed shapes of the models with negative magnitude of imperfections. In this case the last three models presents a similar buckling shape in the center of the panels.

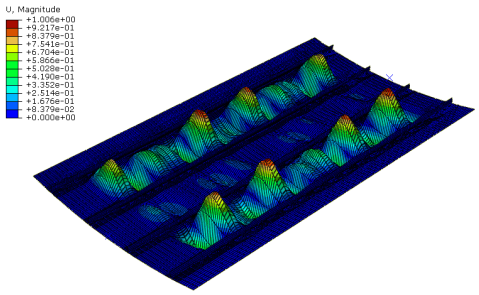

Figure 5.41: Mode shape used as imperfection.

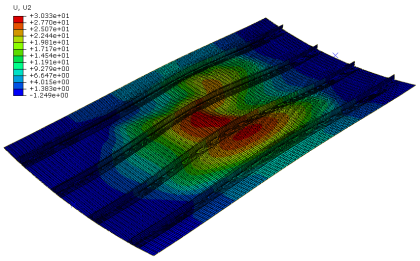

(a) Result of the model with an imperfection of 10%

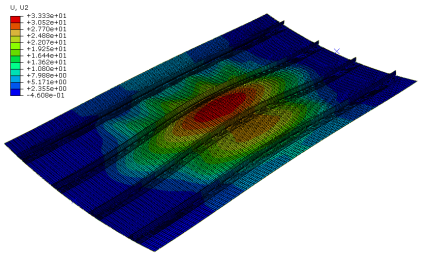

(b) Result of the model with an imperfection of 25%

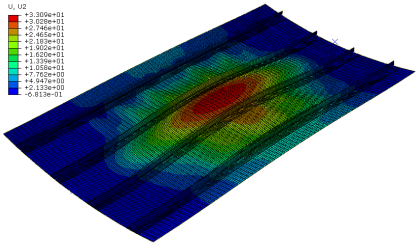

(c) Result of the model with an imperfection of 50%

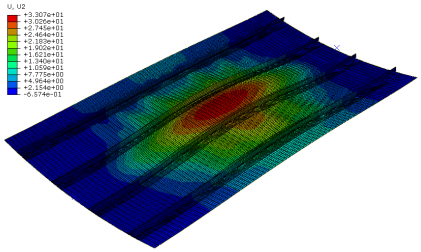

(d) Result of the model with an imperfection of 75%

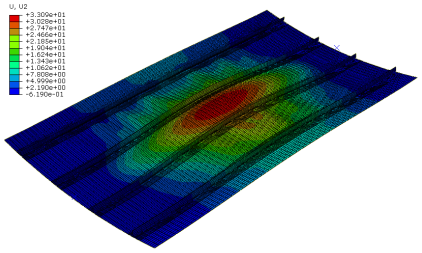

(e) Result of the model with an imperfection of 95%

Figure 5.42: Deformed shapes of the model with imperfection.

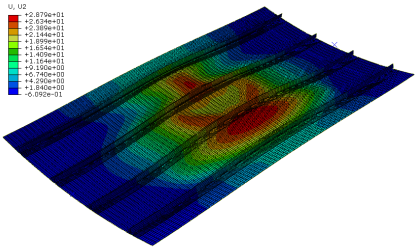

(a) Result of the model with an imperfection of 10%

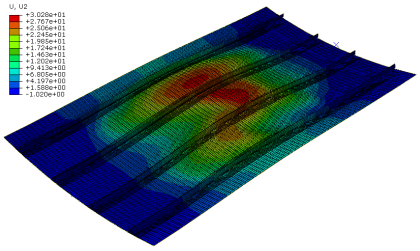

(b) Result of the model with an imperfection of 25%

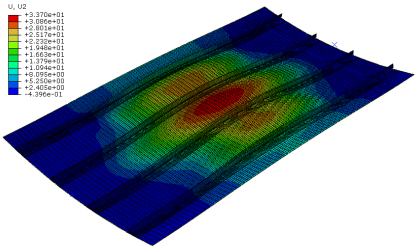

(c) Result of the model with an imperfection of 50%

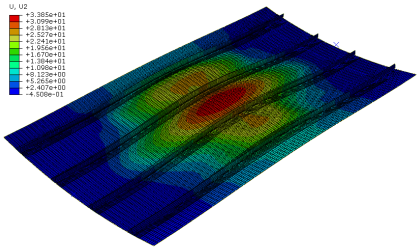

(d) Result of the model with an imperfection of 75%

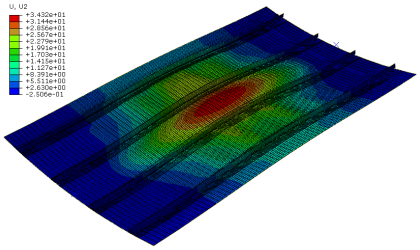

(e) Result of the model with an imperfection of 95%

Figure 5.43: Deformed shapes of the model with negative imperfection.

The load vs displacement curves of the model with positive imperfections are shown in Figure 5.44. It can be seen that the curves shifted to the right as it happened with panel P10 but in this case the curves deviate from the experimental curve. The prebuckling stiffness of both computational and experimental curves still match but the postbuckling stiffness tends to deviate with the increase of the magnitude of imperfections. Regarding the first global buckling load, it tends to decrease with the increase of the magnitude of imperfections. In Figure 5.45 it is shown the load vs displacement curves of the model with negative magnitude of imperfections. It can be seen that there are not big differences between the models with positive and negative imperfections. The curves of the models with negative magnitude of imperfections also shifted to the right side of the graph and the buckling load also decreases with the increase of the magnitude of imperfections.

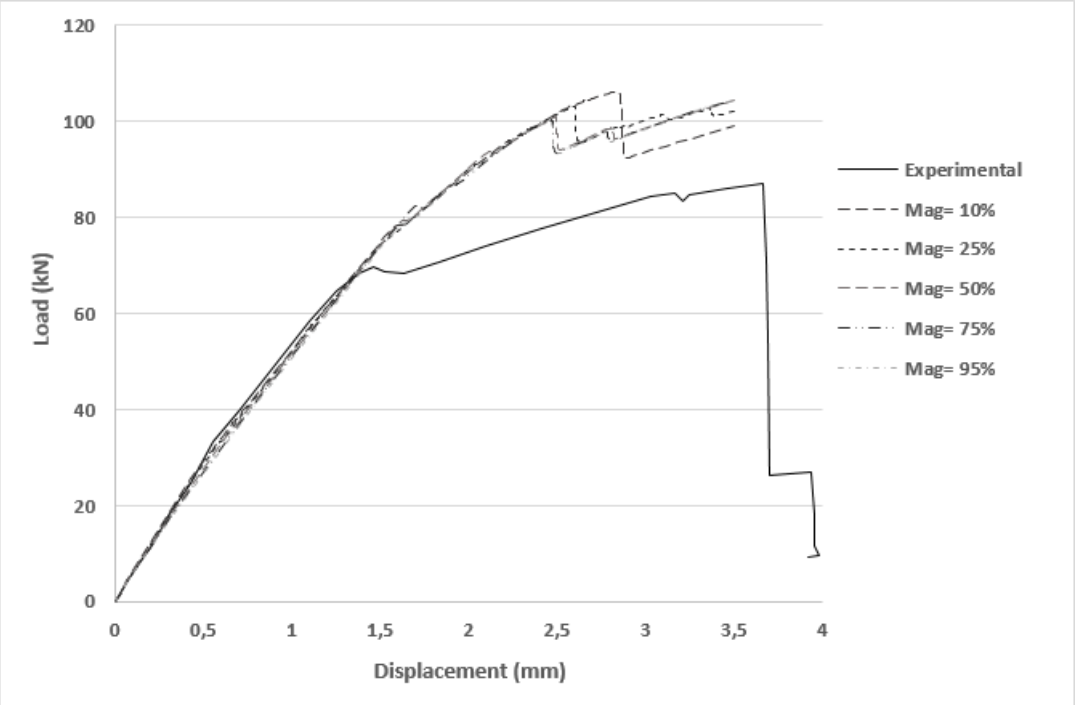

Figure 5.44: Load vs displacement curves of the model with positive imperfections.

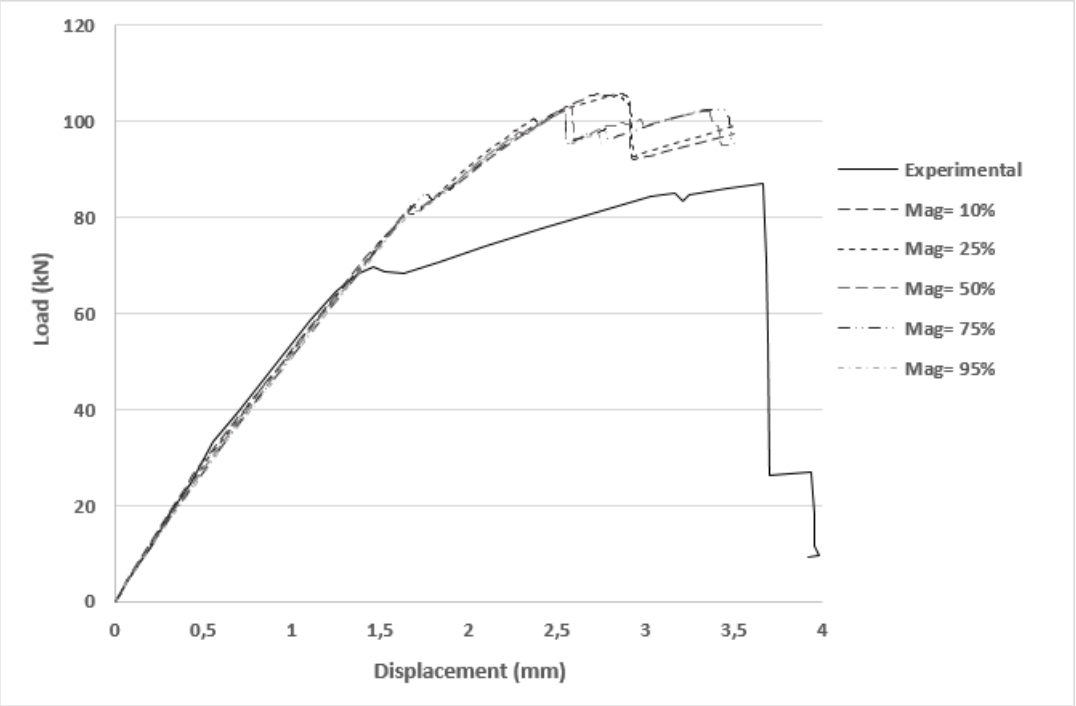

Figure 5.45: Load vs displacement curves of the model with negative imperfections.

It can be seen that the first global buckling load, of the load vs displacement curves obtained from the simulations, are too high when compared to the load vs displacement curve of the experimental result. In order to investigate the reasons, additional simulations were performed. Figure 5.2 d) shows how the longitudinal edges of the test specimens were embedded in supporting beams and, in order to enable free gliding of the panel in loading direction, the layers between the panel edge and the beam were made from a glass fiber/resin filling compound.

The effect of the supporting beams is modelled by springs acting subsequently on one, two, three and four node rows within the width of the embedding. Therefore, the boundary conditions applied in the longitudinal edges of the models were replaced by the springs. In Figure 5.46 it can be seen the model with two rows of springs. The springs were applied in the nodes within the width of the embedding.

The simulations of the model using springs, were made using the same model used to show the influence of the imperfections, however the results showed a first global buckling load too low. So the simulations were then made for the model with 40448 elements, S4R element formulation and a damping factor of 2e-7.

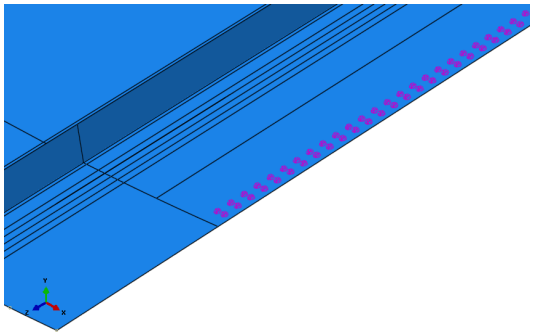

Figure 5.46: Model with two rows of springs.

In Figure 5.47 it is shown the deformed shapes obtained from this model and the respective load vs displacement curves are shown in Figure 5.48. All the models present a global buckling shape in the center of the panels. The load vs displacement curves shows that the axial stiffness of the four models using springs, in the prebuckling area, have a good agreement with the axial stiffness of the experimental curve. The increase of rows of springs influence the first global buckling load. Regarding the postbuckling area, it can be seen that the changing of the boundary conditions in the embedded region have a big influence in the axial stiffness of the panel. Therefore, it is difficult to simulate the load vs displacement curve in the deep postbuckling area, since there is no detailed knowledge of how the lateral edges influence the postbuckling behaviour of the panel, especially due to the effect of free gliding.

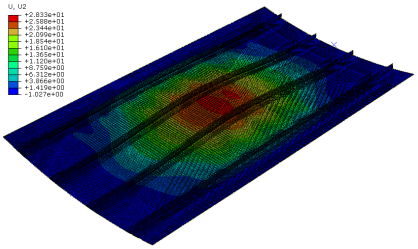

(a) Deformed shape of the model with one row of springs.

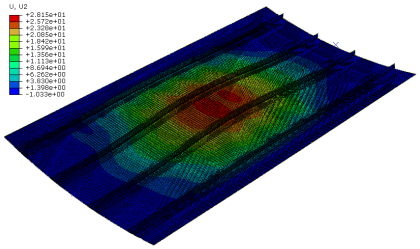

(b) Deformed shape of the model with two rows of springs.

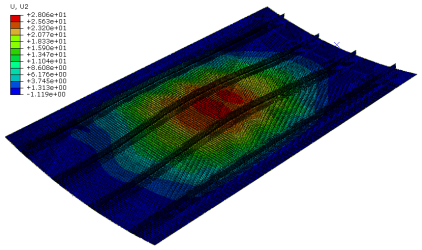

(c) Deformed shape of the model with three rows of springs.

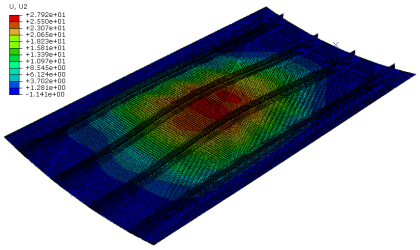

(d) Deformed shape of the model with four rows of springs.

Figure 5.47: Deformed shapes of the model with springs.

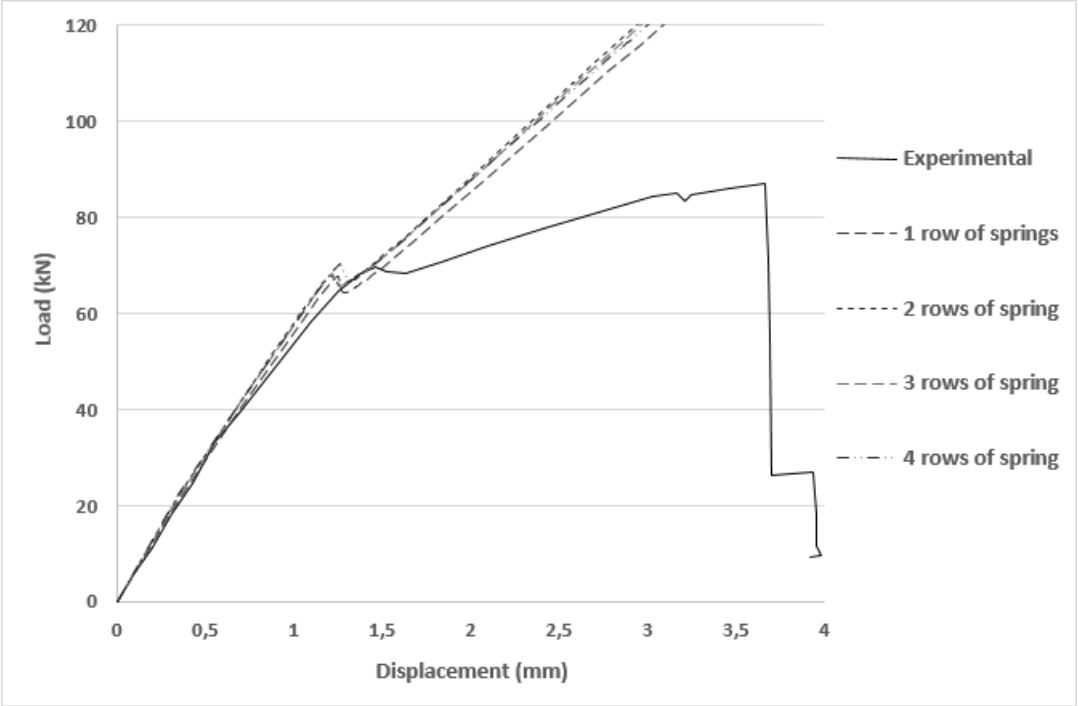

Figure 5.48: Influence of the boundary conditions of the longitudinal edge.

5.5 Summary of the results

Two different panels were tested in this chapter. The first one (panel P10) has three stringers while the second one (panel P12) has four stringers. Its distribution is also different, while panel P10 has a stringer in the center of the panel, the panel P12 has a skin field. Another difference between the two models is the radius of the skin, which is bigger for panel P10, and also the thickness of the skin which is bigger for panel P12.

As it was seen, the behaviour of the panels is influenced by several parameters. In general, for both models, a damping factor value equal to 2e-5 presents an horizontal area in the first global buckling area, while for higher damping factor values a peak starts to appear. Also the different values of damping factors influence the computational time, which increases with the decreased of the damping factor value. Panel P12 has shown a good agreement with the experimental results in the prebuckling area, however it was difficult to simulate the load vs displacement curve in the postbuckling area. The first global buckling load was too high comparatively with the reference value and it was seen how the boundary conditions of the lateral edges can influence this load. Regarding the panel P10 the prebuckling area of the models without imperfection did not match, however when the imperfections were introduced into the model, the curve shifted to the right, coinciding with the experimental curve.

It could be seen too how the number and type of elements influence the simulation of the load vs displacement curves. In general, the more refined is the mesh, higher is the first global buckling load. The same happened when the type of element was changed, for S4 element formulation, most of load vs displacement curves showed a first buckling load higher than the load vs displacement curves of the models with S4R element formulation. However for both number and type of elements, there are exceptions that were already mentioned. The computation time is also influenced by the number and type of elements used in the simulations. It increases with the increase of number of elements as also with the change of the S4R to the S4 element formulation.

Regarding the influence of the magnitude of imperfections it was seen that the load vs displacement curves of the panel P10 presented a different evolution when compared to the load vs displacement curves of the panel P12. While the load vs displacement curves of panel P12 showed a linear evolution, i.e., the first global buckling load decreased with the increase of the magnitude of imperfections (for both positive and negative magnitude of imperfections), the first global buckling load of panel P10 decreased and increased with the increase of the magnitude of imperfections, in the case of positive magnitude of imperfections. Regarding the negative magnitude of imperfections, the buckling load increased with the increase of the magnitude of imperfections. It was also seen for both panels that the load vs displacements curves tends to shift to the right side of the graph with the increase of the magnitude of imperfections.

Despite the material properties and boundary conditions being the same for both panels, they presented different behaviours, as it was expected, since their geometry was different. Both panels presented a global buckling shape, however in panel P10 it appeared in one side of the panel, while for panel P12 it appeared in the center of the panel. This can be explained by the position of the stringers as well as by the skin-stringer connection. It was easier to simulate the load vs displacement curves, in the postbuckling area, of panel P10, since it showed a better agreement with the experimental curve than panel P12. As it was mentioned, the numerical simulation of panel P12 were too stiff.

Chapter 6

Final considerations

6.1 Conclusion

The main goal of this thesis was the domain of computational tools based on the Finite Element Method (FEM) in order to analyse the behaviour of stiffened panels subjected to compressive loading conditions. The simulations carried out throughout the present work allow to take some conclusions on the methodologies and parameters that were intended to study.

Chapter 4 permitted to learn the methodologies involved in the analysis of the buckling behaviour. It was seen that the results obtained in this thesis for model TR almost matched the results obtained by Paulo in [1], and in the case of panel L, the load vs displacement curves showed the same behaviour but they were shifted a little bit to the right side of the graph. It was also seen how the magnitude of imperfections can influence the behaviour of the load vs displacement curves.

In Chapter 5 it was made the analysis of two different stiffened CFRP curved panels. The reason to study two different type of panels was to understand how the geometry can influence the postbuckling behaviour of the panels. It was seen that the existence or non existence of a stringer in the middle of the panel can influence the postbuckling behaviour. The use of the stabilize method involves the study of the damping factors and so four values were tested and its influence was shown. It was seen that the postbuckling area is influenced by the damping factor and when its value increases, the postbuckling area becomes horizontal (in the first buckling load area). Other parameters, such as the number and type of elements and magnitude of imperfections, were also tested. Regarding the magnitude of imperfections, it was seen that both panels showed a different evolution regarding the load vs displacement curves when the magnitude of imperfections is increased and it was also seen that positive and negative magnitude of imperfections affects differently the behaviour of the panels. In the case of panel P10 the first global buckling load decreased and increased with the increase of the magnitude of imperfections, for positive magnitude of imperfections, and it increased with the increase of the magnitude of imperfection for negative magnitude of imperfections. Regarding the panel P12 the first global buckling load decreased with the increase of the magnitude of imperfections, for both positive and negative magnitude of imperfections. It could also be seen that all load vs displacement curves tend to shift to the right side of the graphic with the increase of the magnitude of imperfections. Other parameter that was tested was the boundary condition applied to the lateral edges and it was shown how the

lack of knowledge on how the lateral edges are restrained can influence the postbuckling behaviour.

6.2 Future works

As it was mentioned before there are several parameters that can influence the behaviour of the panels and the skin-stringer connection is one of the those parameters. In this thesis the TIE constraint was the method chosen to connect the skin to the stringers but there are others that could be tested. One example is the multi-point constraint.

Models that take into account damage should be tested too. There are degradation models for ply failure of a laminate, for instance fiber fracture and matrix cracking and interlaminar damage, namely delamination. Some of the methods used to study the delaminations were already mentioned in the present work.

Bibliography

[1] Rui Paulo, Simulação numérica do comportamento mecânico de estruturas reforçadas, Tese de Mstrado, Universidade de Aveiro (2011).

[2] A. Rama Chandra Murthy, G. S. Palani, Nagesh R. Iyer ,Damage tolerant evaluation of cracked stiffened panels under fatigue loading, Indian Academy of Sciences (2012), 37: 171-186.

[3] E. A. Starke, Jr. and J. T. Staley, Application of modern aluminium alloys to aircraft, Prog. Aerospace Sci., 32: 131-172.

[4] P. Rigo, R. Sarghiuta, S. Estefen, E. Lehmann, S. C. Otelea, I. Pasqualino, B. C. Simonsen, Z. Wan, T. Yao, Sensitivity analysis on ultimate strength of aluminium stiffened panels, Marine Structures (2003), 16: 437-468.

[5] Jeom Kee Paik, Sjoerd van der Venn, Alexandre Duran, Matthew Collette, Ultimate compressive strength design methods of aluminum welded stiffened panel structures for aerospace, marine and land-based applications: A benchmark study, Thin-Walled Structures (2005), 43: 1550-1566.

[6] Mohammad Reza Khedmati, Pedram Edalat, A numerical investigation into the effects of parabolic curvature on the buckling strength and behaviour of stiffened plates under in-plane compression, Latin American Journal of Solids and Structures (2010), 7: 249-264.

[7] J. Campbell, L. Hetey and R. Vignjevic, Non-Linear Idealisation Error Analysis of a Metallic Stiffened Panel Loaded in Compression, Thin-Walled Structures (2012), 54: 44-53.

[8] Eirik Byklum, Eivind Steen, Jorgen Amdahl, A semi-analytical model for global buckling and post-buckling analysis of stiffened panels, Thin-Walled Structures (2004), 42: 701-717.

[9] A. Aalberg , M. Langseth , P. K. Larsen, Stiffened aluminium panels subjected to axial compression, Thin-Walled Structures (2001), 39: 861-885.

[10] Mohammad Reza Khedmati, Abbas Bayatfar, Philippe Rigo. Post-buckling behaviour and strength of multi-stiffened aluminium panels under combined axial compression and lateral pressure, Thin-Walled Structures (2010), 23: 39-66.

[11] Torsten Mocker, Hans-Gunther Reimerdes, Postbuckling simulation of curved stiffened composite panels by the use of strip elements, Composite Structures (2006), 73: 237-243.

[12] S. Adali, Izzet U. Cagdas, Failure analysis of curved composite panels based on first-ply and buckling failures, Procedia Engineering (2011), 10: 1591-1596.

[13] J. F. Caseiro, R. A. F. Valente, A. Andrade Campos, J. W. Yoon, Elasto-plastic buckling of integrally stiffened panels (ISP): An optimization approach for the design of cross section profiles, Thin-Walled Structures (2011), 49: 864-873.

[14] Xiang Zhang, Yazhi Li, Damage tolerance and fail safety of welded aircraft wing panels, AIAA Journal (2005), 43: 1613-1623.

[15] Collette M., Incecik A., Ultimate strength design and reliability of aluminium structures for high speed craft, Chesapeake Section SNAME Presentation (2005).

[16] Fred Delany, Stephan W. Kallee, Mike J. Russel, Friction stir welding of aluminium ships, (2007). Consulted on 2014 in: http://www.twi-global.com/technical-knowledge/published-papers/friction-stir-welding-of-aluminium-ships-june-2007/.

[17] Marcelo F. S. F. de Moura, Alfredo B. de Morais, Antnio G. de Magalhes, Materiais Compsitos - Materiais, Fabrico e Comportamento Mecnico, 2ł Edio, Publindstria (2011).

[18] Se-Hee Oh, Kwang-Soo Kim, Chun-Gon Kim, An efficient postbuckling analysis technique for composite stiffened curved panels, Composite Structures (2006), 74: 361-369.

[19] A. Blzquez, J. Reinoso, F. Pars, J. Caas, Postbuckling behavior of a pressurized stiffened composite panel - Part II: Numerical analysis. Effect of the geometrical imperfections, Composite Structures (2011), 94: 1544-1554.

[20] Broderick H. Coburn, Zhangming Wu, Paul M. Weaver, Buckling analysis of stiffened variable angle tow panels, Composite Structures (2014), 111: 259-270.

[21] Composite Structures. Consulted on 2015 in: http://www.aerooptimal.com/industries/composite-structures.

[22] L. Huang, A. H. Sheikh, C-T Ng, M. C. Griffith, An efficient finite element model for buckling analysis of grid stiffened laminated composite plates, Composite Structures (2014).

[23] Norman F. Knight Jr., James H. Starnes Jr., Postbuckling Behavior of Selected Curved Stiffened Graphite-Epoxy Panels Loaded in Axial Compression, AIAA Journal (2013), 26: 344-352.

[24] Riccardo Vescovini, Chiara Bisagni, Buckling Optimization of Stiffened Composite Flat and Curved Panels, AIAA (2011).

[25] Luca Lanzi, Vittorio Giavotto, Post-buckling optimization of composite stiffened panels: Computations and experiments, Composite Structures (2006), 73: 208-220.

[26] A. Riccio, A. Raimondo, F. Scaramuzzino, A robust numerical approach for the simulation of skin-stringer debonding growth in stiffened composite panels under compression, Composites: Part B (2015), 71: 131-142.

[27] Alessandro T. Neto, Flvio L. S. Bussamra, Henrique A. C. Silva, A new metamodel for reinforced panels under compressive loads and its application to the fuselage conception, Latin American Journal of Solids and Structures (2014), 11: 223-244.

[28] B. H. Sun, K. Y. Yeh, F. P. J. Rimrott, On the Buckling of Structures, Technische Mechanik (1995), 15: 129-140.

[29] J. W. Yoon, G. H. Bray, R. A. F. Valente, T. E. R. Childs, Buckling analysis for an integrally stiffened panel structure with a friction stir weld, Thin-Walled Structures (2009).

[30] R. M. F. Paulo, F. Teixeira Dias, R. A. F. Valente, Numerical simulation of aluminium stiffened panels subjected to axial compression: Sensitivity analysis to initial geometrical imperfections and material properties, Thin-Walled Structures (2013), 62: 65-74.

[31] D. G. Stamatelos, G. N. Labeas, K. I. Tserpes, Analytical calculation of local buckling and post-buckling behaviour of isotropic and orthotropic stiffened panels, Thin-Walled Structures (2010), 49: 422-430.

[32] A. Murphy, M. Price, A.Gibson, C. G. Armstrong, Efficient non-linear modelling of fuselage panels, ICAS2002 Congress (2002).

[33] C. Lynch, A. Murphy, M. Price, A. Gibson, The computational post buckling analysis of fuselage stiffened panels loaded in compression, Thin-Walled Structures (2004), 42: 1445-1464.

[34] Richard Degenhardt, Jean-Pierre Delsemme, Buckling and postbuckling analysis of a CFRP stiffened panel for a better material exploitation, DLR, Institute of Structural Mechanics, SAMTECH.

[35] D. S. Zarouchas, R.C. Alderliensten, The effect of disbonds on stability aspects of adhesively bonded aluminium panels during compression loading, Thin-Walled Structures (2015), 96: 372-382.

[36] Ning Hu, Hisao Fukunaga, Hideki Sekine, Kouchakzadeh Mohammad Ali, Compressive buckling of laminates with an embedded delamination, Composite Science and Technology (1999), 59: 1247-1260.

[37] Yusuf Arman, Mehmet Zor, Sami Aksoy, Determination of critical delamination diameter of laminated composite plates under buckling loads, Composite Science and Technology (2006), 66: 2945-2953.

[38] S. Psarras, S.T. Pinho, B.G. Falzon, Damage-Tolerant Design of Stiffener Run-Outs: A Finite Element Approach (2012).

[39] Lucas F.M. da Silva, Paulo J.C. das Neves, R.D. Adams, J.K. Spelt, Analytical models of adhesively bonded joints- Part I: Literature survey, International Journal of Adhesion and Adhesives (2009), 29: 319-330.

[40] Adrian C. Orifici, Rodney S. Thomson, Richard Degenhardt, Chiara Bisagni, Javid Bayandor, A finite element methodology for analysing degradation and collapse in postbuckling composite aerospace structures, Journal of Composite Materials (2009), 43: 1-26

[41] P. P. Camanho, C. G. Dvila, Mixed-Mode Decohesion Finite Elements for the Simulation of Delamination in Composite Materials, NASA CASI (2002).

[42] A. Murphy, M. Price, R. Curran, P. Wang, Integration of strength and process modelling of friction stir welded fuselage panels, Journal of aerospace computing, information and communication (2006), 3: 159-176.

[43] Friction Stir Welding, Technical Handbook, ESAB.

[44] A. Murphy, F. Lynch, M. Price, A. Gibson, Modified stiffened panel analysis methods for laser beam and friction stir welded aircraft panels, Journal of Aerospace Engineering (2006), 220: 267-278 .

[45] A. Murphy, T. Ekmekyapar, D. Quinn, M. Ozaka, K. Poston, G. Moore, J.Niblock, The influence of assembly friction stir weld location on wing panel static strength, Thin-Walled Structures (2013), 76: 56-64.

[46] F. Teixeira Dias, J. Pinho da Cruz, R. A. Fontes Valente, R. J. Alves de Sousa, Método dos Elementos Finitos - Técnicas de Simulação Numérica em Engenharia, LIDEL (2009).

[47] Abaqus 6.13 Analysis User's guide.

[48] R. Degenhardt, H. Klein, H. Temmen, R. Zimmermann, Buckling and postbuckling analysis of shells under quasi-static and dynamic load, DLR Institute of Structural Mechanics.

[49] A.C. Orifici, R. S. Thomson, R. Degenhardt, A. Kling, K. Rohwer, J. Bayandor, Degradation investigation in a postbuckling composite stiffened fuselage panel, Composite Structures (2007).

[50] S. Lauterbach, A. C. Orifici, W. Wagner, C. Balzani, H. Abramovich, R. Thomson, Damage sensitivity of axially loaded stringer-stiffened curved CFRP panels, Composite Science and Technology (2009), 70: 240-248.

[51] Ever J. Barbero, Finite Element Analysis of Composite Materials using Abaqus, CRC Press, Taylor & Francis Group (2013).

[52] The path to saving fuel by reducing wight (2008). Consulted on 2014 in: http:/newenergyandfuel/com/2008/08/15/the-path-to-saving-fuel-by-reducing-weight/

[53] Matthew J. Tauris, Stress analysis of a fiber reinforced-polymer matrix orthotropic plate with an elliptical hole (2009).

[54] Hagbart S. Alsos, Jorgen Amdahl, Odd S. Hopperstad, On the resistance to penetration of stiffened plates, Part II: Numerical analysis, International Journal of Impact Engineering (2008), 36: 875-887.

[55] R. Zimmermann, H. Klein, A. Kling, Buckling and postbuckling of stringer stiffened fibre composite curved panels - Tests and computations, Composite Structures (2006), 73: 150-161.

[56] R. Degenhardt, A. Kling, K. Rohwer, A.C. Orifici, R.S. Thomson, Design and analysis of stiffened composite panels including post-buckling and collapse, Computers and Structures (2008), 86: 919-929.

[57] P. K. Mallick, Fiber-Reinforced composites, Materials, Manufacturing and Design, Third Edition, Taylor & Francis Group, (2007).